



**Università degli Studi di Milano**  
**Scuola di Dottorato in Medicina Molecolare**  
**Dipartimento di Scienze e Tecnologie Biomediche**

Curriculum di *Genomica, Proteomica e Tecnologie Correlate*

Ciclo XXIV

Settore Disciplinare: BIO - 10

Anno Accademico 2011/2012

**Dottorando:** Dr.ssa Moira MARIZZONI  
Matricola: R08227

**DEVELOPMENT OF IMAGING MARKERS  
TO TRACK ALZHEIMER'S DISEASE PROGRESSION  
IN HUMANS AND MOUSE MODELS**

**Direttore della Scuola:** Ch.mo Prof. Mario Clerici

**Tutore:** Ch.mo Prof. Mario Clerici

**Co-Tutore:** Dr. Giovanni Frisoni

## CONTENTS

ABSTRACT .....	IV
SOMMARIO .....	V
1 ALZHEMER DISEASE .....	1
1.1 <i>Introducion</i> .....	1
1.2 <i>Clinical utility of biomarkers in AD</i> .....	1
2 AIM OF THE STUDY .....	5
3 PART I: ANIMAL IMAGING.....	6
3.1 <i>AD transgenic mice</i> .....	6
3.1.1 Models of amyloidosis .....	6
3.1.2 Models of tauopathy.....	7
3.1.3 Models of amyloidosis and tauophaty .....	8
3.2 <i>Tg as model of preclinical AD</i> .....	8
3.2.1 Neuritic alterations .....	8
3.2.2 Synaptic dysfunction .....	9
3.3 <i>Imaging markers</i> .....	11
3.3.1 Structural outcomes.....	11
3.3.1.1 <i>Structural MRI</i> .....	11
3.3.1.2 <i>Diffusion Tensor Imaging (DTI)</i> .....	14
3.3.2 Functional or metabolic outcomes.....	14
3.3.2.1 <i>Glucose uptake</i> .....	14
3.3.2.2 <i>Brain perfusion</i> .....	15
3.3.2.3 <i>Spectroscopy (MRS)</i> .....	17
3.4 <i>Part I: animal imaging study goals</i> .....	18
3.5 <i>Materials and Methods</i> .....	19
3.5.1 Animals .....	19
3.5.2 MRI animal preparation .....	19
3.5.3 MRI acquisitions .....	19
3.5.4 Data post-processing .....	20
3.5.4.1 <i>Volumetric data analysis</i> .....	20
3.5.4.2 <i>Diffusion data analysis: estimation of structural connectivity</i> <i>measures</i> .....	21
3.5.4.2.1 <i>Tract-Based Spatial Statistics (TBSS)</i> .....	21
3.5.4.2.2 <i>ROI-based analysis</i> .....	21
3.5.4.3 <i>Entorhinal cortex thickness measurement</i> .....	22
3.5.5 Histology and immunohistochemistry .....	23
3.5.5.1 <i>6E10, GFAP and Cd11b antibodies</i> .....	23
3.5.5.2 <i>Gold-chloride</i> .....	24
3.5.6 Statistical analysis.....	24
3.6 <i>Results</i> .....	25
3.6.1 TASTPM.....	25
3.6.1.1 <i>Morphometry results</i> .....	25



3.6.1.2 Diffusion results .....	27
3.6.1.3 Histology.....	32
3.6.2 TAUPS2APP .....	37
3.6.2.1 Morphometry results .....	37
3.6.2.2 Diffusion results .....	38
3.6.2.3 Histology.....	39
3.6.3 PDAPP .....	42
3.6.3.1 Morphometry results .....	42
3.6.3.2 Diffusion results .....	43
3.6.3.3 Histology.....	44
3.7 Discussion.....	49
3.7.1 Brain structural outcome .....	49
3.7.1.1 Genotype effect.....	49
3.7.1.2 Genotype x age effect .....	49
3.7.2 Brain Diffusion outcome .....	50
3.7.2.1 White matter .....	50
3.7.2.2 Grey matter.....	50
3.8 Conclusions and future prospects .....	51
3.8.1 Markers selection .....	51
4 PART II: HUMAN IMAGING .....	53
4.1 Introduction.....	53
4.2 Part II: Human imaging study goals .....	55
4.3 Materials and methods .....	56
4.3.1 Subjects .....	56
4.3.2 MRI acquisitions .....	57
4.3.3 Data preparation .....	58
4.3.4 Data post-processing .....	58
4.3.4.1 Volumetric Measurement.....	58
4.3.4.2 Diffusion data analysis: estimation of structural connectivity measures .....	59
4.3.5 Evaluation of reliability .....	60
4.3.6 Statistical analysis.....	61
4.4 Results.....	62
4.4.1 Morphometry Results.....	62
4.4.1.1 Estimation of brain morphometric volumes across MRI sites..	63
4.4.1.2 Estimation of volume reproducibility: effects of MRI sites and segmentation analyses .....	63
4.4.1.3 Estimation of spatial reproducibility of volumetric segmentations: effects of MRI sites and segmentation analyses .....	66
4.4.1.4 Estimation of cortical thicknesses across MRI sites.....	67
4.4.1.5 Estimation of thickness reproducibility: effects of MRI sites and segmentation analysis .....	68
4.4.2 Diffusion results .....	71
4.4.2.1 Estimation of brain diffusion parameters across MRI sites.....	72

4.4.2.1 Estimation of brain diffusion parameters reproducibility across MRI sites .....	74
4.4.2.2 Estimation of CV and ICC: effects of MRI sites .....	77
4.4.2.3 Estimation of spatial reproducibility of atlas-based ROIs: effects of MRI sites.....	78
4.5 Discussion.....	79
4.5.1 Brain morphometry .....	79
4.5.2 Brain diffusion .....	80
4.5.3 Limits of the study.....	81
4.6 Conclusions and future prospects .....	82
5 ACKNOWLEDGEMENTS.....	83
6 LIST OF TABLES AND FIGURES.....	84
7 BIBLIOGRAPHY .....	90
8 SCIENTIFIC PRODUCTS .....	105

## ABSTRACT

Alzheimer's disease (AD) is the most common form of dementia in elderly population, affecting more than 35 million people worldwide. To date, the only approved therapies for AD focus on symptomatic relief. The development of new therapeutic agents is time consuming and costly. Drug discovery process is arduous because clinical trials are currently involving too wide sample of patients and long follow-up. Moreover, the predicting value of experimental models used nowadays is limited due to the lack of homologous markers in humans and animals.

This work is a branch of Pharmacog, an industry-academic European project aimed at identifying reliable biomarkers that are sensitive to disease progression in patients with Mild Cognitive Impairment (MCI) and in AD animal models in order to bridge the gap between preclinical and clinical outcomes. Human neuroimaging markers are among the most promising candidates to track disease progression. In addition, advanced magnetic resonance imaging (MRI) allow the identification of homologous biomarkers in humans and mice. Prior to investigate neuroimaging biomarkers on MCI patients, we have to test that there is no significant effect of within and across MRI sites variability on brain AD-related longitudinal changes.

The first aim of this work is the study of the morphometric and diffusion changes in three different AD mouse model (TASTPM, TauPS2APP and PDAPP from 3 to 22 months of age) through MRI. We found significant volume reduction starting at 9 months in the caudate-putamen and frontal cortex of TASTPM and TauPS2APP ( $p < 0.001$ ) compared to non transgenic mice. The decrease in the enthorinal cortex thickness was significantly lower in all the strains ( $p < 0.001$ ). We also found age-related diffusion abnormalities in different white matter regions of TASTPM. The earlier changes were found in the corpus callosum and anterior commissure of 13 months old mice ( $p < 0.001$ ). In TASTPM, deficits detected with MRI are related to heavy amyloid pathology, marked gliosis and astrocitosis.

The second aim of this study is the evaluation and comparison of test-retest reproducibility of brain volumes and thicknesses by two existing Freesurfer pipelines (longitudinal and cross-sectional). Moreover, we assessed the reliability of a diffusion pipeline developed in our lab. Eight different 3T MRI sites in Europe enrolled a group of 5 healthy elderly subjects scanned twice at least a week apart. We found that the within and across sites variability of volumes was less than 3% for larger brain structures (such as thalamus) and less than 6% for smaller regions (i.e., hippocampus). The thickness variability was less than 6% and diffusion indices variations were mostly within the range 2-3%.

In conclusion, the present data identify imaging biomarkers of disease progression in mice similar to that seen in humans and pave the way of a murine "imaging signature" usefulness in clinical trials. Human data show significantly higher reproducibility of brain morphometry using the longitudinal pipeline than using the cross-sectional one ( $p < 0.01$ ). Finally, we demonstrated that the reliability of the analysis of brain diffusion we implemented in our lab is comparable to data reported in the literature.

## SOMMARIO

La Malattia di Alzheimer (AD) è la forma più comune di demenza nella popolazione anziana e affligge più 35 milioni di persone nel mondo. Ad oggi, le uniche terapie approvate per la sua cura sono dirette a ridurre i sintomi. Lo sviluppo di nuovi farmaci è lungo e costoso. Il processo di scoperta è arduo in quanto i trial clinici coinvolgono un ampio campione di pazienti e implicano dei follow-up troppo lunghi. Inoltre il valore predittivo dei modelli sperimentali è limitato a causa della mancanza di marcatori omologhi nell'uomo e nei modelli animali.

Questo lavoro si inserisce in Pharmacog, un progetto europeo che vede la collaborazione di università ed industrie allo scopo di identificare biomarcatori affidabili e sensibili alla progressione di malattia in pazienti affetti da decadimento cognitivo lieve (MCI) e modelli animali di AD allo scopo di colmare il vuoto tra risultati clinici e preclinici. Nell'uomo, i marcatori di neuroimmagine sono tra i più promettenti candidati nel tracciare la progressione di malattia. Innovazioni nelle tecniche di risonanza magnetica (MRI) rendono possibile l'identificazione di marcatori omologhi nell'uomo e nel topo. Prima dello studio di neuroimmagine nei pazienti MCI, è necessario verificare che eventuali cambiamenti individuati siano dovuti all'effettiva progressione di malattia e non causati dalla variabilità intra e tra i diversi scanner utilizzati nel progetto.

Il primo scopo di questo lavoro è lo studio dei cambiamenti morfometrici e di diffusione in tre diversi modelli murini di Malattia Alzheimer (TASTPM, TauPS2APP e PDAPP da 3 a 22 mesi) tramite l'utilizzo di tecniche MRI. A nove mesi abbiamo trovato una significativa riduzione rispetto ai controlli del volume del caudato-putamen e della corteccia frontale nei TASTPM e nei TauPS2APP ( $p < 0.001$ ). L'assottigliamento della corteccia entorinale era significativo alla stessa età in tutte e tre i modelli ( $p < 0.001$ ). Abbiamo inoltre individuato delle anomalie dipendenti dall'età anche in diverse regioni di sostanza bianca. Quelle più precoci erano nella commissura anteriore e nel corpo calloso dei TASTPM di 13 mesi ( $p < 0.001$ ). I danni dei TASTPM sono associabili al pesante carico di amiloide ed alla marcata attivazione della glia e degli astrociti.

Il secondo scopo dello studio è la valutazione e la comparazione della riproducibilità di misure volumetriche e di spessore tra test e retest ottenute utilizzando due diversi metodi di processazione esistenti (Freesurfer sulla singola acquisizione o Freesurfer longitudinale). Inoltre abbiamo saggiato la riproducibilità di un'analisi per le immagini di diffusione messa a punto nel nostro laboratorio. A questo scopo ognuno degli otto centri europei coinvolti nel progetto e con diversi scanner a 3T ha arruolato un gruppo di 5 volontari sani e anziani sottoponendoli a 2 acquisizioni di risonanza ad almeno una settimana di distanza l'una dall'altra. Abbiamo trovato che la variabilità intra e tra i diversi centri nei volumi estratti da queste acquisizioni era inferiore al 3% per le strutture più grandi (come il talamo) e minore del 6% per quelle più piccole (es. amigdala). La variabilità degli spessori era meno del 6% e le variazioni dei parametri di diffusione erano prevalentemente nell'intervallo del 2-3%.

In conclusione, abbiamo identificato nei modelli analizzati dei marcatori di immagine sensibili alla progressione dell'AD simili a quelli visti nell'uomo e questo apre la strada al possibile utilizzo di una "distintiva collezione" di marcatori murini di

immagine nei trial clinici. I dati collezionati nella parte umana mostrano un più alta riproducibilità dei risultati morfometrici ottenuti con l'analisi longitudinale rispetto a quella sulla singola acquisizione ( $p < 0.01$ ). Infine, abbiamo dimostrato che l'analisi delle immagini di diffusione messa a punto nel nostro laboratorio dà risultati ugualmente riproducibili a quelli riportati in letteratura.

## LIST OF SYMBOLS

ac	anterior commissure
AD	Alzheimer Disease
AICD	amyloid intracellular domain
Amy	Amygdale
APH1	anterior pharynx defective 1
APP	Apolipoprotein
A $\beta$	$\beta$ amyloid
BACE1	$\beta$ -site APP-cleaving enzyme 1
Cau	Caudate
Cau-Put	caudate-putamen
CBF	Cerebral blood flow
CBV	Cerebral blood volume
cc	corpus callosum,
cc_body	body of the corpus callosum
cc_genu	genu of the corpus callosum
cc_spl	splenium of the corpus callosum
Cdk5	Cyclin-dependent kinase 5
Cho	Choline
cing	cingulum
cp	cerebral peduncle
crtsp	corticospinal tract
CS	Cross sectional stream
CSF	Cerebrospinal fluid
CTF- $\alpha$	carboxy-terminal fragment
Ctx	Cortex
Ctx	Cortex (except the frontal)
CV	Coefficient of variation
DTI	Diffusion Tensor Imaging
DWI	Diffusion Weighted Imaging
ec	external capsule
EMA	European Medicines Agency
ent/ERC	entorhinal cortex
FA	Fractional anisotropy
FAD	Familial AD
FAT	fast axonal transport
fi	fimbria
FLIRT	FMRIB 's Linear Image Registration Tool
FOV	Field of view
FSL	FMRIB Software Library
FTDP	Frontotemporal Dementia with parkinsonism linked to chromosome 17
Fus	Fusiform gyrus
GFAP	Anti-glial Fibrillary Acid Protein
Glu	Glutamate
GSK-3 $\beta$	glycogen synthase kinase 3 $\beta$
HMG-CoA reductase	3 hydroxy-3-methylglutaryl-coenzyme A reductase

Hp	Hippocampus
ICC	Intraclass correlation coefficient
ICV	Intracranial volume
ILF	inferior lateral fasciculus
int	internal capsule
Lat	Lateral ventricle
LatOc	Lateraloccipital gyrus
LG	Longitudinal stream
Ling	Lingual gyrus
LTD	Long term depression
LTP	Long term potentiation
MAPT	microtubul-associated protein tau
MCI	Mild Cognitive Impairment
MD	Mean diffusivity
MEMRI	Manganese-Enhanced MRI
mIns	myo-inositol
MRI	Magnetic Risonance Imaging
NAA	N-acetylaspertate
NFT	Neurofibrillay tangles
NGS	Normal goat serum
ns	non significant
NSE	neuron-specific enolase
OB	Olfactory bulb
Pal	Pallidum
Parahp	Parahippocampal gyrus
PBS	Phosphate buffered saline
PCC	Posterior cingulated cortices
PDGF $\beta$	platelet-derived growth factor $\beta$ -chain) and
PET	Positron emission tomography
PPD	Paired-pulse depression
PPF	Paired-pulse facilitation
Prec	Precuneus
PrP	prion protein
PS1	Presenilin 1
PS2	Presenilin 2
PSs	Presenilins
Put	Putamen
RA	Relative anisotropy
RF	Radio frequency
ROI	Region of interest
RT	Room temperature
SLF	superior lateral fasciculus
SOD-2	Superoxide dismutase 2
SupFr	Superiorfrontal gyrus
SupPar	Superiorparietal gyrus
Supra	Supramarginal gyrus
SupTem	Superiortemporal gyrus

TBS	Tris buffered saline
TBSS	Tract Based Spatial Statistics
TE	Echo time
Tg	Transgenic mice
Thal	Thalamus
Thy-1	thymocyte differentiation antigen 1
TP	temporo-parietal cortex
TR	Repetition time
Vent	Lateral, third and fourth ventricles
WB	Whole brain
WT	wild-type
$\lambda_{\perp}$	Radial diffusivity
$\lambda_{  }$	Axial diffusivity



# 1 ALZHEMER DISEASE

## 1.1 Introduction

Alzheimer's disease (AD) is the most common form of dementia in elderly people affecting more than 35 million people worldwide [1]. Its incidence increases exponentially with age [2] and the median survival time from diagnosis is around three-ten years [3]. AD is characterized by the deterioration of memory, behaviour, emotion and cognition. Most AD cases are sporadic with unknown causes, whereas the familial or inherited form of AD (FAD), accounting for only 1-10% of cases, presents several autosomal dominant mutations. AD brains are characterized by the accumulation of two major proteins:  $\beta$ -amyloid ( $A\beta$ ) and hyperphosphorylated tau. The former constitutes extracellular deposits [4] in the parenchyma and in brain vessels, the latter forms intracellular neurofibrillary tangles (NFT) [5, 6]. Synaptic impairment, metabolic deficits, neuronal loss and inflammation are also present. The pathological process starts years before the appearance of clinical symptoms and progressively gets worst with time [7].

AD was discovered in 1906 by Alois Alzheimer from whom the pathology takes its name; he reported the case of Auguste D., a 51-year-old woman presenting several of the cardinal features observed in most patients nowadays. In the middle 1980s the  $A\beta$  peptide, the main component of amyloid plaques, was purified and sequenced [8, 9], giving rise to the "amyloid hypothesis" of AD, which suggests an initiating role of  $A\beta$  in the kickoff of the degenerative process where loss of tau physiological functions is required to elicit symptoms.

## 1.2 Clinical utility of biomarkers in AD

There are two distinct approaches for the treatment of AD: symptomatic relief (i.e., improvement of cognitive performance) and disease modification (i.e., prevention, slowing or reversal of the underlying pathological processes). To date, the only approved therapies for AD focus on symptomatic relief because any drug has convincingly shown disease modifying effects. The development of therapeutic agents in this field is time consuming, costly and continuous to delay the effective treatments of patients [10]. Drug discovery process is challenging because clinical trials are currently implicating wide sample size and follow-up for as far as 18 months [11]. Moreover, experimental models recapitulating the main pathological characteristics of AD have not yet been engineered and this might explain the unexpected results and failure of the numerous clinical trials carried out so far. Identifying biomarkers sensitive to disease progression is fundamental for diagnostic purpose and to accelerate the clinical application of novel therapeutic agents [12]. Pharmacog is an industry-academic European project aimed at identifying reliable biomarkers that are sensitive to disease progression in patients with Mild Cognitive Impairment (MCI) and animal models to bridge the gap between preclinical and clinical outcomes. Longitudinal studies in patients with MCI, who have a high risk of developing AD, and animals will improve our capability to selectively quantify the pathological progressive changes and thus discover and define novel indices of disease progression in both. An ideal translatable biomarker of disease progression should be identified in humans and

have a similar history in animals. Moreover, it should give reliable results in drug testing allowing translatable therapeutic considerations for human patients. Recently a biomarker model of the preclinical AD has been proposed [13] (Fig 1a). The pathologic markers variations can be temporally divided in i) amyloid  $\beta$  ( $A\beta$ ) deposition, evaluated through reduction in CSF  $A\beta_{42}$  and increased in amyloid tracer retention on positron emission tomography (PET); ii) synaptic markers alterations detected using fluorodeoxyglucose (FDG) uptake on PET and iii) AD-related neuronal loss on magnetic resonance imaging (MRI) [13]. Transgenic mice (Tg) carrying human mutated genes associated to AD, such as amyloid precursor protein (APP) or presenilins (PSs), are considered models of preclinical AD because they reproduce different pathological features, such as  $A\beta$  accumulation into amyloid plaques or neurofibrillary tangles or synaptic dysfunction and, as for humans, mouse deficits increase with age (Fig 1b). In mice, the protein expression pattern depends on the transgene promoter, the amount of amyloid deposition seems to be influenced by gene mutation type and genetic background could also account for strain differences. Although different complex animal models exist, none of them replicates the AD pathology as a whole but animal models are available for a number of pathological AD features allowing to translate human markers to or develop new ones from mice.

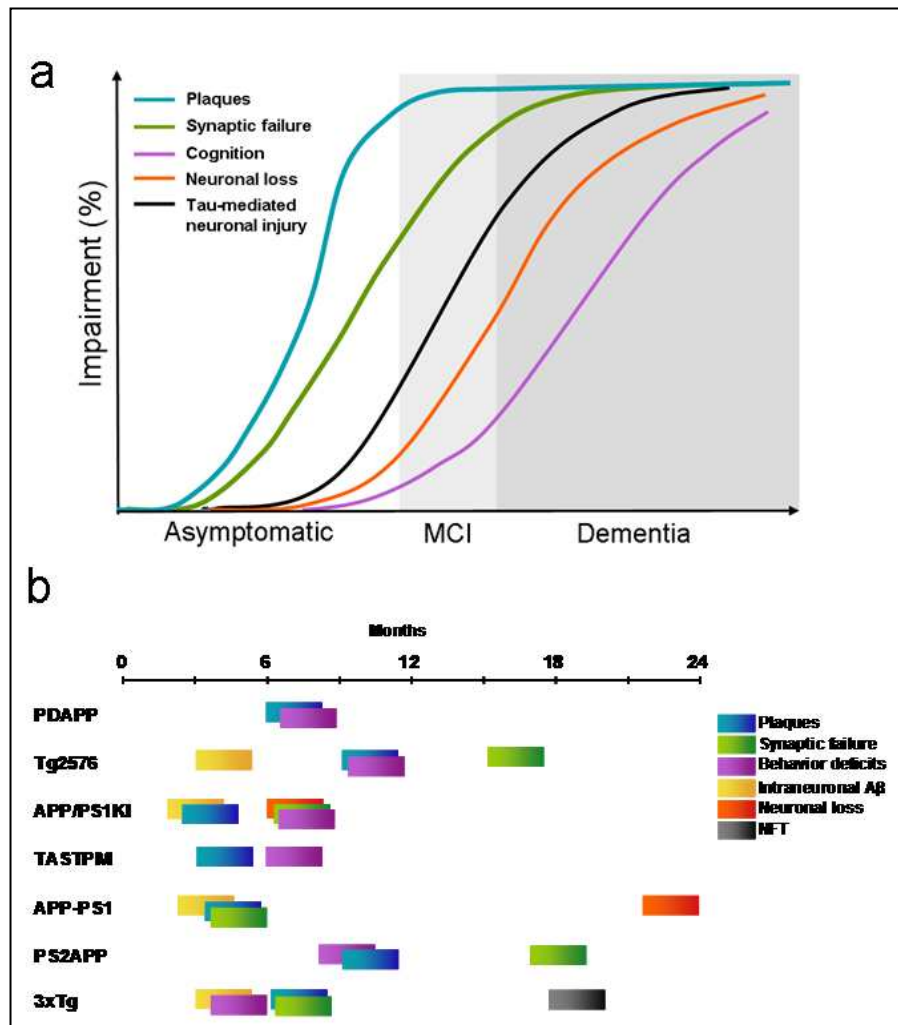


**Figure 1. Hypothetical model of dynamic biomarkers in human AD (a) [13] and pathological AD progression in the most frequently used mice (b).** Models of amyloidosis are created by deploying one, or a combination of, genes that have been found mutated in Familiar AD subjects (such as APP and PS1). These mice show structural, functional and biochemical alterations similarly to the human pre-clinical stage of AD pathology. Moreover, as for human, mouse deficits increase with age. All APP and/or PS1 Tg mouse models do not reproduce tangles. Tau pathology can be replicated in mice using modifications in the sequence of tau protein discovered in the familiar form of Frontotemporal Dementia with parkinsonism linked to chromosome 17 and Tau Tg mice are characterized by tangles in absence of A $\beta$ . The triple transgenic mouse model, carrying mutation in

*APP, PS1 and Tau (3xTg) better reproduces the signature lesions of AD as it develops both A $\beta$  and tangles.*

## 2 AIM OF THE STUDY

My work is inside IMI-Pharmacog, an industry-academic European project investigating the translational information derived from neuroimaging, biochemical, neurophysiological and neuropsychological outcomes in animal models and patients with MCI to discover and define novel indices of disease progression in both.

The two main goals of my project were focused on preclinical and clinical neuroimaging analysis. The **preclinical** side was dedicated to study biomarkers which are shown to be altered in the human disease [14, 15] and find new ones, in three transgenic animal models. Identifying an imaging biomarker signatures in mice similar to that seen in MCI patients would improve predictive capacity for the clinic. We analyzed in details morphometric and diffusion changes in three different AD mouse model, such as TASTPM, TauPS2APP, PDAPP and non transgenic (wild-type, WT) mice using different MRI techniques. We limited our investigation to the structural outcomes because definition of functional acquisition and analysis protocols are still ongoing. The **clinical** side was to evaluate and minimize the across-session test-retest reliability of brain segmentations and diffusion parameters derived from a group of different 3T MRI scanners (Siemens, Philips, GE) using elderly healthy subjects.

The work described here is structured in two sections:

**Part I: Animal imaging** Performing morphometric and diffusion analysis in transgenic mice relative to wild-type using 3D and Diffusion Tensor Imaging (DTI). We identified several structural markers sensitive to Alzheimer progression.

**Part II: Human imaging** Assessment of morphometric and diffusion measure reproducibility in 8 3T sites across Europe using 3D and DTI.

## 3 PART I: ANIMAL IMAGING

### 3.1 AD transgenic mice

Most of the commonly used Tg mice are created by deploying one, or a combination of, genes that have been found mutated in Familial AD (FAD) subjects such as APP [16, 17] and PSs [18, 19] or in the familial form of Frontotemporal Dementia such as tau [20]. While all APP and PSs Tg mouse models do not reproduce tangles, Tau Tg mice are characterized by tangles in absence of A $\beta$  (Table 1 summarize some of the most used models).

Tg line name	Genetic Mutation	Promoter	Ref
PDAPP	APP <sup>minigene</sup> (Indiana: V717F)	PDGF $\beta$	[21]
Tg2576	APP <sup>695</sup> (Swedish: K670N-M671L)	Hamster PrP	[22]
APP/PS1KI	APP <sup>751</sup> (Swedish and London: V717I) / PS1 <sup>KI</sup>	Murine Thy-1 (APP and PS1)	[23]
TASTPM	APP <sup>695</sup> (Swedish) / PS1 <sup>M146V</sup>	Murine Thy-1 (APP and PS1)	[24]
APP-PS1	APP <sup>751</sup> (Swedish and London) / PS1 <sup>M146L</sup>	PDGF $\beta$ (APP) and HMG-CoA reductase (PS1)	[25]
PS2APP	APP <sup>695</sup> (Swedish) / PS2 <sup>N141I</sup>	Murine Thy-1 (APP) and PrP (PS2)	[26]
3xTg	APP <sup>751</sup> (Swedish) / PS1 <sup>M146V KI</sup> / Tau <sup>P301L</sup>	Murine Thy-1 (APP, PS1 and Tau)	[27]
TauPS2 APP	APP <sup>695</sup> (Swedish) / PS2 <sup>N141I</sup> / Tau <sup>P301L</sup>	Murine Thy-1 (APP), PrP (PS2 and Tau)	[28]

**Table 1. Most frequently used mice models of amyloidosis.** PDGF $\beta$  (platelet-derived growth factor  $\beta$ -chain) and PrP (prion protein) result in a transgene expression inside and outside of the central nervous system. Thy-1 (thymocyte differentiation antigen 1), HMG-CoA reductase (3 hydroxy-3-methylglutaryl-coenzyme A reductase) and NSE (neuron-specific enolase) are neuronal specific.

#### 3.1.1 Models of amyloidosis

Tg mouse models mimicking amyloidosis are created deploying APP and/or PSs. APP is a member of type 1 transmembrane family of glycoproteins and is proteolytically cleaved by secretases, proteases membrane-associated.  $\alpha$ -secretase begin the nonamyloidogenic processing of APP, generating a large soluble peptide ( $\alpha$ -sAPP) and a smaller carboxy-terminal fragment (CTF- $\alpha$ ). CTF- $\alpha$  is a  $\gamma$ -secretase substrate that produces extracellular p3 and the amyloid intracellular domain (AICD). Amyloidogenic processing is started by  $\beta$ -site APP-cleaving enzyme 1 (BACE1) [29, 30], a  $\beta$ -secretase, which creates  $\beta$ -sAPP, larger

than  $\alpha$ -sAPP, and CTF- $\beta$ . Also CTF- $\beta$  is processed by  $\gamma$ -secretase producing A $\beta$  and AICD.

Although the exact physiological significance of APP and the products of its cleavage remain to be clarified, different physiological roles have been hypothesized including involvement in cell movement [31], apoptosis [32], cell differentiation [33], synaptic strength [34] and transcriptional regulation [35]. APP FAD mutations can be detected near the  $\beta$ - or  $\gamma$ -secretases cleavage sites, facilitating their activity and increasing the secretion of the longer and more toxic A $\beta$  peptides, A $\beta$ 42 [36], or within A $\beta$  sequence, majoring the capacity to form oligomers and protofibrils [37].

PSs are transmembrane proteins. Presenilin 1 (PS1) belongs to the  $\gamma$ -secretase complex with nicastrin, anterior pharynx defective 1 (APH1) and presenilin enhancer 2 (PEN2) [38, 39]. PSs are not only involved in APP processing but they are also implicated in neurotransmitter release regulation [40] and directly interact with tau and glycogen synthase kinase 3 $\beta$  (GSK-3 $\beta$ ) [41], an important enzyme involved in tau phosphorylation and essential in the pathogenesis of AD [42]. Moreover, PSs probably act as neuronal endothelium reticular calcium leak channels [43] and might play another physiological role regulating the intracellular trafficking of selected proteins [44-47]. PSs FAD mutations result in an A $\beta$  peptide generation increment and cause an imbalance in calcium signalling [48, 49].

Many Tg models have been created using different promoters, mouse strains or sequence mutations but in general the human APP or PS mutated gene overexpression results in amyloidosis which leads to the early onset of dementia [21, 22, 50, 51]. This phenomenon is even more precocious if these genes are co-expressed in the same mouse [23, 52, 53]. Unfortunately, atrophy or neuronal loss are very rare. To date, an increasing number of evidence indicates the accumulation of A $\beta$  peptides localized within the neurons as one of the earliest pathological events in AD [54]. Tg mice with intraneuronal A $\beta$  or neuronal loss are reviewed in [55]. Beside gene overexpression, another way used to study the role of the genes is the knock out technique in which specific genes are unmade. APP knock out mice are viable and fertile and show reduced locomotor activity and reduced grip strength [56]. PS1-deficient mice die perinatally probably because PS1 is involved in Notch signalling pathway [57, 58] and also exerts pleiotropic effects during brain development, including the regulation of neurogenesis. For this reason a conditional forebrain-specific PS1 knockout mouse, based on Cre/loxP system has been created. These mice are normal but deficient in enrichment-induced neurogenesis. PS2 knockout mice had no abnormal phenotypes [59], maybe because its loss of function is covered by PS1. Mice lacking both PS1 and PS2 are embryonic lethal too [60] but conditional double knockout mice lacking the PSs in the postnatal forebrain are identical to wild type until adulthood and exhibit an age-dependent AD-like neurodegenerative phenotypes [61, 62]. BACE1 null mice are viable, healthy and fertile. In their adult brains no A $\beta$  production has been detected and BACE1 deficient neurons fail to secrete A $\beta$ , even when co-expressing APP and PS1 mutant genes [63].

### **3.1.2 Models of tauopathy**

Although no tau mutations have been found in AD, NFT, the other principal pathological characteristic of this dementia is replicated in mice using modifications

in the sequence of tau protein discovered in the familial form of Frontotemporal Dementia with parkinsonism linked to chromosome 17 (FTDP-17) [20]. The microtubule-associated protein tau (MAPT) gene is located on chromosome 17 and more than 30 mutations have been linked to FTDP-17 [64]. The genetic sequence alteration influences the presence and the level of fibrillary lesions and NFTs. In normal conditions, Tau is a multifunctional protein localized to the axons where is associated with microtubules ensuring their stability and their assembly [65]. It is also implicated in axonal transport [66], elongation and maturation [67] and in facilitating tubulin acetylation [68]. HPr becomes insoluble, loses its affinity for microtubules and forms cytotoxic intermediate aggregates [69] that, successively, composed the tangles. The tau phosphorylation status depends on the balance between kinases and phosphatases activity and the principal kinases involved in tau modifications are GSK-3 $\beta$  [42] and Cyclin-dependent kinase 5 (Cdk5) [70, 71]. In adult human brain six tau isoforms exist, all of them have been found in a hyperphosphorylated state in neurofibrillary lesions of AD patients [72].

Tau animals, like amyloidosis models, have been commonly created using knockout or overexpression techniques. The former seem linked to normal development and mild cognitive deficits although embryonic hippocampal cultures from these mice show a significant delay in maturation [67], the latter are linked to different phenotypes depending on the transgene and its promoter (for a review see [73]). An alternative approach is to create mouse models overexpressing kinases involved in tau phosphorylation [74, 75].

### **3.1.3 Models of amyloidosis and tauopathy**

The triple transgenic mouse model (3xTg) seems to be the model which better reproduces the signature lesions of AD because of the development of both A $\beta$  and tangles [28]. Interestingly, A $\beta$  induces NFTs formation only in mice carrying the mutant form of human tau and not the human wild type sequence. This is different from AD patients situation, where A $\beta$  aggregation and NFT formation occur in the absence of tau pathogenic mutations [76].

## **3.2 Tg as model of preclinical AD**

### **3.2.1 Neuritic alterations**

Neuritic alterations are associated to transport impairment of lipids components and membranes proteins along the axons, a critical issue for neuronal functioning known as fast axonal transport (FAT). FAT is accountable for the delivery of different elements and subcellular structures, such as mitochondria and synaptic vesicles, from the sites of their synthesis to their final destination. Histological analysis of many mouse models found dystrophic neuritis around and within the A $\beta$  deposits [21, 26, 27, 77, 78].

To date, advanced neuroimaging techniques are possible for the *in vivo* analysis of neuritic structure and functionality of AD animal models, such as Tg mice. DTI allows the description of tissue microstructures exploiting the diffusion properties of water [79] will be deeply discussed in the section “Structural outcomes” (pag 14). MRI using manganese (Mn<sup>2+</sup>) as contrast agent (MEMRI: Manganese-Enhanced MRI) is used to identify and quantify the difference in axonal transport rates *in vivo* because the paramagnetic ion Mn<sup>2+</sup> was transported along microtubules via FAT. A



study on Tg2576 showed an age-dependent decrement in the axonal transport rate within Tg as well as a difference between Tg and controls, with a lower axonal transport rate in the Tg (81). It was hypothesized that the decrease in axonal transport was related to plaques formation. Although mutated tau alone led to axonal transport deficits [80, 81] wild-type tau deletion [67, 82] or overexpression [82] were ineffective. Loss of wild-type tau expression had a very different impact when mutated APP co-exists [83]. In the Tg2576 for example, extensive degeneration of cortical and subcortical neurites, not normally observed, an increase in A $\beta$  peptide and more severe cognitive deficits were detected. A recent MEMRI-study showed that FAT was reduced by 50% in APP knock out mice since early-life [84]. This condition was ameliorated by co-overexpression of human wild-type tau and was exacerbated by mutated tau. *In vitro* studies reported deleterious effect of A $\beta$  oligomers on both axonal transport and tau physiological properties [85-87]. Moreover, a convergent role of PS and tau in axonal transport and neuronal survival and function was proposed [88]. Misregulation of both genes in the same mouse accelerated neurodegeneration and tau phosphorylation, at least at peripheral level. PS1 FAD-mutations were associated with increase in kinesin1 phosphorylation by GSK-3K followed by kinesin1-vesicles complex disassembling and kinesin1 degradation [89], leading to FAT impairment of specific membrane proteins, such as APP and TrkR, neurotrophins and mitochondria. Transport alterations might arise not only as a consequence of molecular transporters defects but also from alterations in the actin cytoskeleton. Recently, a growing body of evidence has brought to light an active role of A $\beta$  in cytoskeletal abnormalities [90]. According to the results, A $\beta$ 42 might induce the formation of rod-shaped actin bundles (rods) that would be able to sequester the phosphorylated form of tau [91]. Blockage and inhibition of neuritic transport were associated with axonal swelling where the local accumulation of APP, A $\beta$  and vesicles lead to synaptic failure and neurodegeneration [92, 93].

### 3.2.2 Synaptic dysfunction

It has been demonstrated that synapses loss precede neuronal degeneration in AD [94, 95]. Synapses damage is experimentally associated with loss of synaptic marker or with loss of synaptic plasticity. Synaptic markers can be divided in (i) presynaptic, such as synaptophysin, an indicator of the presynaptic terminal density, and (ii) postsynaptic, such as AMPA and NMDA receptors (AMPA and NMDAR, respectively), indices of the dendritic spines density. Long term potentiation (LTP) and depression (LTD) are forms of long-term plasticity while paired-pulse facilitation (PPF) and depression (PPD) are forms of short-term plasticity and have been used to monitor the synaptic changes.

LTP observed in CA1 region of hippocampus is only one of the forms of long term synaptic plasticity depending on functionality of the medial temporal lobe and known to be impaired in MCI subjects [96]. Synaptic plasticity is related to the cellular changes involved in memory formation and, being its impairment involved in the precocious AD phases, the understanding of its biological mechanisms could supply new therapeutic targets.

APPPS1-21 mice resulted in an age-related CA1 LTP impairment, probably dependent on plaque formation, and in a PPF impairment at 15-months of age [97]. In these mice, hippocampal A $\beta$  deposits emerging at 4 months were surrounded by

synaptophysin-positive dystrophic terminals and boutons and hyperphosphorylated tau-positive neuritic structures [98]. Before plaque deposition, old Tg2576 [99] and homozygous APP/PS1KI (with 2 knock-in PS1 alleles) [100] exhibited hippocampal LTP impairment together with impaired performance in working memory tasks. In Tg2576 mice these deficits were probably related to a decline in functional synaptic plasticity because synaptic transmission was maintained (minimal or no loss of hippocampal presynaptic and postsynaptic structures were identified) [24, 99]. Another study applying the same model (Tg2576) reported opposite results namely normal LTP and synaptic transmission impairment [101]. In APP/PS1KI 6-months old, the levels of pre and postsynaptic markers considered were significantly decreased in the synaptosome-enriched protein fraction indicating a synaptic transmission damage. APP/PS1KI was a suitable model to study early A $\beta$  peptides effects on brain cell populations in so far A $\beta$ 42 comprised 85% of total A $\beta$ , consisting of full length and heterogeneous N-terminal modified variants. These mice exhibited hippocampal atrophy [100] and severe learning deficits [102] already at the age of 6 months and neuronal loss pattern matched better with oligomers distribution rather than with plaques. Since APP products were detectable already at 2 months, the authors speculated the existence of a narrow period for the onset of the synaptotoxic effects. Interestingly, hemizygous APP/PS1KI (with 1 knock-in PS1 allele) and PS1KI mice exhibited normal LTP, maybe related to low expression of endogenous murine PS1, considering that PS FAD mutations were able to produce synaptic plasticity impairment [103]. Old PS2APP showed significantly enhanced PPD and no difference in LTP when compared with WT [26]. In contrast, no difference in the levels of hippocampal LTP and basal transmission between Tg and WT was found in APPsw/PS1A246E mice [104] suggesting the presence of an intact machinery for induction and expression of LTP at CA1 synapses in this model. The involvement of A $\beta$  in synaptic degeneration was further confirmed by a new mouse model of oligomer-induced pathology lacking plaques until 24 months of age [105] and by a study where the treatment with a  $\gamma$ -secretase inhibitor improved synaptic function and plasticity in Tg2576 within days [106].

In htau mice, a mouse model in which the mouse tau gene was replaced by a non-mutated human tau gene, an age-dependent learning impairment dependent on disruption of synaptic functions was shown, concomitant to tau pathology and not to neuronal death [107]. PS19 mice, a model with mutated tau, showed synaptic pathology in the CA1 hippocampal region at 6 months of age (before neuronal loss and NFT formation) consisting in basal synaptic transmission impairment, presynaptic dysfunction and LTP deterioration [108]. In another study, two new inducible tau mouse models were created using a "pro-aggregation" and an "anti-aggregation" sequence [109]. In both mutants, mutated Tau induced missorting of tau in somatodendritic compartments and bound equally well to microtubules. Only the pro-aggregation model showed tau aggregation proceeding to a pre-tangle oligomeric state. The decline in number of synapses was most pronounced with the pro-aggregation form and the authors concluded that synapses loss is related to aggregation of tau rather than to its missorting. All Tau-induced pre-tangle changes were reversible when the expression of Tau was turned off.

An LTP age-dependent reduction correlating with intraneuronal A $\beta$  was revealed in CA1 region of the hippocampus in older 3xTg compared to WT. The PPF was unaffected (68). Despite this hippocampal synaptic plasticity impairment occurring before plaques and NFTs development, the synaptic vesicle recycling was not affected [110] even if morphological changes were reported [111]. In another 3xTg the reduction in both soluble A $\beta$  and tau levels, but not A $\beta$  alone, was followed after immunotherapy by cognitive function improvement suggesting a synergistic actions of A $\beta$  and tau in cognitive decline [112].

Thus, both tau and A $\beta$  seem to be directly involved in synaptic decay but the exact cellular mechanisms is unknown. A $\beta$  oligomers, rather than plaques [113], monomers or fibrilles, block LTP [114] and reduce the density of dendritic spines and numbers of electrophysiologically active synapses [115]. Several mechanisms of oligomers toxicity have been proposed including a possible interference with the cholinergic signalling pathway [116-119] and/or alteration of the glutamatergic transmission [120-123] and/or, even the damaging of the calcium balance (88), essential for LTP induction. The role of tau in this scenario is not clear. In reality, in AD patients tau accumulates in the somatodendritic compartment and neurofibrillary tau deposits correlates better than A $\beta$  with neuronal loss [124] and with the severity of the dementia [125].

### **3.3 Imaging markers**

MRI is a non invasive technique that permits the quantification of the structural profile in vivo and in vitro and has been widely used to characterize AD disease in human. Advanced in this field make MRI applicable in mice as well as in humans allowing comparative studies among different Tg and translatable studies between human and mice throughout the progression of the disease.

#### **3.3.1 Structural outcomes**

##### **3.3.1.1 Structural MRI**

Neuroimaging markers are among the most promising candidates to track disease progression [126]. Indeed, whole brain and hippocampal atrophy are two of the most validated surrogate outcomes for clinical trials [126]. Hippocampal atrophy detected by MRI has recently been accepted by European Medicines Agency (EMA) for use in clinical trials in pre-dementia stage of AD (EMA/CHMP/SAWP/809208/2011). AD is characterized by grey matter loss in specific regions such as hippocampus, lateral and medial parietal, posterior cingulate and lateral temporal cortices, useful for defining the pathology and tracking its progression [127].

Atrophy in mouse models using imaging techniques is difficult to identify, both because in many models is not present or is not enough extensive to involve the whole structure volume and because often the volumes differences are related to development defects and not to amyloid pathology. For these reasons, each Tg has a specific structural alteration signature. Two approaches are generally used to calculate the anatomy structures volumes, one relies on manual segmentation and the other take advantage of automatic tools. The first one is more accurate but is time-consuming, operator-dependent and measures only few regions of interested (ROI), the second considered much more anatomical regions independently of a

*priori* hypothesis but its use is challenging because of brain variations. Mice carrying a single APP mutation were analyzed applying the manual ROI definition approach with different results. PDAPP showed hippocampal volume deficits probably due to a continuous hippocampal development in controls that did not happen in Tg [128]. In APP-Au model, characterized by intracellular A $\beta$  accumulation in absence of plaques, volume reduction in the whole brain and in the cortex but not in the hippocampus were observed [129]. PS2APP did not show any volumetric difference in whole brain and ventricles [130]. In APPPS1 brain size reduction and CSF volume increase in old mice were detected but atrophy concerned mainly posterior brain areas not usually involved in AD [25]. To overcome the limitations of manual ROI approach, non-biased automated methods have been introduced. Brain volume increase is reported in APP/PS1 [131] and TASTPM [132]. In the former the hippocampus is smaller than in control, whereas in TASTPM the hippocampal formation enlarges. In general, MRI imaging is useful to differentiate Tg and controls but the hippocampal volume deficits detected are ascribable to development rather than pathological factors. Anyway, a mouse model where the disease started after the brain was fully mature was analyzed immediately before and shortly after the onset of amyloid formation [133]. These mice were created using a system that permit the temporal control of the mutated APP expression through the administration of a drug. Drug removal, and consequent transgene expression, was performed after 6 weeks of life. The authors found volume reduction in whole brain, cortex and hippocampus before amyloid deposition. Moreover, volumetric losses identified in regions not normally considered because not directly AD-associated, predicted locations of amyloid formations at later stages of the disease. This model reproduce many futures of the human disease and could be good to study pre- and post-amyloid volumetric changes. This proves the enormous potentiality of automated methods showing unexpected sites of degeneration and allowing the study of their role and their connections in the progression of the pathology. Figure 2 summarized the comparison of the structural markers results between human and mice.

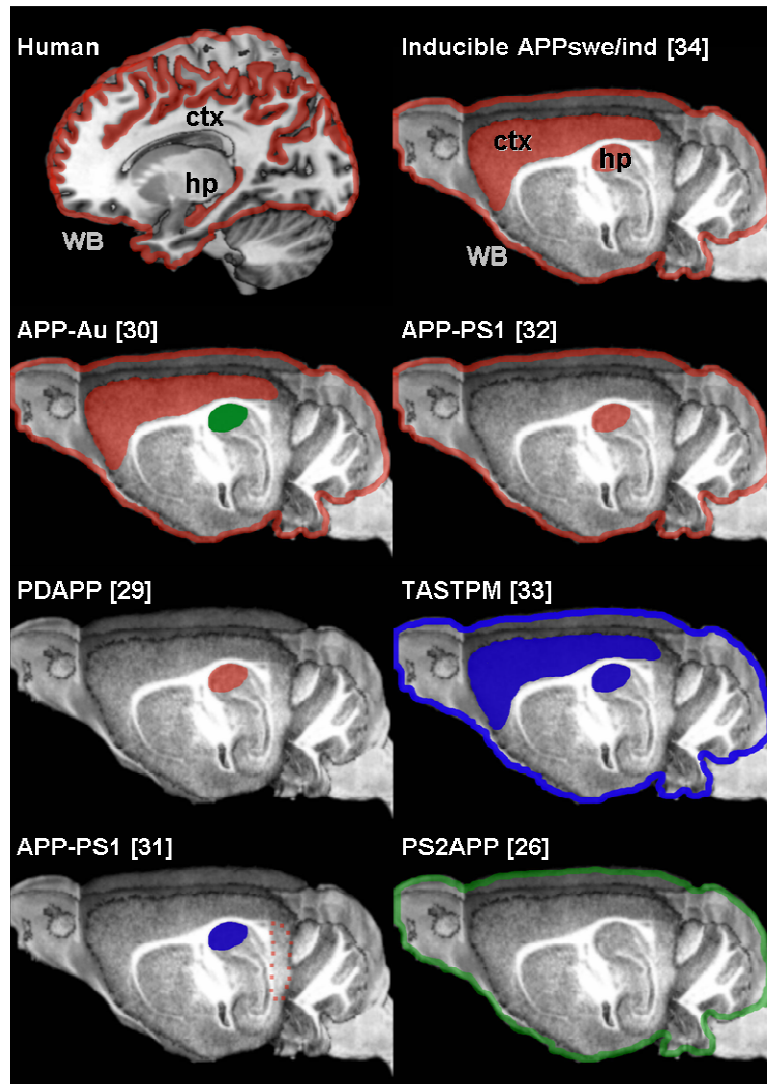


**Figure 2. Structural markers in humans and mice.** In humans, grey matter loss in regions such as hippocampus (hp), cortices (ctx) and whole brain (WB) is useful for defining the AD pathology and tracking its progression. The brain morphological alteration of Tg mice are linked with neurodevelopmental rather than neurodegenerative factors. Indeed, each Tg has a specific structural alteration signature and are described one by one. Volume decrease and increase are represented in red and blue colours respectively while no differences between Tg and controls are illustrated in green. Continuous line represents whole brain (WB), dotted line only posterior brain. The only mouse model exhibiting hippocampal volume decrease and deficits in cortical volume detected using MRI is the Inducible APPswe/Ind, where pathology develops when the brain has reached fully maturity.

### **3.3.1.2 Diffusion Tensor Imaging (DTI)**

DTI is a quantitative MRI technique that allows the description of tissue microstructures exploiting the diffusion properties of water and the detection of white matter lesions. DTI parameters commonly obtained from DTI image analysis are fractional or relative anisotropy (FA or RA, respectively), which are measures of tissue integrity, mean diffusivity (MD), trace and apparent diffusion coefficient ( $ADC = \text{Trace}/3$ ), which evaluate the total water diffusion, axial ( $\lambda_{||}$ ) and radial ( $\lambda_{\perp}$ ) diffusivity, indices of axonal injury and demyelination, respectively.

In human, white matter lesions such as atrophy of the corpus callosum as well as MD and anisotropy alterations are higher in AD than in healthy subjects [134] and DTI parameters changes in the medial temporal lobe (parahippocampus [135] and posterior cingulum [136]) and hippocampus [137] seem promising markers for disease progression.

Analysis of different white matter tracts of PDAPP mice revealed significant decrease in RA and increase in Trace and radial diffusivity in 15-month-old Tg [138]. Despite A $\beta$  was detected in cortex, hippocampus and, to a lesser extent, within the external capsule of old Tg no correlation between RA values and A $\beta$  load was found. Tg2576 was examined considering also several grey matter regions [139]. When A $\beta$  deposition was known to increase, differences in DTI indices values became detectable, especially in the corpus callosum. A correlation test between A $\beta$  load and DTI indices was not performed because of the limited number of mice considered in the study. However, a positive relation between cortex trace and A $\beta$  load was observed. Analysis of TgCRND8 applying diffusion-weighted imaging (DWI) did not find significant changes in ADC in all the grey matter regions considered [140]. One explanation could be the different and less informative technique used instead of DTI. Future studies with automated approach could reveal unexpected group differences in white and grey matter diffusion abnormalities impossible to detect with manual procedure.

Several similarities has been found between human and mice, specially in white matter regions. The difficulty to define valid DTI outcomes begin from human field and rely on the lack of longitudinal studies, the impossibility to correlate DTI parameters changes to histological sections and the absence of a complete agreement between all the literature reports. In this scenario mouse models become essential given that histological evaluation, hence A $\beta$  and DTI indices variation correlation, is possible.

### **3.3.2 Functional or metabolic outcomes**

Cerebral metabolism and blood perfusion correlate better than A $\beta$  load to cognitive status in AD patients [141]. Glucose uptake can be evaluated with FDG autoradiography or PET, while blood perfusion or metabolites concentration analyses with MRI.

#### **3.3.2.1 Glucose uptake**

FDG uptake is believed to reflect synaptic activity [142]. Human PET studies in AD patients found progressive glucose uptake impairment in the hippocampus, followed by fronto-temporal (FT) and posterior cingulate cortices (PCC) [143]. Cerebral metabolism decline in the entorhinal cortex and hippocampus can

discriminate MCI patients that will convert to AD from MCI that will not convert [144].

An age-dependent increase of FDG uptake was reported in the cortex and hippocampus of APPPS1 [145]. Other two FDG-PET studies were performed in Tg2576. One did not detect appreciable differences between Tg and control [146]. The other revealed an abnormal hypermetabolism at least until 7 months of age [147], a completely different situation from the human condition. These data suggest that Tg2576 are not a reliable model to study neuronal metabolism and that PET *in vivo* applications in mice are probably still limited.

FDG autoradiography, with its higher resolution, is a valuable alternative to PET. This technique in aged PDAPP showed a significant reduction in whole brain and PCC FDG-uptake when compared with young Tg and age-matched controls [148]. This progressive decline in PDAPP was not linear during aging but, noteworthy, PCC metabolic deficits appeared before amyloid deposition and seemed to be related to memory deficits [149]. Morphological analysis had indicated important developmental defects in these mice, which could confound the metabolic results. Mice without severe cerebral alterations were evaluated. Analysis of old PSAPP demonstrated reduced FDG uptake in PCC and retrosplenial cingulate gyrus [150] but a longitudinal study supporting the progressive reduction has not yet been performed. FDG-autoradiography in a triple Tg mice (3xTg), carrying plaque and tangles, showed hypometabolism in all measured regions, including cortical and subcortical gray matter, cerebellum and brainstem [151].

#### **3.3.2.2 Brain perfusion**

Brain perfusion is a marker of neuronal activity. Cerebral blood volume (CBV) and cerebral blood flow (CBF) assessment based on magnetic resonance, provide information similar to FDG-PET in patients [152]. Cerebral hypo-perfusion on single photon emission tomography (SPET) in the posterior temporo-parietal lobes, is a consistent finding in AD patients [153] and has been correlated with Braak pathological stages [153] and with cerebrospinal fluid (CSF) biomarkers [154].

Because of the small size of the mouse brain, the discrimination of brain regions (ROI) is difficult. Anyway, an interesting cross-species study between humans and a mouse model expressing a double APP mutation showed a similar pattern of CBV defects in the hippocampal formation of both [155]. Prominent CBV dysfunction in the entorhinal cortex in mice was rescued by chronic administration of a drug that reduced A $\beta$ -related neurotoxicity. These results point out that CBV is a functional imaging marker able to detect A $\beta$ -hippocampal dysfunction even in the absence of cell death or NFT. Reduced blood perfusion was demonstrated also in the cortex of APPxPS1-KI, a model featuring, among others, hippocampal cell loss [156]. Whether this cerebral blood reduction was due to cell loss and/or to cerebral abnormalities still has to be explored, however similar findings were reported in the cortex of single APP transgenic mice (Tg2576) [157] where the cell loss has not been described. Superoxide dismutase 2 (SOD-2) co-expression conferred these mice protection against vascular and neuronal deficits suggesting a possible important role of reactive oxygen species in A $\beta$  neurotoxicity. A study in PS2APP found reduced blood supply in the occipital cortex compared to controls, already at an early age [158] but these results were not confirmed by another group [28]. The reason is probably related to the different genotype of the two models, the former

being homozygote and the latter heterozygote for PS2APP. Perfusion deficit was described also in the dorsal cortical area of TauPS2APP at the age of 15 months when compared to Tau single mutant [28] and in the hippocampus of another 3xTg [159]. Figure 3 summarizes the comparison of the functional markers results between humans and mice.

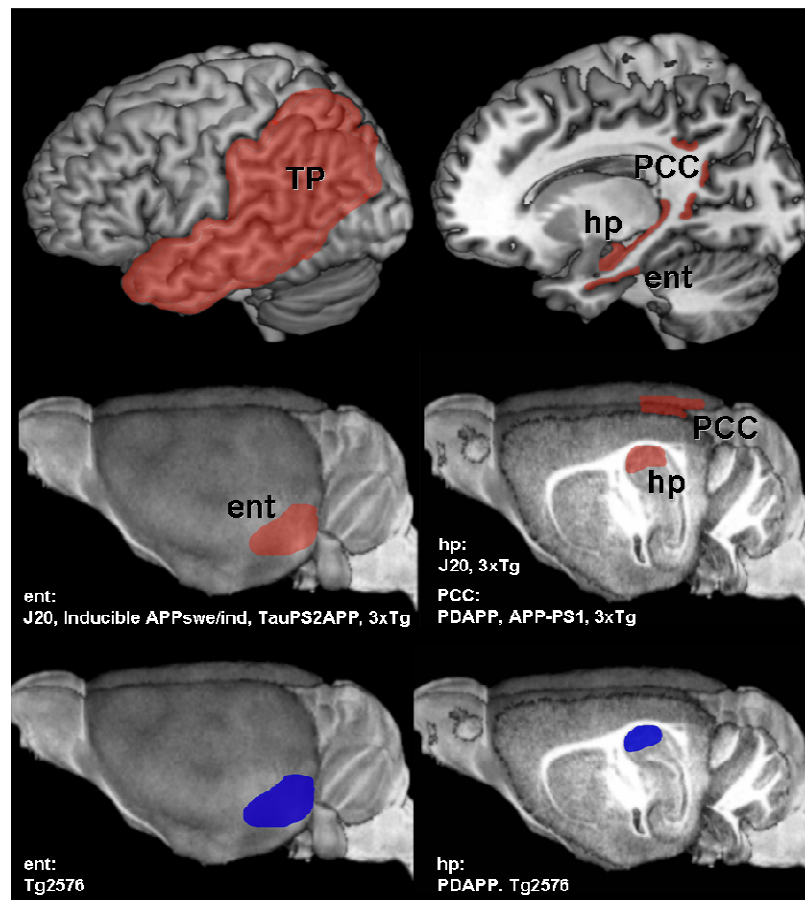


**Figure 3. Functional and metabolic markers of preclinical AD in humans and homologous markers in Tg mice.** Neuronal functionality is compromised many years before the appearance of clinical symptoms. Human studies found progressive functional impairment in the hippocampus (hp), posterior cingulate cortex (PCC), entorhinal cortex (ent) and temporo-parietal cortex (TP) of AD patients. The same areas were investigated in transgenic mice. Top: Functional markers of preclinical AD in humans. Middle: Mice strains where functional markers homologous to humans have been identified (e.g. metabolic deficits in the hippocampus of J20 and 3xTg mice). Bottom: Mice strains where the same markers have been evaluated giving opposite results in comparison with humans. Markers decrease and increase are represented with red and blue colours respectively.



### **3.3.2.3 Spectroscopy (MRS)**

MRS identifies and tracks neurochemical changes of biochemical metabolites such as N-acetylaspartate (NAA) or myo-inositol (mIns). NAA is mainly located in neuronal cells and its reduction had generally been accepted as an indicator of neuronal dysfunctions. mIns is primarily present in the glial cells and elevation of its levels is associated to glial proliferation and inflammation. Compared to the NAA and mIns, choline (Cho), another compound considered in MRS analysis is present at low concentrations in brain tissue. Increased levels of Cho in AD has been correlated to the chronic deficiency in acetylcholine production and neurodegeneration.

Human spectroscopy studies showed decrease in NAA in the posterior cingulate gyrus and medial temporal lobes of people with MCI as much as in patients with AD [160] and increase in mIns in the parietal lobes of MCI and mild AD [161].

A reduction in NAA and glutamate (Glu, another neuronal marker) was obtained in the cortex and hippocampus of aged APP-PS1 [162, 163] and their levels correlated with increasing brain amyloidosis. No differences in mIns between Tg and controls was reported [162] until 400 days of age when an increase was detected [163]. Stable mIns levels, decrease of the NAA and increase of choline (Cho) and taurine intensity were reported in the cortex of old Tg2576 [164]. Rodent taurine might perform a role similar to human mIns. PS2APP [130] revealed stable NAA and Glu during the first 12 months of age that significantly decrease at 24 months. An increase in mIns was detected in old Tg but the variability was too high to be statistically significant. Limiting factors in the translational application of MRS are the difficult to obtain good spectra in mice due to the small murine brain size and the cross-species metabolic profile differences.

### **3.4 Part I: animal imaging study goals**

We limits our investigation to the structural outcomes because definition of functional acquisition and analysis protocols is still ongoing. We analyzed in details morphometric and diffusion changes of three different mouse models of AD such as TASTPM, TauPS2APP, PDAPP and WT at 5 ages using different MRI techniques. The morphometric data evaluated includes subcortical, ventricular and intracranial volumes as well as entorhinal thickness while the diffusion parameters were FA, MD,  $\lambda_{||}$  and  $\lambda_{\perp}$  in white and grey matter regions.

### 3.5 Materials and Methods

#### 3.5.1 Animals

Experiments were conducted with PDAPP, TASTPM, TauPS2APP mutant mice (see Table 1 in the Introduction for genetic details and Fig. 1b for phenotypic features) and non transgenic C57/BL6 (WT). Mice were longitudinally or cross-sectionally followed from 3 to 22 months (for number per age, gender and study design, please refer to table 2). All mice were housed under a 12 hour light and 12 hour dark and fed with standard laboratory chow and water *ad libitum*.

Number of mice per age (females)						Study design
	3 Months	9 Months	13 Months	18 Months	22 Months	
<b>TASTPM</b>	<b>20 (8)</b>	<b>15 (5)</b>	<b>15 (4)</b>	<b>15 (4)</b>	<b>12 (3)</b>	<b>CS</b>
<b>WT</b>	<b>20 (10)</b>	<b>20 (10)</b>	<b>20 (10)</b>	<b>18 (9)</b>	<b>20 (10)</b>	
<b>TauPS2APP</b>	<b>28 (14)</b>	<b>28 (14)</b>	<b>26 (13)</b>	<b>26 (13)</b>	<b>17 (10)</b>	<b>LG</b>
<b>WT</b>	<b>20 (10)</b>	<b>20 (10)</b>	<b>20 (10)</b>	<b>14 (10)</b>	<b>10 (4)</b>	
<b>PDAPP</b>	<b>10 (0)</b>	<b>12 (0)</b>	<b>11 (0)</b>	<b>11 (0)</b>	<b>10 (0)</b>	<b>CS</b>
<b>WT</b>	<b>10 (0)</b>	<b>11 (0)</b>	<b>10 (0)</b>	<b>7 (0)</b>	<b>3 (0)</b>	

**Table 2.** List of the transgenic mice and their respective controls included in this study, specified by animals per age, gender and study design. Abbreviations: CS= cross-sectional; LG= longitudinal.

#### 3.5.2 MRI animal preparation

The animals were initially anesthetized with isoflurane (5% for induction and 1% during the set-up) in a mixture of O<sub>2</sub> (30%) and NO<sub>2</sub> (70%) gases, delivered to the nose cone for spontaneous respiration throughout the experiment. Stereotaxic hear bars were used to minimize movements during the imaging acquisition. Temperature was maintained at ~37°C by a feedback-controlled, water circulated heating cradle.

#### 3.5.3 MRI acquisitions

MRI was performed using a 7T small bore animal Scanner (Bruker Biospec, Ettlingen, Germany). Two actively coupled radio frequency (RF) coils were used: a volume coil with a 7.2 cm diameter used as the transmitter and a 1 cm surface coil diameter positioned on the top of the animal's head as the receiver. The ParaVision 5.1 software interface (Bruker BioSpin, Ettlingen, Germany) was also used for data acquisition.

A 3D RARE T2-weighted sequence allowed the acquisition of 102 sagittal slices with 147 µm thickness, which covered the whole mouse brain volume. The morphological images were obtained with an in-plane resolution of 117 x 147µm (matrix 256 x 102 and a Field of View (FOV)= 3 x 1.5 cm); repetition time (TR)=2500 ms, echo time (TE)=10 ms and a RARE factor of 16, for 1 average.

The diffusion-weighted acquisitions were gained using DTI EPI sequence which covered the whole brain except for the cerebellum. The diffusion-weighted images were acquired with matrix 140 x 140, FOV= 2 x 2 cm, TR= 3000 ms, TE= 36 ms, slice thickness 1 mm, b value= 800 s/mm<sup>2</sup>, one b0 image, 19 gradient directions and 4 averages.

For T2 measurements a multislice multiecho sequence was used with the following parameters: 20 TE equally separated by 11 ms, TR = 2500 ms, FOV = 2 x 2 cm<sup>2</sup>, matrix 256 x 256, slice thickness = 1 mm, acquisition time = 8 min.

### 3.5.4 Data post-processing

#### 3.5.4.1 Volumetric data analysis

The volume measurement of structural MRI images were obtained using a Java-based custom made software. Regions of interest (ROIs) were manually drawn by a trained expert and traced on the images for quantitative comparison of the brain atrophy of different regions. For each animal the ROIs were chosen following the definition of mice brain structures in the Paxinos' atlases [165].

We studied the cortex, the hippocampus, the caudate-putamen, the olfactory bulb, the ventricular system, the whole brain and the total intracranial volume (Fig 4). The cortex was divided into frontal cortex (from Bregma 3.20 mm to Bregma 1.54mm) and the rest of the cortex. Data from all the animals were obtained by averaging the values calculated multiplying the total ROI area for the slice thickness. We manually traced the total intracranial volume, the whole brain, the hippocampus and the olfactory bulb on the sagittal view; the other regions were traced on the coronal view.

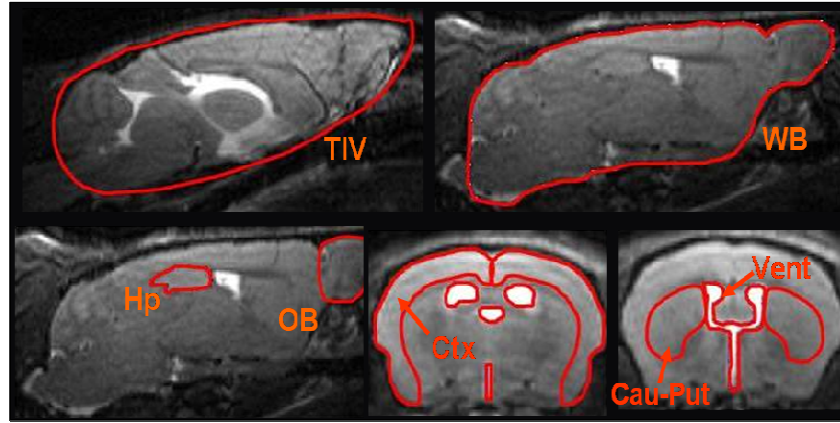


**Fig 4.** Some examples of sagittal (first row and bottom left) and coronal (second row middle and right) images of a young WT are shown with overlay of the masks used for the manual volume segmentation. Abbreviations: Cau-Put= caudate-putamen, Hp= hippocampus, OB= olfactory bulb, ctx= cortex (except the frontal), Vent= lateral, third and fourth ventricles, WB= whole brain, ICV= intracranial volume.

### **3.5.4.2 Diffusion data analysis: estimation of structural connectivity measures**

#### **3.5.4.2.1 Tract-Based Spatial Statistics (TBSS)**

In order to reliably process the FA images, we developed a processing pipeline based on a modified version of the user-independent method TBSS. The processing stream consists in the following steps: (i) FA template computation by iterative affine registration of the individual FA images; (ii) individual FA maps projection into the reference space of the template; (iii) skeletonization of the template and choice of a threshold value (usually 0.2); (iv) group-wise voxel-by-voxel comparison of the FA distributions; (v) analysis of the other DTI indices maps. The statistical significance was assessed at  $p < 0.05$  corrected by multiple comparisons.

#### **3.5.4.2.2 ROI-based analysis**

Each diffusion-weighted series was used to compute the six independent components of the diffusion tensor. The three eigenvalues ( $\lambda_1, \lambda_2, \lambda_3$ ) and the eigenvectors of the resulting tensor map were derived by matrix diagonalization [79]). The DTI indices FA, MD ( $10^{-3} \text{ mm}^2/\text{s}$ ),  $\lambda_{II}$  ( $10^{-3} \text{ mm}^2/\text{s}$ ) and  $\lambda_{\perp}$  ( $10^{-3} \text{ mm}^2/\text{s}$ ) are defined by the following equations:

$$FA = \frac{\sqrt{3}}{\sqrt{2}} \frac{\sqrt{(\lambda_1 - \bar{\lambda})^2 + (\lambda_2 - \bar{\lambda})^2 + (\lambda_3 - \bar{\lambda})^2}}{\sqrt{\lambda_1^2 + \lambda_2^2 + \lambda_3^2}} \quad (1)$$

$$MD = \frac{\lambda_1 + \lambda_2 + \lambda_3}{3} \quad (2)$$

$$\lambda_{II} = \lambda_1 \quad (3)$$

$$\lambda_{\perp} = \frac{\lambda_2 + \lambda_3}{2} \quad (4)$$

The FA, MD,  $\lambda_{II}$  and  $\lambda_{\perp}$  maps were obtained using the FMRIB Software Library (FSL, University of Oxford, UK). ROIs were manually drawn by a trained expert and traced on the the coronal view of the colour coded map and using a mouse brain atlas [165] as reference. For the white matter structures we studied corpus callosum, anterior capsule, external capsule, cerebral peduncle, fimbria and internal capsule. For the grey matter we focused on hippocampus, frontal cortex, thalamus, caudate-putamen and olfactory bulb regions (Fig. 5).

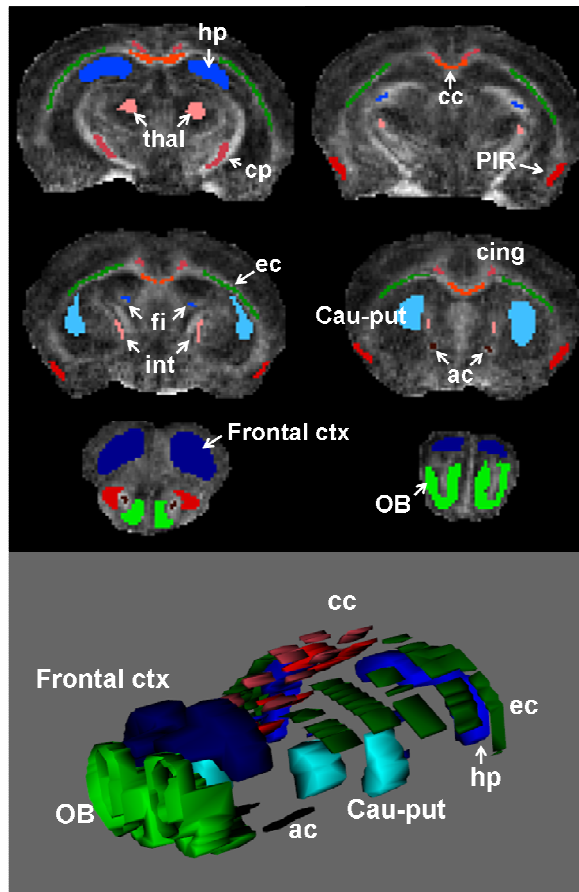


**Fig 5.** Examples of coronal color-coded images of a young WT are shown with the overlay of the masks used for the manual diffusion quantification (black background) and 3D masks visualization (grey background). Abbreviations: cc= corpus callosum, ac= anterior commissure, cc= corpus callosum, cp= cerebral peduncle, ec= external capsule, fi= fimbria, int= internal capsule, Cau-Put= caudate-putamen, hp= hippocampus, OB= olfactory bulb, Frontal ctx= frontal cortex, Thal= thalamus, PIR= piriform cortex.

#### **3.5.4.3 Entorhinal cortex thickness measurement**

The thickness of the entorhinal cortex was measured in WT and Tg mice to identify structural differences. We chose a reference image between all the coronal acquisition. Then we registered all the other images to the reference one in order to avoid bias due to bad head positioning during the acquisition. For the image registration we used FLIRT (FMRIB's Linear Image Registration Tool), a fully automated robust and accurate tool for linear (affine) intra- and inter-modal brain image registration. We used a 3D to 3D rigid body registration with 6 degree of freedom. 9 coronal slices were selected at the level between Bregma -2.75 mm

and Bregma -3.80 mm based on mouse brain atlases (Paxinos and Franklin, 2003; Paxinos et al., 2006), and the thickness was measured below the rhinal fissure [166] (Fig. 6). The measures were repeated 6 times (3 for the left and 3 for the right hemisphere) by a trained expert and the values were averaged to get the final values.

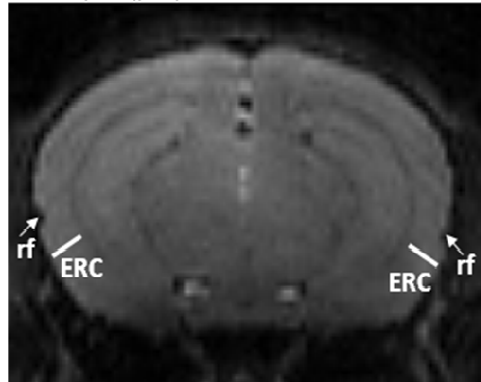


**Fig 6. Entorhinal cortex (ERC) thickness definition shown on a coronal image of a WT mouse. Abbreviation: rf = rhinal fissure.**

### 3.5.5 Histology and immunohistochemistry

A subset of mice was deeply anesthetized with equitiesin and was transcardially perfused with 0.1 M phosphate-buffered saline (PBS), pH 7.4 for histological analysis. The brains were then removed and postfixed for 2 h at 4°C in 4% paraformaldehyde. In order to cryoprotect the tissues, brains were immersed in 20% sucrose at 4°C overnight (o/n) and then frozen. Sagittal sections were prepared using a Leica cryostat using a slice thickness of 20 µm. Amyloid plaques deposition was detected using 6E10 antibody (1:500; Signet, Dedham, MA), astrocytes with GFAP antibody (1:2500; Chemicon, Billerica, MA), and microglia with Cd11b antibody (1:1000; BD, Italy) and myelinated axons with gold chloride staining (Sigma; Italy). Slices were placed on gelatin-coated glass and dried overnight at room temperature (RT) for Gold Chloride staining while they were processed in 24-well plate (free-floating) for 6E10, GFAP and CD11b antibodies. Sections were then dehydrated using successively increasing percentages of ethanol, cleared with xylene and then covered with DPX.

#### 3.5.5.1 6E10, GFAP and Cd11b antibodies

Prior to immunostaining, sections were washed 3 × 5 min in PBS and then incubated with 1% H<sub>2</sub>O<sub>2</sub> (Sigma, St. Louis, MO) in order to quench endogenous peroxidase activity.

Tissues were then incubated with blocking-permeabilizing solutions containing 10% normal goat serum (NGS) for plaque staining and also 0.4% Triton-X100 for glial cell staining. Incubation lasted 1 hour at RT. Following, sections were incubated with the appropriate antibody dilutions overnight on an orbital shaker at 4°C.

The day after, brain slices were washed 3 × 5 min in PBS prior to incubation with the appropriate secondary antibody at a 1 : 200 dilution for 1 hr. Immediately after, sections were washed 3 × 5 minutes in PBS and were incubated in Vectastain ABC kit (Vector Labs, Burlingame, CA) in PBS for 1 hour.

Sections were then washed 2 × 5 minutes in PBS and 1 × 5 minutes in Tris-buffered saline (TBS) and developed with 3,3'-diaminobenzidine tetrahydrochloride (DAB, Sigma, St Louis, MO). For comparison across different ages, sections from animals of different ages were immunostained at the same time.

#### **3.5.5.2 Gold-chloride**

Sections were immersed in PBS containing 0.2% gold chloride (Sigma, St Louis, MO) for 14 hours. Tissues were then removed and washed twice for 10 minutes with PBS and once in 2.5% sodium thiosulfate anhydrous.

#### **3.5.6 Statistical analysis**

Analysis of the MRI and T2 data were conducted using GraphPad Prism 5 software. The two-square root transformation was used to normalize the volumetric data. To compare volumes and DTI parameters among WT and Tg mice two-way ANOVA analysis followed by Hochberg post-hoc test was applied. Statistical significance was established as \* $P < .05$ ; \*\* $< .01$ ; \*\*\* $< .001$ . Descriptive statistics were illustrated using means and standard deviation for each age/genotype group's values and only significant differences between genotype are shown.



### 3.6 Results

A comparison of the changes in time across these mouse models was also evaluated. In particular, we examined the history of structural and diffusion brain changes of TASTPM, TauPS2APP, PDAPP, C57/BL6 mice using in vivo MRI. For a quantitative assessment of genotype differences, the subcortical, cortical, ventricle, intracranial volumes and white and grey matter diffusion parameters have been examined for each mouse. TauPS2APP and their controls were followed longitudinally while the others, due to the small number of animals, were followed cross-sectionally. The ages considered were five (3, 9, 13, 18 and 22 months).

#### 3.6.1 TASTPM

##### 3.6.1.1 Morphometry results

**Table 3** presents the group mean volumetric and ERC thickness results for both WT and TASTPM mice computed from manual segmentation. When comparing males to females, we found no significant differences in the measures detected and the data reported are the average of the entire group.

Total intracranial and whole brain volumes increased in both groups but were greater in TASTPM. Because the regional volumes did not linearly change with the whole brain, to avoid over-evaluations of the differences we did not normalize the regional volumes by the respective TIV considering the volumes in absolute terms. Cortical and subcortical volumes decreased progressively with age in TASTPM while were altered a little in WT (Table 3 and Fig. 7). Caudate-putamen and frontal cortex were similar at 4 months, but at 9 months were significantly smaller in TASTPM than in WT; indeed, transgenexage interactions were strongly significant for both regions ( $p < 0.001$  and  $0.01$ , respectively). Same trend but opposite direction for the ventricles (interaction  $p < 0.001$ ). In TASTPM, the olfactory bulb started to decrease later than 13 months and continued until 22 (interaction  $p$  value  $< 0.001$ ). The hippocampus and the rest of the cortex were significantly smaller in TASTPM when compared with WT at all the ages considered. Anyway, a significant transgenexage interaction was detected ( $p < 0.05$  and  $0.001$ , respectively).

The ERC thickness decreased in relation to age only in TASTPM starting at the age of 9 months (interaction  $p < 0.0001$ ).

Volume (mm <sup>3</sup> )	WT (months)					TASTPM (months)				
	3	9	13	18	22	3	9	13	18	22
Cau-Put	26.0 ± 1.4	26.2 ± 1.5	26.0 ± 1.7	25.2 ± 1.4	25.8 ± 0.8	25.0 ± 1.2	22.1 ± 1.1	20.4 ± 0.7	19.0 ± 1.8	17.8 ± 0.7
Hp	18.4 ± 1.2	18.2 ± 0.8	19.1 ± 1.0	19.1 ± 0.9	18.8 ± 1.2	18.4 ± 1.0	17.5 ± 1.0	16.7 ± 1.3	16.8 ± 1.1	15.6 ± 1.4
OB	24.8 ± 1.6	26.9 ± 1.1	27.0 ± 1.5	27.9 ± 1.2	26.8 ± 1.4	24.5 ± 1.2	25.7 ± 1.4	26.0 ± 1.5	25.7 ± 1.5	23.0 ± 1.3
Frontal ctx	23.2 ± 2.0	23.2 ± 1.3	22.8 ± 0.9	23.0 ± 2.1	22.8 ± 1.6	23.1 ± 0.9	21.4 ± 2.0	21.6 ± 1.6	20.5 ± 1.6	20.1 ± 1.5
Ctx	108.5 ± 3.7	109.3 ± 3.5	110.0 ± 2.5	113.1 ± 4.7	108.6 ± 4.6	105.0 ± 3.6	105.3 ± 2.5	104.5 ± 2.2	103.1 ± 2.0	100.2 ± 1.6
Vent	5.1 ± 0.9	4.9 ± 0.8	5.2 ± 0.8	5.0 ± 1.0	5.6 ± 0.8	5.2 ± 0.8	6.0 ± 0.8	7.0 ± 0.9	8.4 ± 1.6	9.5 ± 1.8
WB	499.6 ± 12.1	511.4 ± 13.8	515.6 ± 15.2	521.2 ± 15.2	510.6 ± 22.3	475.9 ± 18.2	505.0 ± 9.5	509.5 ± 18.0	524.5 ± 24.7	479.0 ± 13.0
ICV	540.9 ± 14.1	555.1 ± 25.7	568.1 ± 18.7	584.6 ± 17.3	583.0 ± 26.3	519.8 ± 15.3	558.5 ± 20.9	571.3 ± 28.3	601.7 ± 39.1	589.7 ± 13.8
<b>Thickness (mm)</b>										
ERC	0.75 ± 0.04	0.72 ± 0.04	0.73 ± 0.04	0.75 ± 0.04	0.72 ± 0.05	0.72 ± 0.05	0.67 ± 0.03**	0.63 ± 0.04***	0.60 ± 0.03***	0.59 ± 0.04***

**Table 3. Comparison between TASTPM and WT volume and thickness estimations.** Within-site group means and standard deviation (across mice and hemispheres) of volumes and thickness obtained from the manual segmentation. The ERC statistics refer to two-way ANOVA, \*\* $p < .01$ ; \*\*\* $p < .001$  after Hochberg's correction. Abbreviations: Cau-Put= caudate-putamen, Hp= hippocampus, OB= olfactory bulb, Fron ctx= frontal cortex, ctx= rest of the cortex, Vent= lateral, third and fourth ventricles, WB= whole brain, ICV= intracranial volume, ERC= entorhinal cortex.

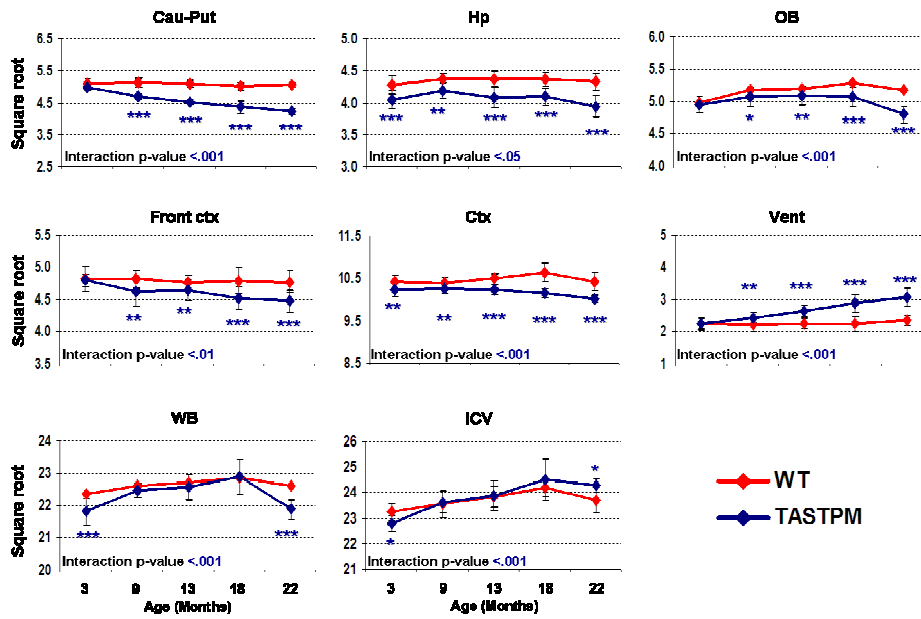


**Fig 7. Comparison between TASTPM and WT normalized volumes across structures.** Within-site group means and standard deviation (across mice and hemispheres) of volumes derived from the manual segmentation. Axis y reported square root values. Two-way ANOVA, \* $p < .05$ ; \*\* $p < .01$ ; \*\*\* $p < .001$  after Hochberg's correction. Interaction p-values were also shown. The abbreviations were the same of Table 3.

### 3.6.1.2 Diffusion results

Typical T2-weighted images, FA maps and colour coded FA of TASTPM and WT brains are shown in Fig 8.

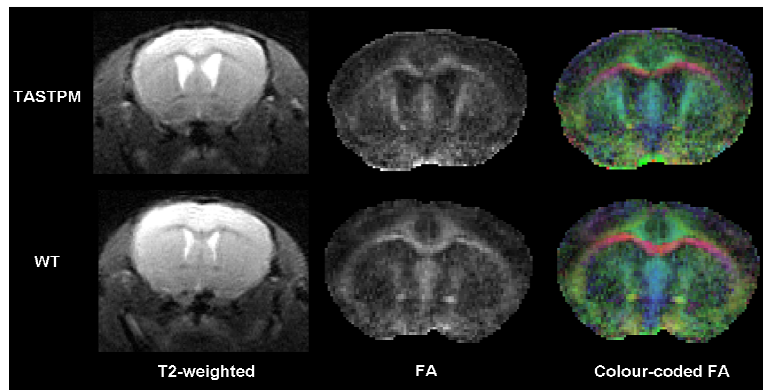


**Fig 8. Representative T2-weighted images, FA maps and colour-coded FA from one coronal slice of young TASTPM and age-matched control.**

The TBSS comparison between TASTPM and WT was done only considering mice of 3, 13 and 22 months old. This analysis revealed changes in DTI parameters of several regions of transgenic mice. FA was significantly lower ( $p < 0.05$ ) in corpus callosum, external capsule, fimbria, cerebral peduncle and internal capsule of older TASTPM when compared to their age-matched controls (Fig 9, top). Viceversa, radial diffusivity was higher in external capsule, corpus callosum and fimbria of older Tg mice than in age-matched WT (Fig 9, bottom).

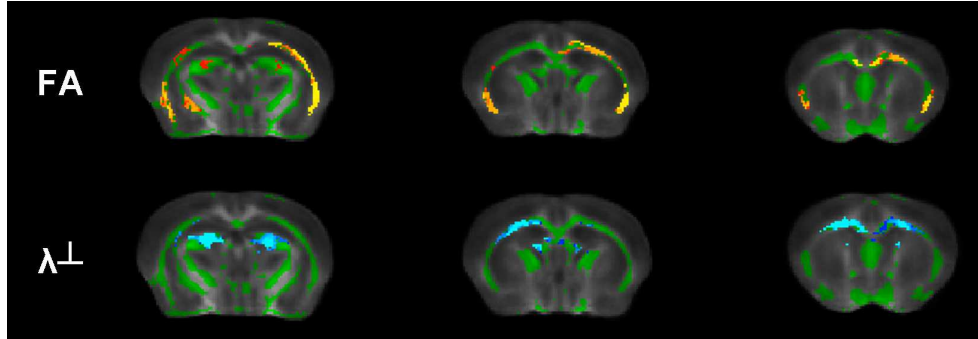


**Fig 9. Automated FA and  $\lambda^\perp$  maps comparisons between older TASTPM and age-matched controls.** Coronal brain images overlaid with the skeleton (green) and with the TBSS results. Data showed significantly ( $p < .05$ ) lower (red-yellow) FA and higher (light-blue)  $\lambda^\perp$  values in external capsule, corpus callosum, fimbria and cerebral peduncle of TASTPM.

Hand-drawn approach was used to perform quantitative analysis of DTI indices in several white (Table 4 a and b) and grey matter regions (Table 4c). In general, DTI parameters changed progressively with age only in several structures of TASTPM while remained stable or was altered a little in WT (Table 4). A significant age-dependent FA, reduction starting at 13 months, was seen in the corpus callosum and anterior commissure (Fig. 10) (transgenexage  $p < 0.0001$  for both) of TASTPM. A concomitant reduction of axial diffusivity (interaction  $p < 0.0001$  for both) and an increment of radial diffusivity (ac interaction  $p < 0.0001$  and cc,  $p = 0.0002$ ) was also seen (Fig. 10). FA decline in cerebral peduncle and cingulum started when TASTPM were 18 months old (cp interaction  $p < 0.0001$  and cing,  $p = 0.001$ ) and in external capsule and fimbria when were 22 (ec interaction  $p = 0.0025$  and fi  $p = 0.0007$ ). In the caudate-putamen, thalamus and olfactory bulb we detected an increase in MD at 22 months (interaction  $p = 0.0034$ ,  $0.0069$  and  $0.034$ , respectively).

a

DTI indices	3 months		9 months		13 months		18 months		22 months		transgenexage	
	FA	MD	FA	MD	FA	MD	FA	MD	FA	MD	FA	MD
<b>sc</b>												
WT	0,623 ± 0.032	0,734 ± 0.033	0,630 ± 0.033	0,725 ± 0.047	0,64 ± 0.038	0,684 ± 0.043	0,659 ± 0.034	0,706 ± 0.036	0,654 ± 0.034	0,680 ± 0.047		
TASTPM	0,622 ± 0.031	0,755 ± 0.046	0,608 ± 0.023	0,736 ± 0.036	0,573 ± 0.043***	0,729 ± 0.044	0,535 ± 0.027***	0,727 ± 0.037	0,489 ± 0.041***	0,686 ± 0.050	<0.0001	ns
<b>cc</b>												
WT	0,626 ± 0.048	0,607 ± 0.053	0,636 ± 0.039	0,763 ± 0.033	0,639 ± 0.038	0,769 ± 0.032	0,643 ± 0.052	0,761 ± 0.037	0,629 ± 0.032	0,727 ± 0.028		
TASTPM	0,612 ± 0.042	0,617 ± 0.041	0,622 ± 0.031	0,795 ± 0.036	0,577 ± 0.058***	0,809 ± 0.052**	0,550 ± 0.042***	0,832 ± 0.055***	0,526 ± 0.034***	0,718 ± 0.019	<0.0001	0.0005
<b>cp</b>												
WT	0,772 ± 0.016	0,75 ± 0.031	0,783 ± 0.022	0,737 ± 0.030	0,786 ± 0.026	0,732 ± 0.029	0,781 ± 0.022	0,723 ± 0.033	0,777 ± 0.027	0,713 ± 0.034		
TASTPM	0,791 ± 0.030	0,774 ± 0.028	0,773 ± 0.034	0,731 ± 0.035	0,765 ± 0.035	0,742 ± 0.052	0,740 ± 0.042***	0,743 ± 0.028	0,720 ± 0.026***	0,697 ± 0.033	<0.0001	ns
<b>clng</b>												
WT	0,507 ± 0.025	0,715 ± 0.023	0,549 ± 0.027	0,668 ± 0.030	0,542 ± 0.031	0,665 ± 0.047	0,541 ± 0.022	0,675 ± 0.036	0,550 ± 0.036	0,662 ± 0.029		
TASTPM	0,52 ± 0.018	0,728 ± 0.024	0,511 ± 0.032*	0,719 ± 0.034**	0,524 ± 0.051	0,700 ± 0.047	0,494 ± 0.023**	0,695 ± 0.030	0,481 ± 0.031***	0,659 ± 0.029	0.0010	ns
<b>Int</b>												
WT	0,463 ± 0.035	0,713 ± 0.016	0,524 ± 0.038	0,691 ± 0.024	0,499 ± 0.020	0,697 ± 0.021	0,517 ± 0.039	0,691 ± 0.024	0,520 ± 0.040	0,674 ± 0.022		
TASTPM	0,519 ± 0.020**	0,738 ± 0.027	0,508 ± 0.038	0,709 ± 0.023	0,541 ± 0.054	0,713 ± 0.030	0,532 ± 0.037	0,705 ± 0.034	0,484 ± 0.042*	0,670 ± 0.025	0.0007	ns
<b>sc</b>												
WT	0,522 ± 0.033	0,741 ± 0.017	0,537 ± 0.039	0,732 ± 0.029	0,533 ± 0.047	0,722 ± 0.033	0,542 ± 0.060	0,722 ± 0.047	0,542 ± 0.040	0,695 ± 0.026		
TASTPM	0,494 ± 0.032	0,759 ± 0.043	0,524 ± 0.069	0,740 ± 0.029	0,528 ± 0.081	0,742 ± 0.043	0,510 ± 0.107	0,743 ± 0.034	0,441 ± 0.032***	0,733 ± 0.046*	0.0025	ns
<b>fl</b>												
WT	0,594 ± 0.061	0,895 ± 0.047	0,645 ± 0.050	0,892 ± 0.069	0,670 ± 0.027	0,909 ± 0.083	0,680 ± 0.019	0,860 ± 0.069	0,653 ± 0.030	0,845 ± 0.059		
TASTPM	0,680 ± 0.034***	0,889 ± 0.066	0,684 ± 0.028	0,869 ± 0.046	0,670 ± 0.029	0,850 ± 0.096	0,651 ± 0.083	0,866 ± 0.073	0,652 ± 0.033	0,782 ± 0.050	0.0002	ns

b

DTI indices	3 months		9 months		13 months		18 months		22 months		transgenexage	
	$\lambda_{II}$	$\lambda_{\perp}$	$\lambda_{II}$	$\lambda_{\perp}$	$\lambda_{II}$	$\lambda_{\perp}$	$\lambda_{II}$	$\lambda_{\perp}$	$\lambda_{II}$	$\lambda_{\perp}$	$\lambda_{II}$	$\lambda_{\perp}$
<b>ac</b>												
WT	1.338 ± 0.075	0.430 ± 0.027	1.330 ± 0.077	0.423 ± 0.041	1.288 ± 0.064	0.397 ± 0.043	1.323 ± 0.073	0.397 ± 0.036	1.273 ± 0.074	0.384 ± 0.043		
TASTPM	1.378 ± 0.078	0.444 ± 0.041	1.323 ± 0.060	0.442 ± 0.028	1.259 ± 0.082	0.465 ± 0.041***	1.220 ± 0.074***	0.480 ± 0.033***	1.092 ± 0.073***	0.483 ± 0.048***	<0.0001	<0.0001
<b>cc</b>												
WT	1.484 ± 0.078	0.478 ± 0.070	1.401 ± 0.072	0.445 ± 0.043	1.413 ± 0.049	0.448 ± 0.043	1.391 ± 0.087	0.438 ± 0.059	1.323 ± 0.072	0.430 ± 0.027		
TASTPM	1.46 ± 0.134	0.496 ± 0.033	1.443 ± 0.046	0.471 ± 0.043	1.381 ± 0.091	0.624 ± 0.069***	1.388 ± 0.069	0.667 ± 0.063***	1.174 ± 0.043***	0.604 ± 0.052***	<0.0001	0.0002
<b>cp</b>												
WT	1.618 ± 0.070	0.318 ± 0.021	1.608 ± 0.087	0.304 ± 0.022	1.601 ± 0.088	0.303 ± 0.024	1.569 ± 0.089	0.307 ± 0.024	1.535 ± 0.083	0.306 ± 0.026		
TASTPM	1.710 ± 0.082	0.308 ± 0.035	1.575 ± 0.119	0.315 ± 0.030	1.585 ± 0.127	0.330 ± 0.038*	1.538 ± 0.073	0.349 ± 0.042***	1.41 ± 0.063**	0.342 ± 0.031**	0.0002	0.0016
<b>clng</b>												
WT	1.154 ± 0.040	0.495 ± 0.024	1.119 ± 0.067	0.447 ± 0.020	1.101 ± 0.058	0.447 ± 0.045	1.123 ± 0.048	0.451 ± 0.033	1.110 ± 0.055	0.448 ± 0.036		
TASTPM	1.191 ± 0.042	0.497 ± 0.021	1.164 ± 0.064	0.496 ± 0.034**	1.143 ± 0.083	0.478 ± 0.046	1.101 ± 0.072	0.491 ± 0.013*	1.035 ± 0.048*	0.471 ± 0.027	0.0052	ns
<b>Int</b>												
WT	1.112 ± 0.051	0.614 ± 0.023	1.144 ± 0.036	0.464 ± 0.035	1.127 ± 0.049	0.483 ± 0.015	1.136 ± 0.048	0.489 ± 0.033	1.111 ± 0.056	0.465 ± 0.027		
TASTPM	1.212 ± 0.060***	0.601 ± 0.019	1.152 ± 0.032	0.488 ± 0.036	1.196 ± 0.061**	0.472 ± 0.041	1.171 ± 0.025	0.472 ± 0.043	1.065 ± 0.039	0.473 ± 0.034*	<0.0001	ns
<b>sc</b>												
WT	1.198 ± 0.049	0.513 ± 0.025	1.198 ± 0.063	0.499 ± 0.036	1.178 ± 0.054	0.496 ± 0.042	1.192 ± 0.088	0.489 ± 0.047	1.142 ± 0.051	0.471 ± 0.033		
TASTPM	1.189 ± 0.058	0.544 ± 0.044	1.202 ± 0.073	0.503 ± 0.056	1.210 ± 0.076	0.508 ± 0.074	1.198 ± 0.084	0.516 ± 0.086	1.109 ± 0.074	0.545 ± 0.038***	ns	0.0261
<b>fi</b>												
WT	1.586 ± 0.080	0.549 ± 0.073	1.663 ± 0.169	0.506 ± 0.052	1.736 ± 0.135	0.496 ± 0.065	1.657 ± 0.118	0.461 ± 0.048	1.589 ± 0.105	0.474 ± 0.048		
TASTPM	1.721 ± 0.105	0.473 ± 0.059	1.690 ± 0.086	0.458 ± 0.041	1.619 ± 0.182	0.465 ± 0.064	1.612 ± 0.082	0.493 ± 0.090	1.460 ± 0.074	0.445 ± 0.044	0.0035	0.0016

C

DTI indices	3 months		9 months		13 months		18 months		22 months		transgenexage	
	FA	MD	FA	MD	FA	MD	FA	MD	FA	MD	FA	MD
<b>Cau-Put</b>												
WT	0,187 ± 0,019	0,685 ± 0,013	0,186 ± 0,010	0,699 ± 0,022	0,186 ± 0,020	0,702 ± 0,045	0,195 ± 0,014	0,705 ± 0,016	0,204 ± 0,021	0,706 ± 0,013		
TASTPM	0,209 ± 0,018*	0,717 ± 0,025*	0,206 ± 0,015	0,709 ± 0,025	0,205 ± 0,016	0,717 ± 0,037	0,213 ± 0,019	0,715 ± 0,023	0,199 ± 0,023	0,673 ± 0,023*	0.0034	ns
<b>Hp</b>												
WT	0,171 ± 0,013	0,738 ± 0,018	0,186 ± 0,021	0,748 ± 0,027	0,183 ± 0,015	0,748 ± 0,022	0,181 ± 0,016	0,752 ± 0,025	0,188 ± 0,022	0,762 ± 0,022		
TASTPM	0,182 ± 0,031	0,77 ± 0,038**	0,176 ± 0,012	0,76 ± 0,021	0,187 ± 0,017	0,784 ± 0,050***	0,190 ± 0,019	0,786 ± 0,032**	0,176 ± 0,010	0,783 ± 0,041	ns	ns
<b>OB</b>												
WT	0,245 ± 0,014	0,707 ± 0,023	0,256 ± 0,008	0,697 ± 0,034	0,258 ± 0,014	0,696 ± 0,020	0,260 ± 0,029	0,730 ± 0,039	0,238 ± 0,020	0,718 ± 0,041		
TASTPM	0,248 ± 0,016	0,721 ± 0,034	0,254 ± 0,012	0,69 ± 0,015	0,248 ± 0,018	0,728 ± 0,033	0,247 ± 0,020	0,749 ± 0,045	0,22 ± 0,014*	0,681 ± 0,029**	ns	0.0034
<b>Thal</b>												
WT	0,214 ± 0,030	0,728 ± 0,014	0,219 ± 0,035	0,732 ± 0,027	0,201 ± 0,025	0,738 ± 0,024	0,192 ± 0,022	0,737 ± 0,027	0,192 ± 0,031	0,728 ± 0,035		
TASTPM	0,193 ± 0,057	0,73 ± 0,032*	0,171 ± 0,018*	0,73 ± 0,029	0,211 ± 0,031	0,780 ± 0,042	0,238 ± 0,038*	0,723 ± 0,064	0,229 ± 0,055	0,682 ± 0,048	0.0003	0.0069

**Table 4. DTI indices of the white (a, b) and grey (c) regions of interest.** MD,  $\lambda_{||}$  and  $\lambda_{\perp}$  are expressed as  $10^{-3} \text{ mm}^2/\text{s}$ . Two-way ANOVA, \* $p < .05$ ; \*\* $p < .01$ ; \*\*\* $p < .001$  after Hochberg's correction. Interaction p-values are shown in the transgene x age column. Abbreviations: FA= fractional anisotropy, MD= mean diffusivity,  $\lambda_{||}$ = axial diffusivity,  $\lambda_{\perp}$ = radial diffusivity, cc= corpus callosum, ac= anterior commissure, cp= cerebral peduncle, cing= cingulum, int= internal capsule, ec= external capsule, fi= fimbria, Cau-Put= caudate-putamen, Hp= hippocampus, OB= olfactory bulb, Thal= thalamus, ns= non-significant.

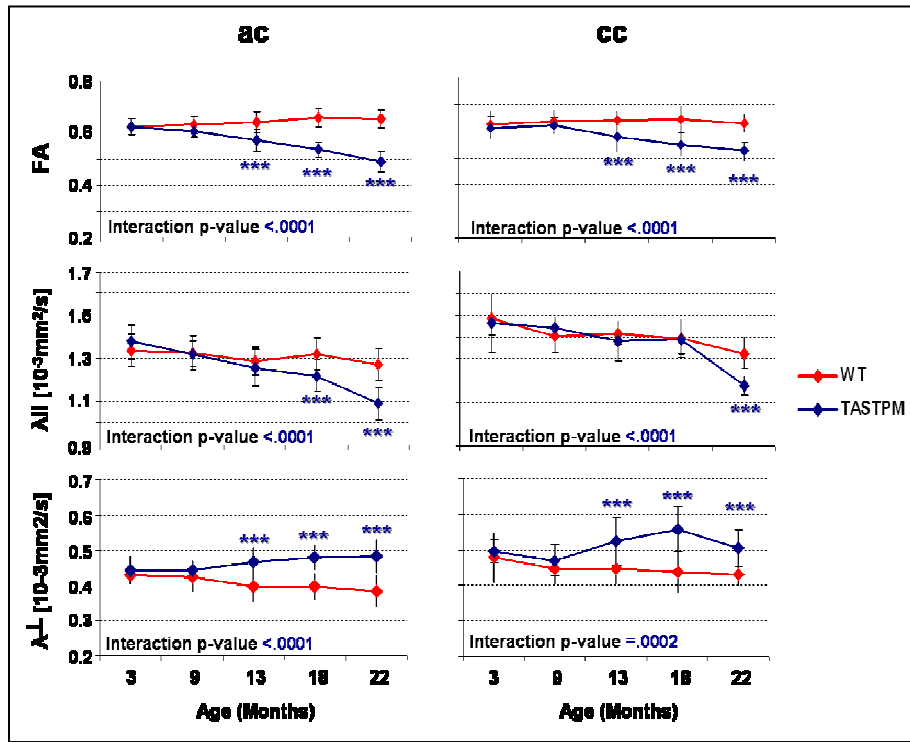


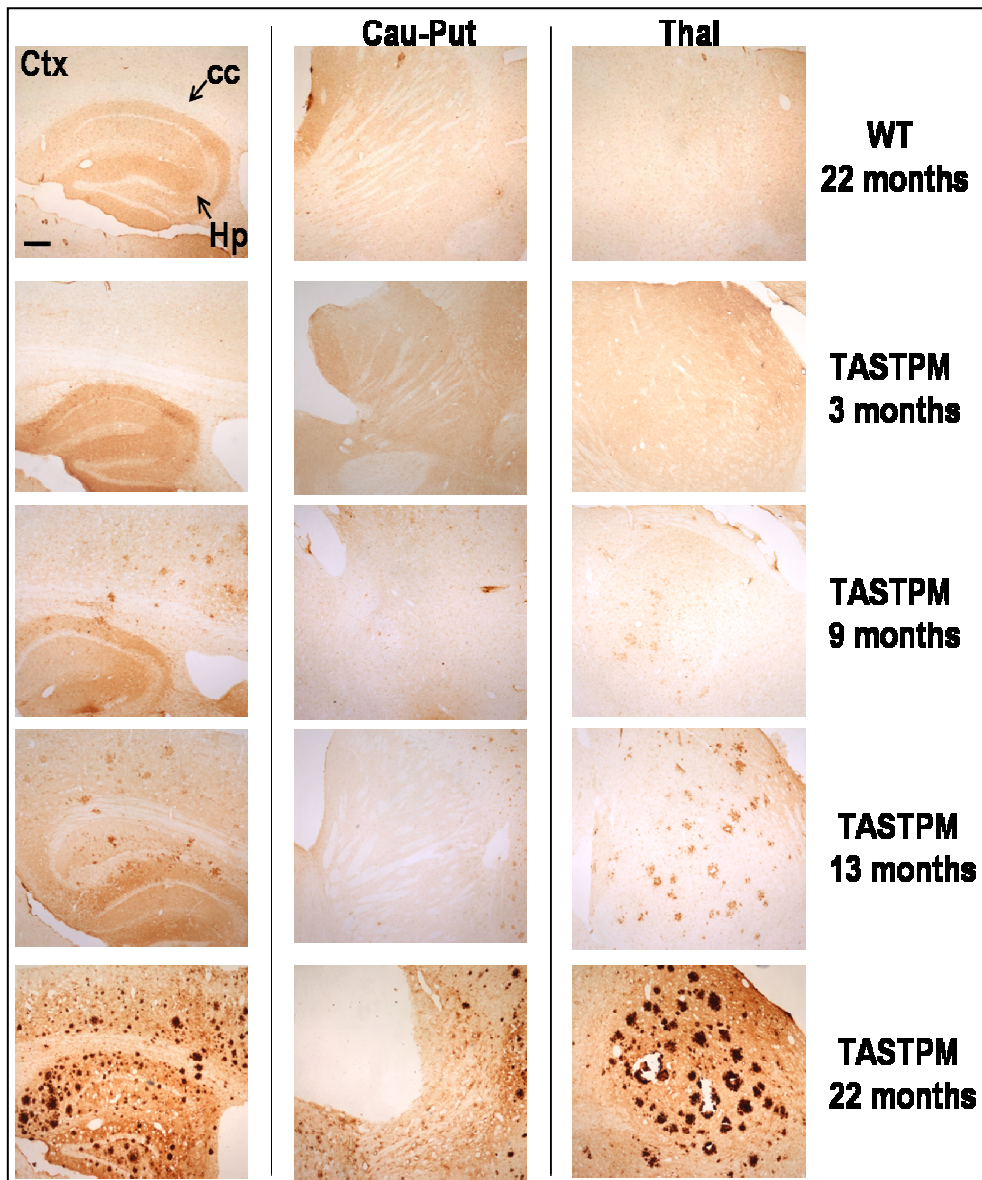
**Fig 10. DTI indices in the anterior commissure (ac) and corpus callosum (cc) of TASTPM and age-matched WT. Two-way ANOVA, \* $p < .05$ ; \*\* $p < .01$ ; \*\*\* $p < .001$  after Hochberg's correction. Interaction p-values are also shown.**

### 3.6.1.3 Histology

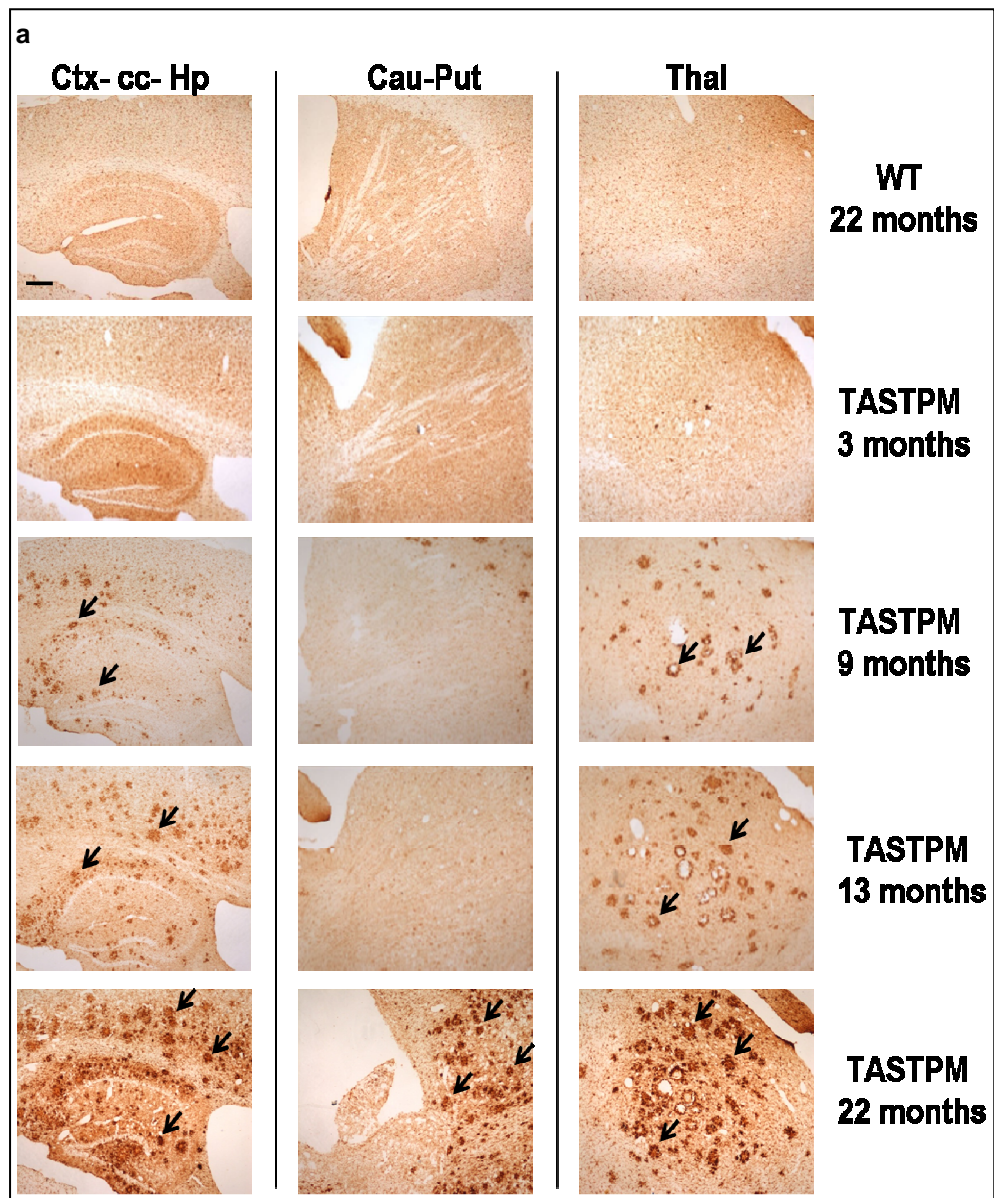
At least five mice from all ages were stained for A $\beta$  deposits, myelinated axons, microglia and astrocytes activation.

As expected, the 3 months old TASTPM tissues did not show the A $\beta$  deposits. However, around 9 months of age, TASTPM began to exhibit A $\beta$  pathology in cortex, corpus callosum, hippocampus and thalamus. Plaques increased with age in number and size (Fig. 11) and covered all brain in the older transgenic. The majority of the plaques was surrounded by activated glia and GFAP-positive astrocytes (Fig. 12 a and b, respectively), clear signs of neuroinflammation. Finally, fibers and white matter organization were reduced in corpus callosum and striatum of TASTPM, from 13 months (Fig. 13).





**Fig 11. A representative comparison of amyloid load among older WT and different ages of TASTPM.** Sagittal slices were immunostained with the 6E10 antibody. TASTPM Tg mice display A $\beta$  deposits which became visible at 9 months and increased with age. Even if the majority of the amyloid burdens was in the grey matter, deposits in white matter were clearly evident (magnification 4x; scale bar, 250  $\mu$ m). Abbreviations: Cau-Put= caudate-putamen, Hp= hippocampus, ctx= cortex, cc= corpus callosum, Thal= thalamus.



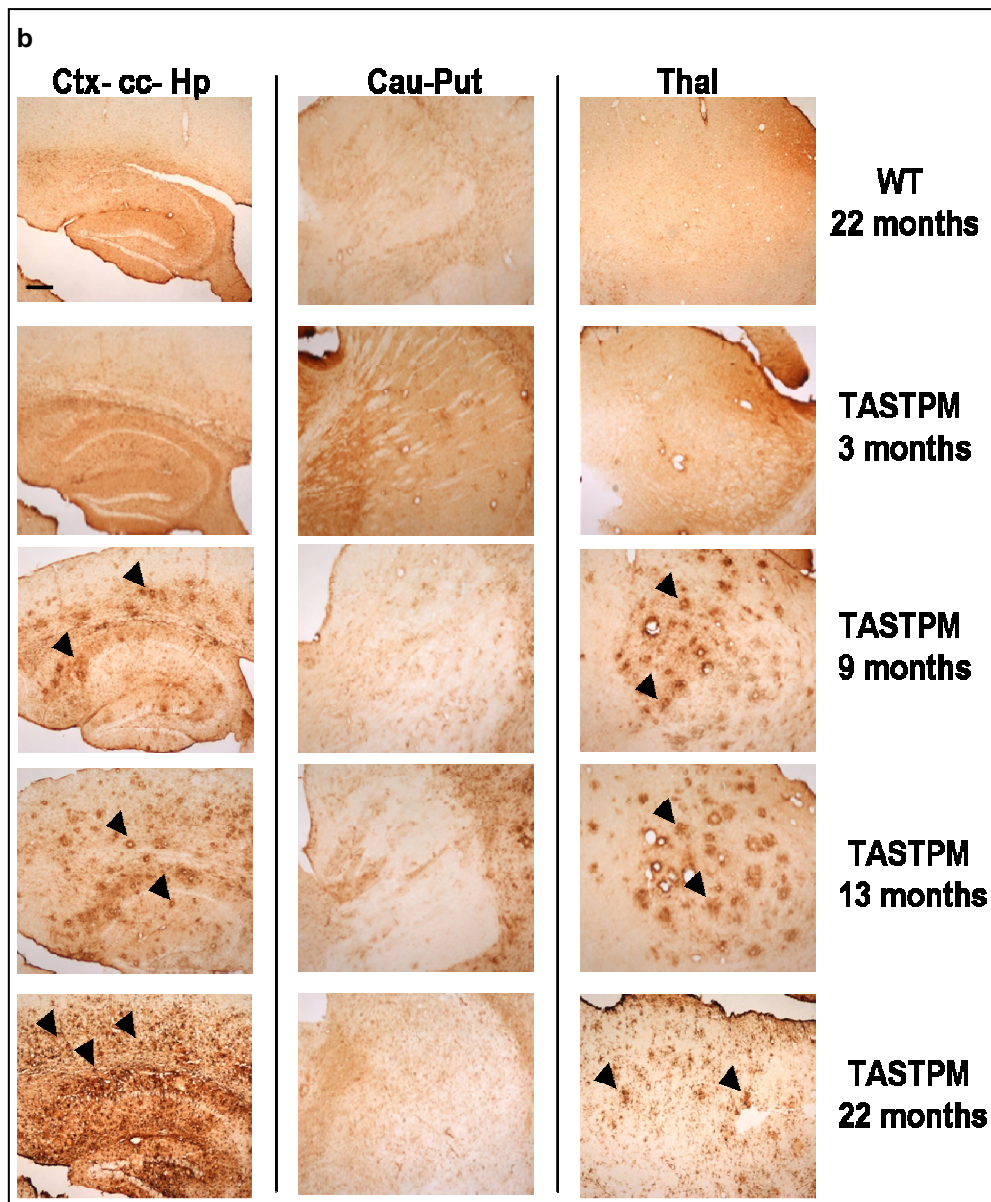


**Fig 12. A representative comparison of neuroinflammation among older WT and different ages of TASTPM.** Sagittal slices were immunostained with Cd11b (a) and GFAP (b) antibodies. Microglial (arrow) and astrocytes (arrowhead) activation were observed when amyloid was present (magnification 4x; scale bar, 250  $\mu$ m). The abbreviations are the same of Fig 11.



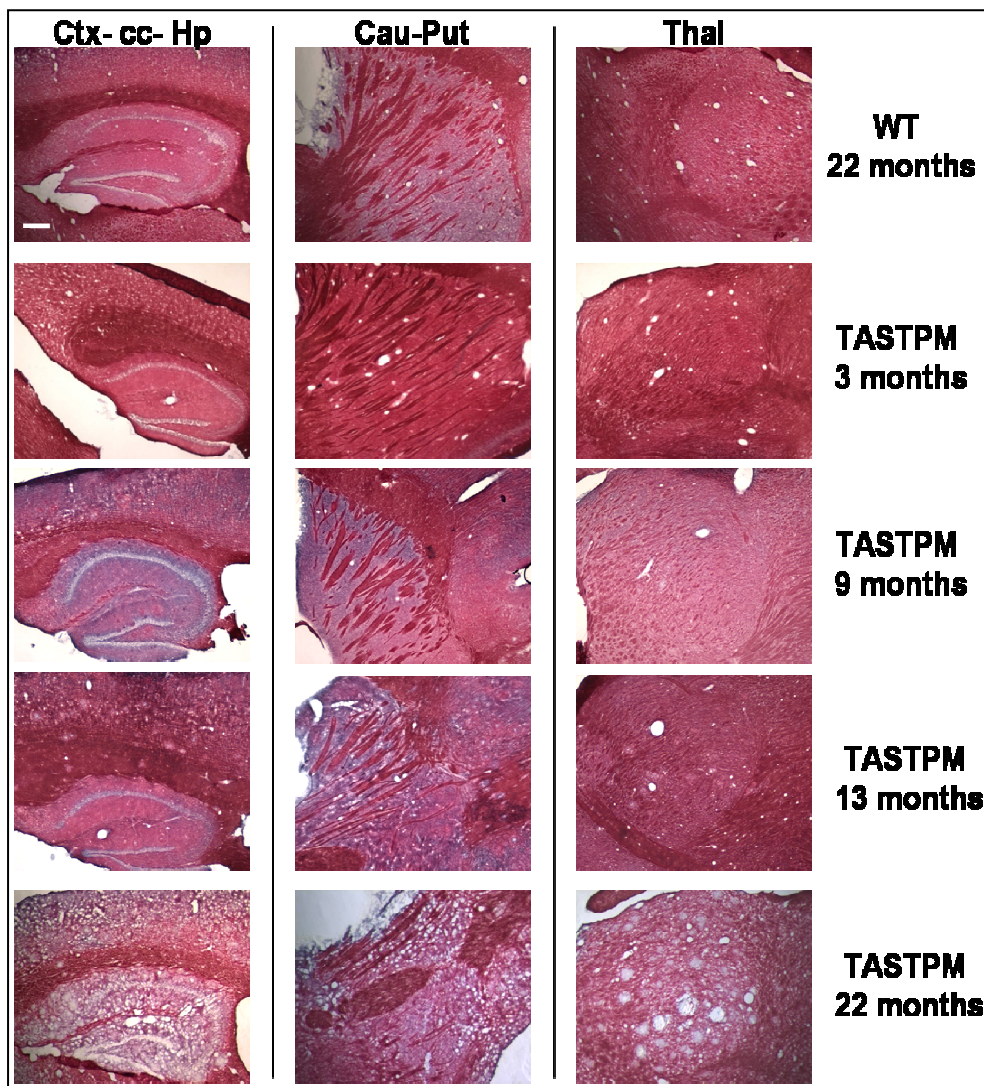


**Fig 13. A representative comparison of myelinated axons among older WT and different ages of TASTPM.** Sagittal slices were stained with Gold chloride. A progressive white matter disorganization starting at 13 months is observable in TASTPM Tg mice (magnification 4x; scale bar, 250  $\mu$ m). The abbreviations are the same of Fig 11.

### 3.6.2 TAUPS2APP

#### 3.6.2.1 Morphometry results

Table 5 shows the volumes and ERC thickness means for WT and TauPS2APP mice derived from manual segmentation. When comparing males to females, we found no significant differences in the measures detected and the data reported are the average of the entire group.

Total intracranial and whole brain volumes were not affected by the transgene presence and had the same trend in both groups. As for TASTPM we used the absolute volumes and not the normalized data. Cortical and subcortical volumes changed progressively with age in transgenic mice in most of the regions considered while was altered a little only WT (Table 5 and Fig. 14). Caudate-putamen, frontal cortex and the rest of the cortex were similar between WT and TauPS2APP at 4 months but at 9 months were significantly smaller in TauPS2APP; indeed, transgenexage interactions were highly significant for all (Cau-Put  $p$ -value < 0.001, Frontal ctx and ctx interaction  $p$ -value < 0.01). The hippocampus was significantly smaller in TauPS2APP when compared to WT at all the ages considered. Anyway, a significant transgenexage interaction was detected ( $p$  < 0.001).

The entorhinal thickness was smaller in TauPS2APP at 4 months and decreased in relation to age only in TauPS2APP (interaction  $p$  < 0.0001).

Brain Volume (mm <sup>3</sup> )	WT					TauPS2APP				
	3	9	13	18	22	3	9	13	18	22
Cau-Put	26.0±1.4	26.0±0.9	25.5±1.1	25.0±0.8	26.0±1.4	25.2±2.0	21.6±1.4	20.0±0.8	19.4±0.8	18.4±0.8
Hp	21.8±1.5	22.5±0.9	22.9±0.9	23.0±1.0	21.8±1.5	18.1±1.1	18.3±0.9	17.5±0.8	17.0±0.8	15.2±0.9
OB	24.8±1.6	26.4±0.9	26.9±0.8	27.1±0.8	24.8±1.6	24.5±1.3	26.1±1.2	27.6±1.4	27.8±1.0	27.5±1.3
Frontal ctx	22.9±1.2	23.1±1.1	23.5±0.8	23.7±0.8	22.9±1.2	22.5±1.3	21.8±1.6	22.3±0.7	21.8±0.7	20.5±0.8
Ctx	108.5±3.8	108.4±2.3	108.4±2.6	108.2±2.3	108.5±3.8	106.3±4.4	100.9±5.3	100.4±3.4	98.8±3.7	98.4±3.2
Vent	5.1±0.8	5.7±0.6	5.9±0.6	6.2±0.5	6.3±0.5	7.7±1.1	9.0±1.8	9.3±1.2	9.8±1.4	10.6±1.3
WB	489.6±12.1	500.3±12.8	497.7±12.4	499.6±15.1	499.6±12.1	500.9±13.1	507.4±16.3	514.8±17.9	510.7±13.9	504.3±11.7
ICV	540.9±14.2	535.8±13.0	539.8±11.2	544.3±13.9	540.9±14.2	547.6±17.0	549.4±16.0	551.2±19.8	547.3±16.4	537.3±13.9
Thickness (mm)										
ERC	0.75±0.04	0.73±0.04	0.74±0.04	0.73±0.03	0.69±0.02	0.68±0.04***	0.65±0.04***	0.63±0.02***	0.60±0.04***	0.56±0.05***

**Table 5. Comparison between TauPS2APP and WT volume estimations across structures.** Within-site group means and standard deviation (across mice and hemispheres) of volumes and thickness derived from the manual segmentation. The ERC statistics referred to two-way ANOVA, \*\* $p$  < .01; \*\*\* $p$  < .001 after Hochberg's correction. The abbreviations were the same of Table 3.

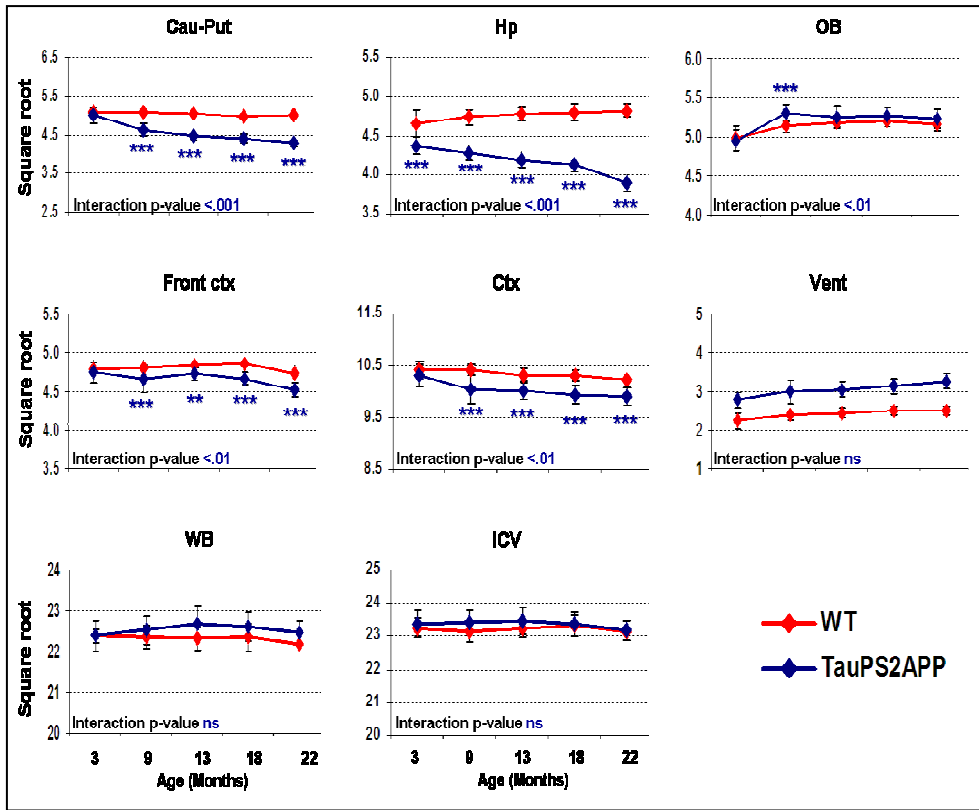


**Fig 14. Comparison between TauPS2APP and WT normalized volume estimations across structures.** Within-site group means and standard deviation (across mice and hemispheres) volumes derived from the manual segmentation. Two-way ANOVA,  $*p < .05$ ;  $**p < .01$ ;  $***p < .001$  after Hochberg's correction. Interaction p-values were also shown. The abbreviations were the same of Table 3.

### 3.6.2.2 Diffusion results

The TBSS comparison between TauPS2APP and WT was done only considering mice of 3, 13 and 22 months old. This analysis did not reveal any significant reduction or increment of FA in transgenic mice when compared to WT (data not shown).

In general, quantitative DTI parameters were significantly different from the age-matched controls only in several grey matters regions (Table 6). In the caudate-putamen of TauPS2APP there was a significant difference in the FA values at 9 and 13 months ( $p < 0.001$ ). The hippocampus of transgenic mice showed higher MD at 18 months ( $p < 0.01$ ) while the thalamus smaller FA at 3 months ( $p < 0.001$ ).

DTI indices	3 months		9 months		13 months		18 months		22 months		transgene age	
	FA	MD	FA	MD	FA	MD	FA	MD	FA	MD	FA	MD
	Cau- Put											
WT	0.179 ± 0.024	0.692 ± 0.013	0.187 ± 0.008	0.693 ± 0.020	0.188 ± 0.021	0.701 ± 0.058	0.195 ± 0.012	0.705 ± 0.013	0.202 ± 0.028	0.681 ± 0.023		
TauPS2 APP	0.177 ± 0.012	0.701 ± 0.025	0.229 ± 0.024***	0.692 ± 0.022	0.217 ± 0.015***	0.697 ± 0.028	0.213 ± 0.014	0.714 ± 0.026	0.210 ± 0.015	0.714 ± 0.026	<0.0001	ns
	Hp											
WT	0.175 ± 0.015	0.733 ± 0.015	0.192 ± 0.009	0.737 ± 0.023	0.185 ± 0.010	0.754 ± 0.022	0.194 ± 0.027	0.747 ± 0.042	0.183 ± 0.008	0.731 ± 0.013		
TauPS2 APP	0.168 ± 0.014	0.752 ± 0.024	0.195 ± 0.015	0.748 ± 0.027	0.187 ± 0.013	0.742 ± 0.027	0.188 ± 0.013	0.776 ± 0.023**	0.189 ± 0.009	0.781 ± 0.025	ns	0.0127
	Thal											
WT	0.234 ± 0.012	0.735 ± 0.015	0.209 ± 0.023	0.735 ± 0.029	0.202 ± 0.025	0.740 ± 0.026	0.193 ± 0.026	0.743 ± 0.032	0.190 ± 0.031	0.716 ± 0.014		
TauPS2 APP	0.163 ± 0.023***	0.717 ± 0.038	0.220 ± 0.033	0.707 ± 0.015	0.182 ± 0.014	0.713 ± 0.025	0.182 ± 0.027	0.739 ± 0.028	0.178 ± 0.025	0.739 ± 0.018	0.0415	ns

**Table 6. DTI indices of the grey regions of interest.** MD is expressed as  $10^3 \text{ mm}^2/\text{s}$ . Two-way ANOVA, \* $p < .05$ ; \*\* $p < .01$ ; \*\*\* $p < .001$  after Hochberg's correction. Interaction  $p$ -values are shown in the transgene  $\times$  age column. Abbreviations: Cau- Put= caudate-putamen, Hp= hippocampus, Thal= thalamus, ns= non-significant.

### 3.6.2.3 Histology

After MRI acquisitions five older TauPS2APP and WT mice were sacrificed and stained for A $\beta$  deposits, myelinated axons, microglia and astrocytes activation. A $\beta$  deposits, although to a lesser extent than in TASTPM, can be seen in cortex, corpus callosum, hippocampus, caudate-putamen and thalamus of older Tg mice (Fig. 15). Also in TauPS2APP plaques were surrounded by activated glia and GFAP-positive astrocytes (Fig. 16 a and b, respectively). Finally, no obvious white matter pathology can be seen in the Tg brain (Fig. 17).

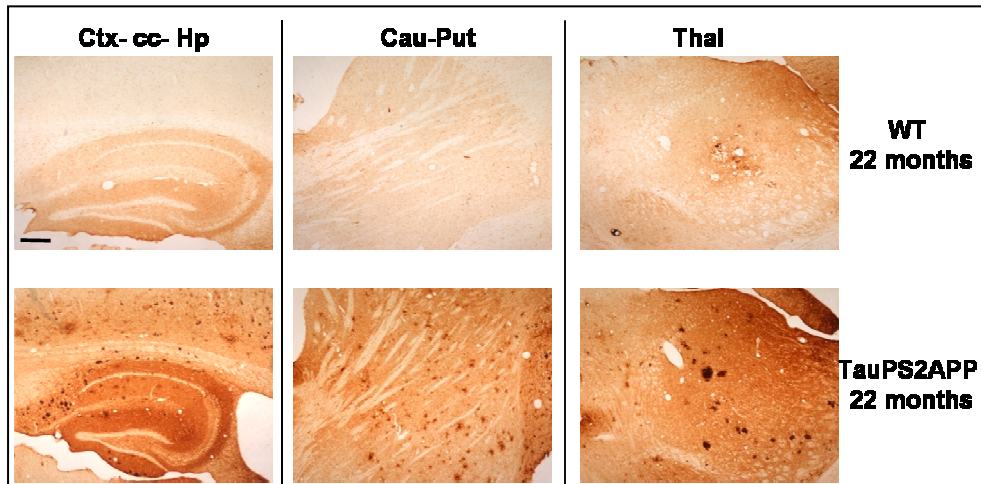


**Fig 15. A representative comparison of amyloid load among older mice.** Sagittal slices were immunostained with the 6E10 antibody. A $\beta$  deposits can be seen in corpus callosum, hippocampus, cortex, caudate-putamen and, to a lesser



extent, in the thalamus (magnification 4x; scale bar, 250  $\mu$ m). The abbreviations are the same of Fig 11.

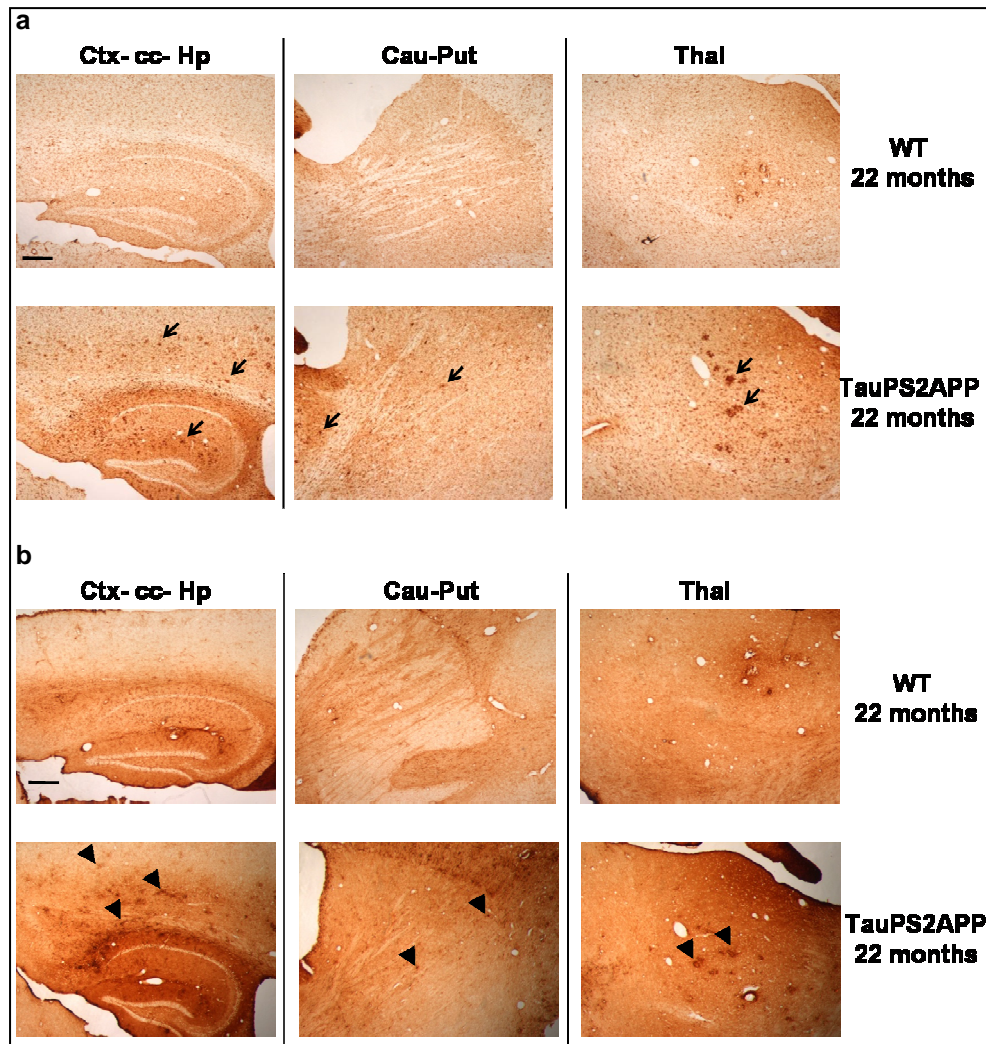


**Fig 16. A representative comparison of neuroinflammation among older mice.** Sagittal slices were immunostained with Cd11b (a) and GFAP (b) antibodies. Only older TauPS2APP exhibited glial (arrow) and astrocytes (arrowhead) activation (magnification 4x; scale bar, 250  $\mu$ m). The abbreviations are the same of Fig 11.



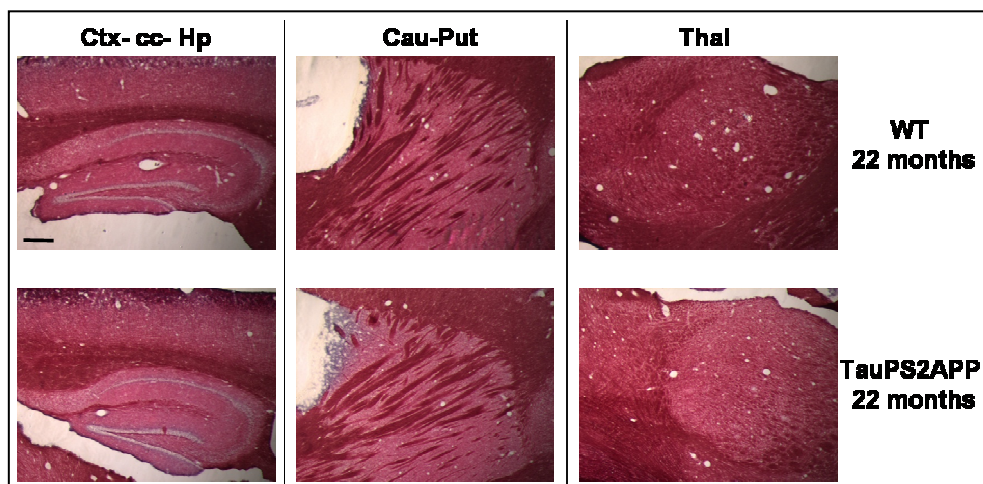


**Fig 17. A representative comparison of myelinated axons among older mice.** Sagittal slices were stained with Gold chloride. Any qualitative difference between TauPS2APP and WT can be appreciated (magnification 4x; scale bar, 250  $\mu$ m). The abbreviations are the same of Fig 11.

### 3.6.3 PDAPP

#### 3.6.3.1 Morphometry results

Table 7 presents the volumes and ERC thickness means for WT and PDAPP mice derived from manual drawn. All mice were males.

Total intracranial and whole brain volumes were not affected by the transgene presence and had the same trend in both. As for TASTPM and TauPS2APP we used the absolute volumes and not the normalized data. Cortical and subcortical volumes changed progressively with age in Tg mice while were altered a little only WT (Table 7 and Fig. 18). Frontal cortex was similar between WT and TauPS2APP at 4 months but at 8 months started to increase in WT; anyway, transgenexage interactions were highly significant ( $p < 0.01$ ). Caudate-Putamen and hippocampus were significantly smaller in PDAPP at 4 months. By the way, significant transgenexage interaction was detected ( $p < 0.01$  and  $p < 0.001$ , respectively). When comparing PDAPP and WT in the remaining structures, we found no significant differences in volumetric values.

The ERC thickness decreased in relation to age only in PDAPP from the age of 13 months (interaction  $p < 0.01$ ).

Brain Volume (mm <sup>3</sup> )	WT (months)					PDAPP (months)				
	3	9	13	18	22	3	9	13	18	22
Cau-Put	24.8 ± 1.0	25.6 ± 1.0	26.2 ± 0.7	24.8 ± 1.4	24.8 ± 0.8	20.8 ± 1.0	22.1 ± 1.6	20.1 ± 1.3	19.8 ± 1.0	18.8 ± 1.0
Hp	21.4 ± 1.0	23.2 ± 1.6	22.5 ± 0.8	22.9 ± 1.2	23.2 ± 0.5	19.7 ± 1.0	20.5 ± 1.4	19.6 ± 1.4	18.7 ± 0.9	17.5 ± 1.2
OB	21.0 ± 1.2	24.8 ± 1.0	25.2 ± 0.8	24.6 ± 1.4	24.6 ± 2.2	20.3 ± 1.3	22.9 ± 1.2	22.5 ± 1.4	23.0 ± 1.0	23.2 ± 1.4
Frontal ctx	22.4 ± 0.8	26.2 ± 0.7	25.6 ± 1.0	24.0 ± 1.2	22.7 ± 2.0	21.8 ± 1.0	22.8 ± 1.5	23.0 ± 1.7	21.7 ± 0.9	21.0 ± 0.7
Ctx	104.1 ± 2.7	105.5 ± 3.1	104.5 ± 3.0	102.4 ± 4.5	99.5 ± 3.3	100.4 ± 1.1	100.1 ± 4.4	96.2 ± 3.9	96.1 ± 2.6	94.1 ± 4.7
Vent	4.8 ± 0.7	4.9 ± 0.7	5.6 ± 0.4	5.8 ± 0.8	6.0 ± 1.0	5.1 ± 0.5	5.9 ± 1.2	6.2 ± 1.0	5.7 ± 0.6	6.4 ± 1.4
WB	453.5 ± 12.0	481.5 ± 17.5	477.3 ± 12.8	490.8 ± 16.7	476.8 ± 18.2	442.7 ± 12.3	471.5 ± 8.1	474.2 ± 10.8	483.0 ± 15.3	474.5 ± 12.2
ICV	482.3 ± 14.9	527.2 ± 17.2	527.3 ± 18.4	535.8 ± 21.3	520.5 ± 18.6	471.9 ± 13.2	514.5 ± 10.5	518.7 ± 12.5	522.0 ± 14.1	512.4 ± 16.2
<b>Thickness (mm)</b>										
ERC	0.68 ± 0.05	0.70 ± 0.04	0.69 ± 0.03	0.70 ± 0.04	0.69 ± 0.01	0.64 ± 0.05	0.67 ± 0.04	0.63 ± 0.03**	0.60 ± 0.03***	0.56 ± 0.04***

**Table 7. Comparison between PDAPP and WT volume estimations across structures.** Within-site group means and standard deviation (across mice and hemispheres) of volumes and thickness derived from the manual segmentation. The ERC statistics refer to two-way ANOVA, \*\*\* $p < .001$  after Hochberg's correction. The abbreviations were the same of Table 3.

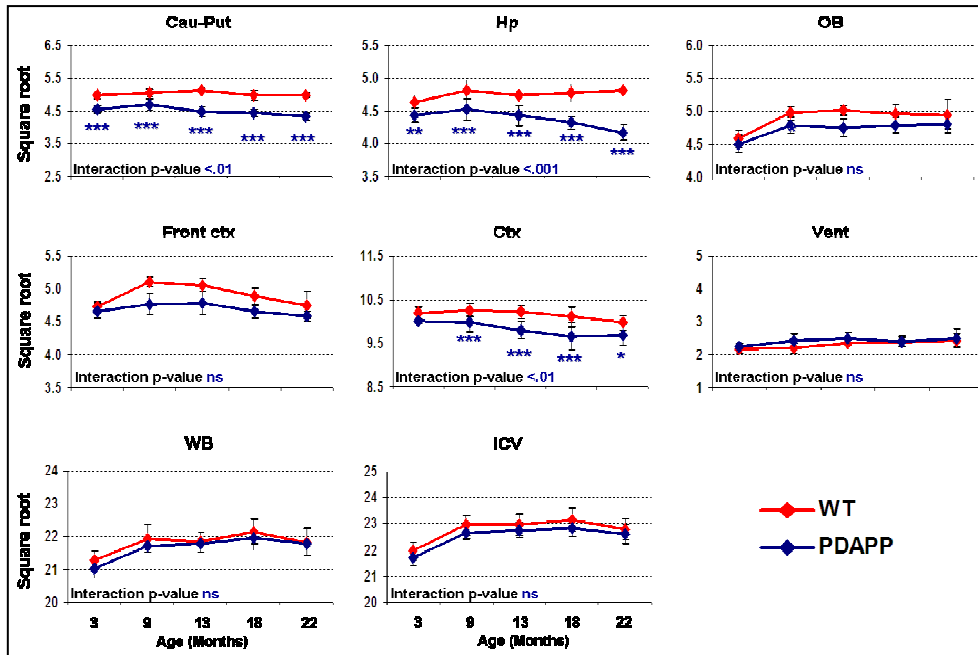


**Fig 18. Comparison between PDAPP and WT normalized volume estimations across structures.** Within-site group means and standard deviation (across mice and hemispheres) of volumes derived from the manual segmentation. Two-way ANOVA, \* $p < .05$ ; \*\* $p < .01$ ; \*\*\* $p < .001$  after Hochberg's correction. Interaction p-values were also shown. The abbreviations were the same of Table 3.

### 3.6.3.2 Diffusion results

The TBSS comparison between PDAPP and WT was done only considering mice of 3, 13 and 22 months old. This analysis did not reveal any significant reduction or increment of FA in transgenic mice when compared to WT (data not shown). In general, quantitative DTI parameters were almost the same among PDAPP and WT for all the ages and the structures considered. Significant differences were detected only in the FA and  $\lambda_{II}$  of corpus callosum and external capsule (Fig.19). The corpus callosum showed smaller values at 4 months (any interaction between age and transgene for FA was detected, for  $\lambda_{II}$   $p < 0.0001$ ), the external capsule began to reach significant differences at 9 for FA (interaction  $p = 0.0002$ ) and 13 months for  $\lambda_{II}$  (interaction  $p = 0.0052$ ). No relevant results in grey matters regions were detected.

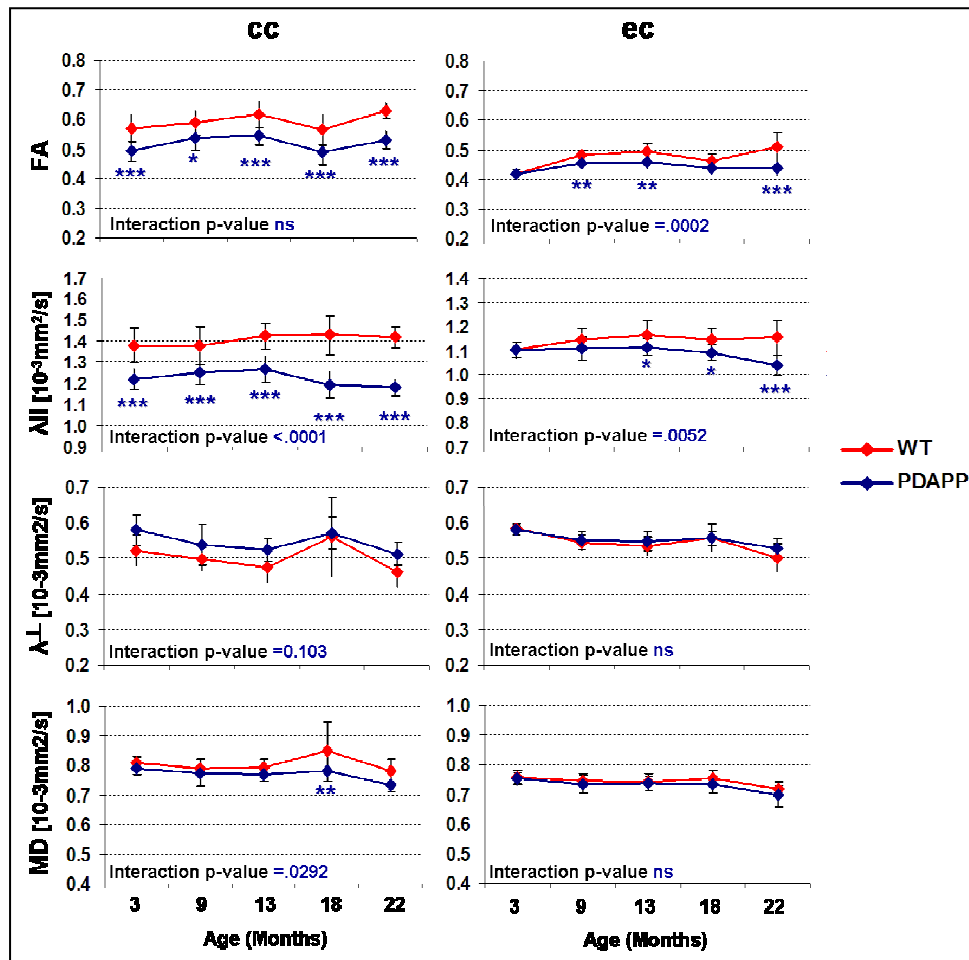
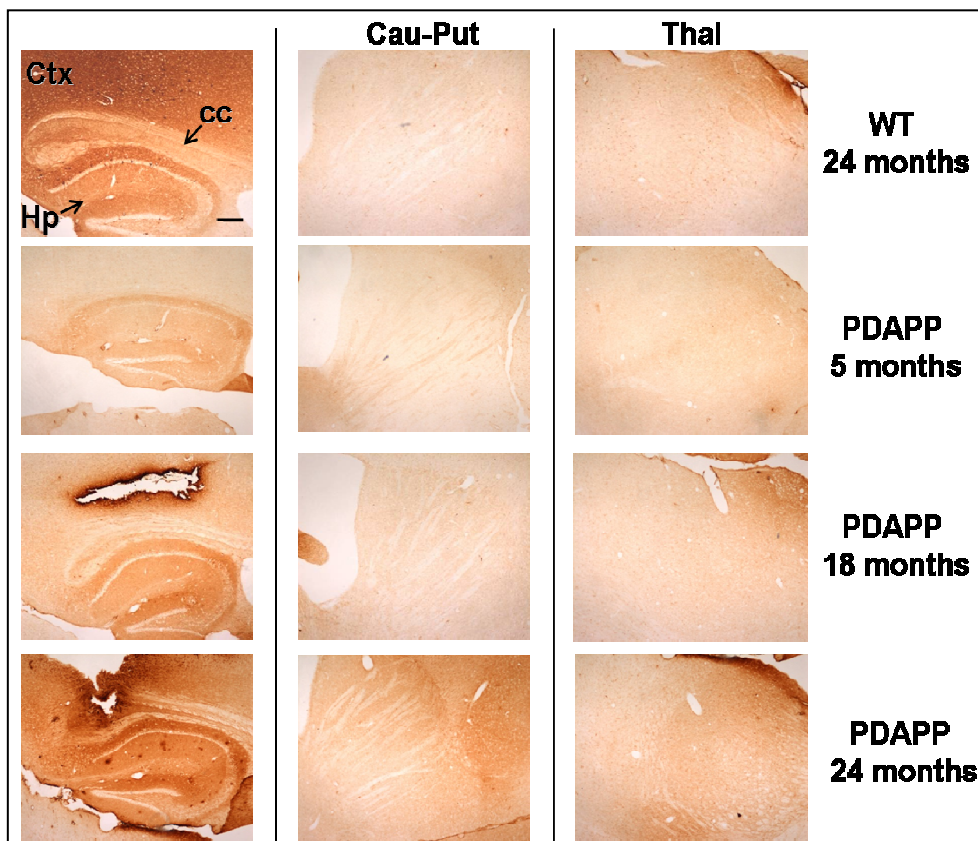


**Fig 19. DTI indices in the corpus callosum (cc) and external capsule (ec) of PDAPP and age-matched WT. Two-way ANOVA, \* $p < .05$ ; \*\* $p < .01$ ; \*\*\* $p < .001$  after Hochberg's correction. Interaction p-values were also shown.**

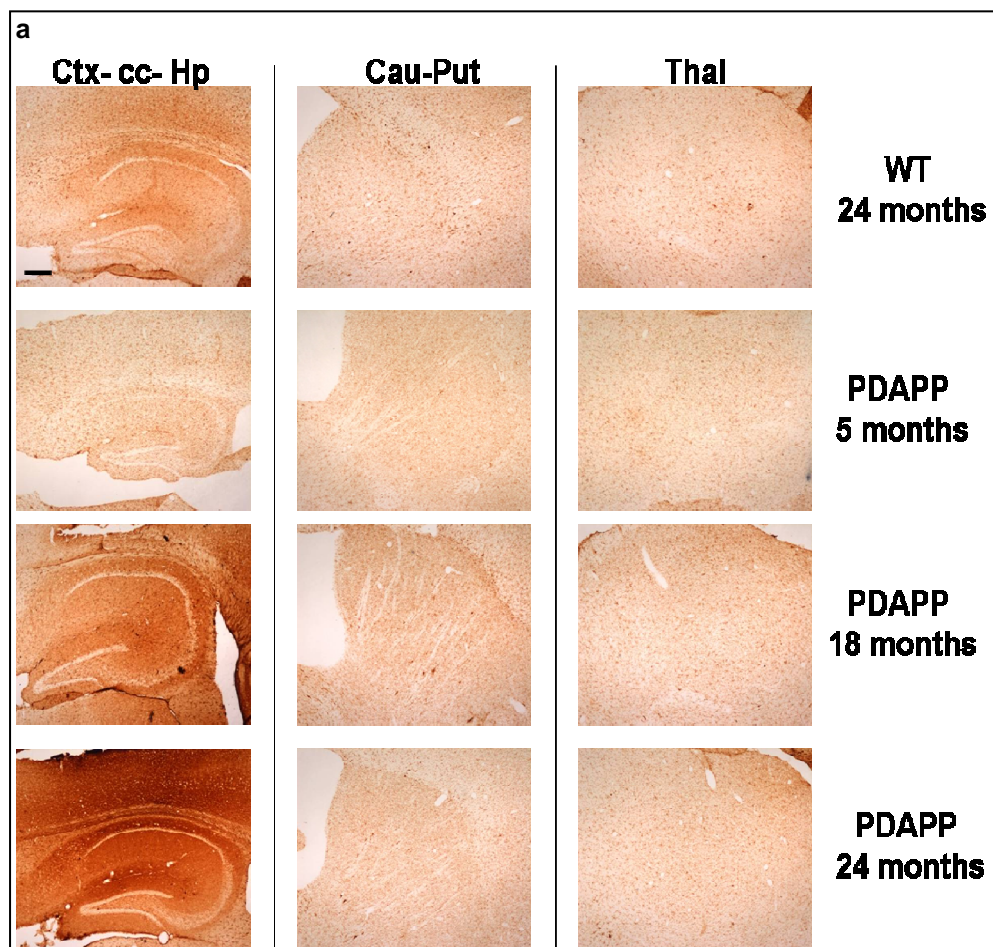
### 3.6.3.3 Histology

At least five mice from all ages were stained for A $\beta$  deposits, myelinated axons, microglia and astrocytes activation.

Few A $\beta$  deposits can be seen only in the hippocampus of older transgenic mice (Fig. 20). Obvious neuroinflammation (Fig. 21) and white matter pathology did not affect transgenic brains (Fig. 22).



**Fig 20. A representative comparison of amyloid load among older WT and different ages of PDAPP.** Sagittal slices were immunostained with the 6E10 antibody. Few A $\beta$  deposits can be seen only in the hippocampus of older PDAPP (magnification 4x; scale bar, 250  $\mu$ m). The abbreviations are the same of Fig 11.





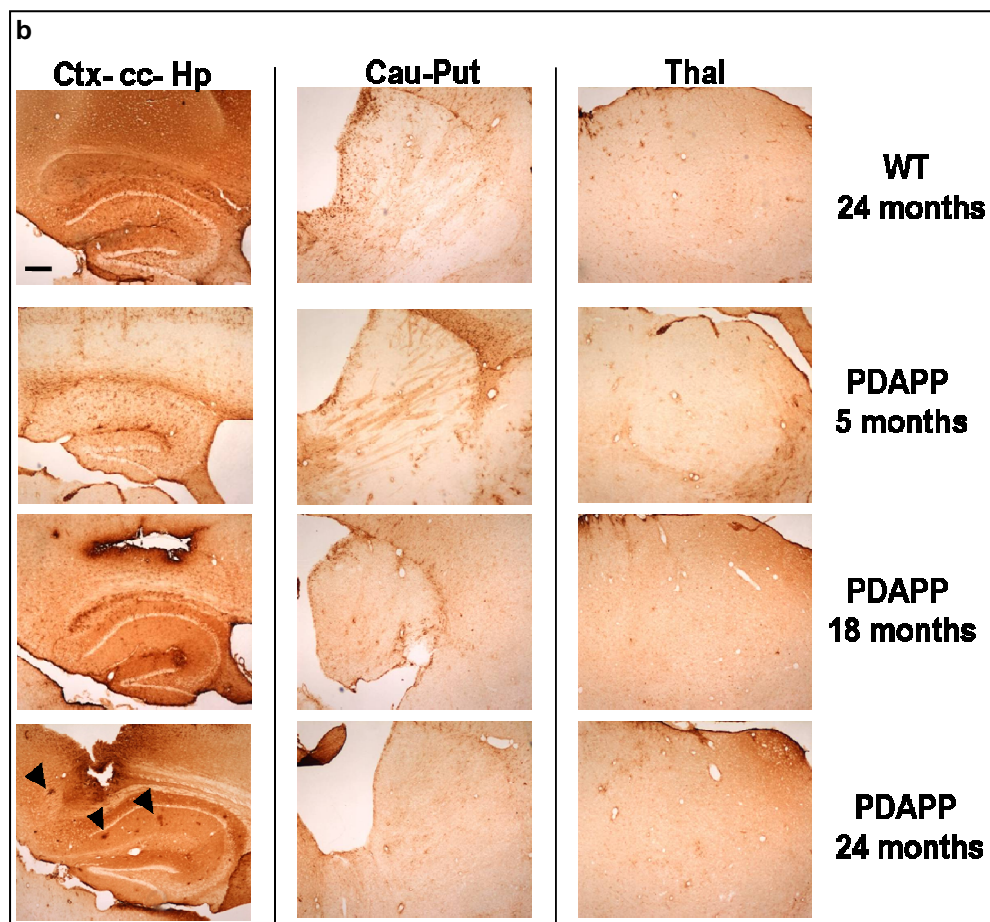


**Fig 21. A representative comparison of neuroinflammation among older WT and different ages of PDAPP.** Sagittal slices were immunostained with Cd11b (a) and GFAP (b) antibodies. No qualitative difference between TauPS2APP and WT can be appreciated (magnification 4x; scale bar, 250  $\mu$ m). The abbreviations are the same of Fig 11.

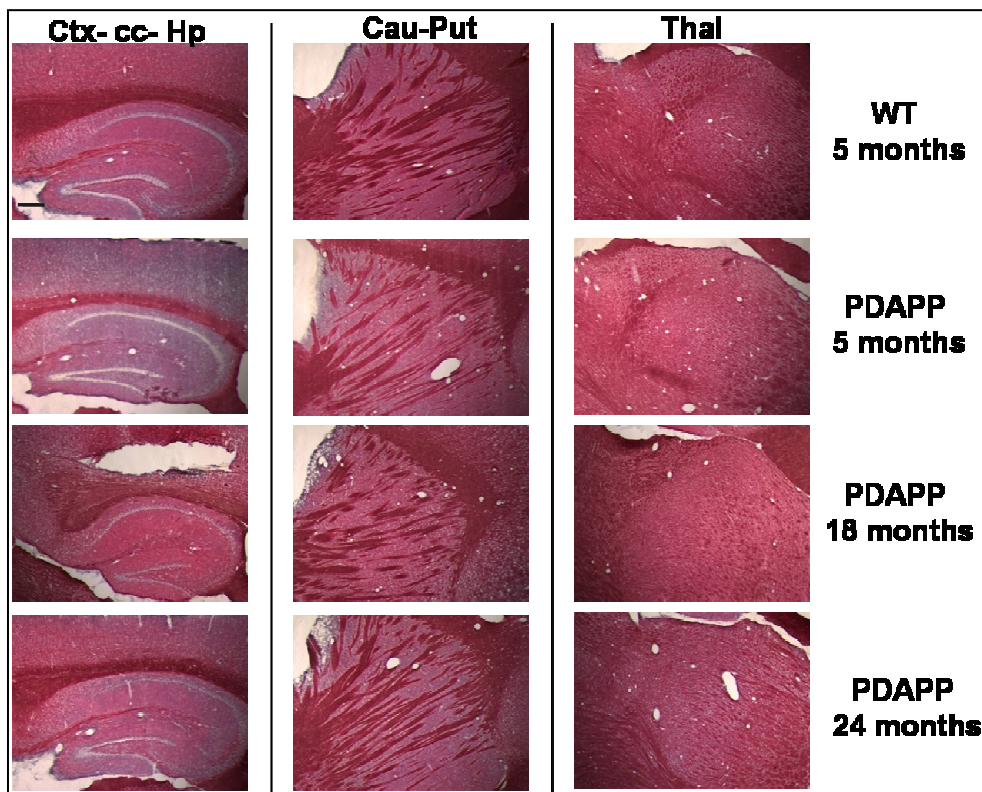


**Fig 22. A representative comparison of myelinated axons among older WT and different ages of PDAPP.** Sagittal slices were stained with Gold chloride. No qualitative difference between PDAPP and WT can be appreciated (magnification 4x; scale bar, 250  $\mu$ m). The abbreviations are the same of Fig 11.



### **3.7 Discussion**

In order to identify imaging markers of disease progression in mice we have characterized three different mouse models of AD. In this work we have analyzed in details structural changes and differences among TASTPM, TauPS2APP, PDAPP and WT using different MRI techniques. The examination was performed through 3D MRI to study brain regions volumes and entorhinal cortex thickness. Microstructural variations in white and grey matter regions were detected using DTI.

At 9 months TASTPM mice shown cerebral plaque pathology consisting in widespread parenchymal deposits (Fig 10). Moreover, deficits in memory tasks were detected at 6 months (REF) indicating an initial decline of brain function at this age. Beside A $\beta$  age-dependen accumulation, TauPS2APP triple transgenic mice are characterized also by neurofibrillary tangles, detectable at a very early age, starting at 4 months [28]. In PDAPP A $\beta$  plaques, dystrophic neuritis and gliosis should appear around 8 months of age (REF) but our findings are in contrast with these results. Indeed we found poor A $\beta$  deposits in absence of gliosis only in older mice.

#### **3.7.1 Brain structural outcome**

##### **3.7.1.1 Genotype effect**

We found a progressive whole brain and TIV volume increases in TASTPM, PDAPP and age-matched control. In TASTPM brain growth was greater than in WT, indeed from 4 to 18 months the percentage of whole brain increment is 4.2 for WT and 9.4 for TASTPM. This could be explained by the strong A $\beta$  load (Fig 9) associated with marked gliosis and astrocitosys (Fig 10a and b) which was present in TASTPM. In PDAPP and WT was equally around 10%. Brain growing is not surprising if we consider that rodent cranium can expand. Similar findings have been reported in another study regarding TASTPM [132] and in other double Tg models [25, 131, 162]. WT local volumes remained stable in time while changes were discovered in Tg mice. Volume reduction was observed in caudate-putamen and hippocampus of TASTPM, TauPS2APP and PDAPP, as in another transgenic models [166] and in human AD patients [124, 167]. Reduced volume was also seen in frontal cortex of TASTPM and TauPS2APP. These data are supported by the previous observations of frontal cortex pathology involvement in other APP/PS1 [25, 162] and in human patients [168, 169]. Reduction in size was also noticed in the olfactory bulb of TASTPM, in line with the olfactory dysfunction affecting AD patients [170]. As entorhinal cortex was smaller in AD patients than in healthy controls [171], as it is in TASTPM, TauPS2APP and PDAPP when compared with WT mice. Similar findings were reported also for rTg4510 [166].

##### **3.7.1.2 Genotype x age effect**

Regarding the interaction between age and transgene we found two distinct pattern of changes across Tg and WT. One pattern shown the same baseline size and volume reduction at the following ages. This is the case of caudate-putamen and frontal cortex of TASTPM and TauPS2APP, olfactory bulb of TASTPM, cortex of TauPS2APP and PDAPP. Same trend but opposite direction for ventricles in TASTPM. The other pattern resulted in lower volumes in transgenic already at 4 months, such as for hippocampus of all strains and for caudate-putamen of

PDAPP. These latter findings supported the hypothesis proposed by Delatour [25] that some volume deficits are ascribable to development rather than pathological factors.

Although the AD pathology is extensively shown in the thalamus, its manual volumetric assessment can not be performed due to the particular anatomy. For DTI study was different because the masks do not have to cover the entire structure but has just to be inside it. This should be overcome with the application of automatic voxel-by-voxel analysis.

### **3.7.2 Brain Diffusion outcome**

#### **3.7.2.1 White matter**

Besides volumetric estimations, we examined the presence of microstructural alterations in white and grey matter of transgenic mice as detected in MCI [134] and AD patients [135]. Significant results have been obtained especially in TASTPM. We used two different approaches, one relies on manual segmentation and the other take advantages of automatic tools. Manual segmentation is more accurate but is time-consuming, operator-dependent and measures only few ROI, while automated analysis considers much more anatomical regions independently of *a priori* hypothesis but its use is challenging because of brain variations. We found a strong agreement between results computed using the two methods in the biggest anatomical structures (cc, cp and ec) but not in the smaller ones (ac). This is probably because our image resolution is not optimal and wide slice could bring partial volumetric effects (presence of different structures in one voxel and possible wrong diffusion parameters evaluation) affecting the steps required for the skeleton creation. Higher resolution is necessary to reduce partial volume effects not only in small structures but also in regions neighboring grey matter or cerebrospinal fluid. Nevertheless, this is a useful method to rapidly and reproducibly apply a voxel wise analysis to screen DTI parameters differences in white matter regions between Tg mice and WT. Moreover it shows potential utility for the evaluation of possible future treatments in mice models of AD or other neurodegenerative pathologies.

Manual segmentation demonstrated FA,  $\lambda_{||}$  reduction and  $\lambda_{\perp}$  increment in the corpus callosum and anterior commissure in 13 months old TASTPM (Tab 4 and Fig 8), when strong amyloid pathology compared. This diffusion parameter modification have been associated with axonal disconnection, volume reduction [172] and myelin degradation of the axonal bundles [173]. Imaging data correspond to histological findings of fiber disorganization (Fig 11). Similar results have been reported for another APP/PS1 model where corpus callosum and anterior commissure volume reduction, loss of axonal neurofilaments and myelin breakdown were extensively demonstrated [174]. Interestingly, these two fiber tracts showed significant alterations in other Tg mice, although at later ages [138, 139] and in AD patients [175, 176]. White matter injury interested also all the other white matter regions considered but they occurred in advanced stage of pathology (Table 4).

#### **3.7.2.2 Grey matter**

Grey matter organization is more heterogeneous than white matter. Indeed grey matter structures such as hippocampus or caudate-putamen contains a larger number of cell bodies and less fibers. Hence, we reported only MD and FA values. Elevated MD values indicating brain tissue alterations in MCI patients were found in the left hippocampus [137] and were associated with a greater hazard of

progression to AD in amnesic MCI [177]. Despite the lower hippocampal volume of TASTPM and TauPS2APP relative to WT we found higher MD values at all ages but, as mentioned above, were probably related to neurodevelopment alterations. Finally, in caudate-putamen and olfactory bulb an MD decrease was detected, in line with hippocampus and cortex results from Tg2576 [138].

### **3.8 Conclusions and future prospects**

#### **3.8.1 Markers selection**

A number of animal models have been developed but none accurately reproduces human AD pathology. Although with some limitations, mouse models have provided valuable insights into different aspects of AD such as the synergistic effect between tau-related pathology and APP dysfunction in sporadic AD. Transgenic mice are also fundamental to test new drugs allowing translatable therapeutic considerations for patients. Considering that many aspects of AD pathophysiology are not clarified, it is difficult to develop a valid animal model and this might explain the unexpected results and failure of the numerous clinical trials carried out so far. In spite of these limitations and of the differences in brain size, disease complexity and progression, it is possible to identify homologous imaging biomarkers in humans and mice, key elements to predict reliable results in drug testing. To date, among the human imaging markers sensitive to disease progression, atrophy detected with MRI are the most validated surrogate outcomes for clinical trials [126]. Indeed, hippocampal atrophy detected by MRI has recently been accepted by the European Medicines Agency (EMA) for use in clinical trials in pre-dementia stage of AD (EMA/CHMP/SAWP/809208/2011). Unfortunately, it does not seem a reliable marker in mice where alterations of hippocampal formation morphometry are often related to neurodevelopmental rather than neurodegenerative events. More complex mouse models, such as inducible models, where the disease starts after the brain is fully mature, may overcome these neurodevelopmental limitations allowing the creation of appropriate models in which in vivo hippocampal atrophy detection can be used as a surrogate biomarker for AD progression. In the meanwhile, we can consider different local volume changes mimicking the human hippocampal rate of atrophy such as caudate-putamen and frontal cortex volumes decrease in TASTPM and TauPS2APP. As recently shown, MRI cortical thickness biomarker can predict the risk to develop the AD pathology in human [178]. Entorhinal cortex thickness seems a potential index of disease progression in all the transgenic mice considered in this study.

The difficulty to define valid DTI outcomes begins from human field and relies on the lack of longitudinal studies, the impossibility to correlate DTI parameters changes to histological sections and the absence of a complete agreement between all the literature reports. In this scenario mouse models become essential given that histological evaluation, hence A $\beta$  and DTI indices variation correlation, is possible. Alterations of corpus callosum and anterior commissure diffusion indices of TASTPM seems to reflect the human pathology and are supported by white matter injury as detected in the histological staining.

In conclusion appropriate approaches with imaging analysis can satisfy the principle of the evaluation of homologous parameters in experimental models and in AD patients to help the translational research in the development of efficacious

therapies. Probably no single imaging marker will be sensitive enough to accurately evaluate pharmacological treatments but a collection of markers should be. The imaging “signatures” composed by

- caudate-putamen and frontal cortex volume of TASTPM and/or TauPS2APP
  - entorhinal cortex thickness of TASTPM and/or PDAPP
  - anterior commissure and corpus callosum diffusion indices of TASTPM
- completed by functional (fMRI), electrophysiological and biological markers of disease progression could improve our predictive power in testing disease modifying drugs.

As the amyloid hypothesis is one of main hypothesis being explored in the clinic, gamma secretase or BACE inhibitors or beta-amyloid antibodies will be used to validate the selected imaging markers. Further studies will then be conducted using other amyloid lowering agents, Tau kinase and neuroprotective drugs to test their predictive capacity in pharmacological interventions.

## 4 PART II: HUMAN IMAGING

### 4.1 Introduction

Longitudinal MRI studies in patients with MCI, who have a high risk of developing AD, will improve our capability to selectively quantify the pathological progressive changes and thus discover and define novel imaging indices of disease progression. Identifying biomarkers sensitive to disease progression is important to reduce sample size and follow-up length of the clinical trials hastening the clinical application of novel therapeutic agents. Targeting a specific patient population is difficult for a single centre and often required a multisite approach to increase the population and statistical power of the analysis where MRI scanner of different models and manufactures account for results variability. Other sources of variability could be (i) lack of MRI acquisition protocols harmonization, (ii) intra-site variability induced by intrinsic instability of hardware components and magnetic field, (iii) changes in subject positioning. The measure reproducibility is fundamental to detect real changes in patients during longitudinal studies and neither morphometric nor diffusion quantitative estimation reliability is trivial [179].

In order to combine data obtain from 1.5T and 3T, the two widely available scanner for clinical and research purpose, efforts focused on reproducibility of morphometric and diffusion measures across field strengths have been done [180, 181]. However, test-retest reliability of these measures across different 3T MRI scanners has been poorly investigated and thus its impact on statistical analysis is not clearly defined.

Manual segmentation of specific brain structures on MRI made by trained raters, with its high inter-rater reliability, is considered as the gold standard by many neuroimaging studies [182, 183]. However, due to its time-costs, manual segmentations are not practically applicable for longitudinal studies involving many subjects and different brain structures. Several automated and semi-automated algorithms have been proposed [184-191]. Advances in automated software tools permit to detect regional brain atrophy in a single subject [187, 192] allowing their application as a diagnostic marker for AD [193]. Recently, a longitudinal image processing framework has been developed [194] showing a significant increase in precision and discrimination power when compared with tools originally designed for cross-sectional analysis. Despite the wide usage of automated techniques, the within and across site test-retest reliability of morphometry and diffusion measures has been poorly investigated and thus its impact on statistical analysis is not clearly defined.

Previously across session reliability studies of T1-weighted 3D structural MRI data at 3T performed on the same scanner has been addressed mainly on Siemens TIM trio scanners [194-196] and only one study exists which investigated it on GE Excite scanner [197] (Table 8a). Regarding the longitudinal (LG) stream, current documented knowledge available from the literature suggests better reliability of the LG analysis from structural 3T MRI data but using special sequences at a single 3T site [198] and within-session variability [194].

To our knowledge, multi-site 3T DTI MRI studies evaluating across-session reproducibility are limited to few sites [199, 200], focused on young subjects and mostly used manual ROI selection [201, 202] (Table 8b) or dedicated to acquisitions with several averaged DTI scans [203].

<b>a</b>				
Study	MRI scanners (number)	Subjects (number) Age (mean $\pm$ SD)	Analysis tool	Reproducibility metrics (days between test-retest)
<b>This study</b>	Siemens Allegra (1), TIM Trio (2), Verio (1), Skyra (1); GE HDxt (1); Philips Achieva (2)	40 (5 sub/scanner) 63.2 $\pm$ 8.1	FSL	Volume and thickness Across-session (14-31)
(Huang et al., 2012)	Siemens TIM Trio (2)	6 24 $\pm$ 6	FIRST	Volume Across-session (31)
(Morey et al., 2010)	GE Excite (1)	23 23.4 $\pm$ 3.3	Freesurfer v4.5 and FIRST 1.2 (CS/LG)	Volume Across-session (7-9)
(Kruggel et al., 2010)	Siemens Allegra (3), Trio (13); GE Excite (5), Genesis (1); Philips Achieva (9)	ADNI dataset	FANTASM	Volume Across-session (30)
(Wonderlick et al., 2009)	Siemens TIM Trio (1)	2 groups: 5, 21.4 $\pm$ 3.8 6, 64.3 $\pm$ 12.2	Freesurfer v4.0.1 (CS)	Volume and thickness Across-session (14)
<b>b</b>				
Study	MRI scanners (number)	Subjects (number) Age (mean $\pm$ SD)	Reproducibility metrics (days between test-retest)	ROI
<b>This study</b>	Siemens Allegra (1), TIM Trio (2), Verio (1), Skyra (1); GE HDxt (1); Philips Achieva (2)	40 (5 sub/scanner) 63.2 $\pm$ 8.1	Mean FA, MD, $\lambda$ , $\lambda^{\perp}$ from ROI Across-session (14-31)	Atlas based cc_body, cc_genu, cc_spl, crtsp, SFL, ILF
(Huang et al., 2012)	Siemens TIM Trio (2)	6 24 $\pm$ 6	Mean FA, MD from ROI Across-session (31)	Manual segmentation WB, cc_spl, SFL, ILF
(Volmar et al., 2010)	GE Signa (2)	9 34 $\pm$ 8	Mean FA from ROI Across-session (1-95)	Manual segmentation WB, cc_spl, SFL, ILF
(Bisdas et al., 2008)	Philips Intera (1)	12 34 $\pm$ 11	Mean FA from ROI Across-session (14)	Manual segmentation cc_genu, cc_spl, int, crtsp
(Jansen et al., 2007)	Philips Achieva (1)	10 26 $\pm$ 2	Median FA voxel wise Across-session (5-25)	WB

**Table 8: Summary of studies that evaluated within-scanner across session test-retest reproducibility of 3T MRI morphometry (a) and diffusion (b) results on healthy subjects.** Abbreviations: CS, cross-sectional analysis; LG, longitudinal analysis, WB= whole brain, cc\_body= body of the corpus callosum, cc\_genu= genu of the corpus callosum, cc\_spl= splenium of the corpus callosum, crtsp= corticospinal tract, ILF= inferior lateral fasciculus, SFL= superior lateral fasciculus.

## **4.2 Part II: Human imaging study goals**

The choice of human data acquisition and data analysis strategies can affect reproducibility errors and is therefore crucial in longitudinal studies aimed at evaluating MRI-derived biomarkers for disease progression and/or treatment efficacy. Here we present work aimed at implementing standardized procedures to acquire and analyze multi-site structural and diffusion 3T MRI data for automated brain analysis.

In particular, this study involves 8 different 3T MRI sites (with Siemens, Philips and GE scanners) and each site scanned a group of elderly subjects scanned twice (test/retest design) at least a week apart to investigate reliability of the MRI-derived measures. The main goals of this are the following:

- Use the multi-site structural MRI to evaluate and compare the across-session test-retest reproducibility of brain segmentations derived from FreeSurfer using the cross-sectional (CS) and longitudinal (LG) analysis streams [2]. The morphometric data evaluated includes subcortical, ventricular and intracranial volumes as well as cortical thickness. The main hypothesis to test is: does the LG segmentation improve the reliability of the brain segmentations (relative to the CS analysis) within all MRI sites to produce also an improvement of the data when pooled across MRI sites?
- Use the diffusion tensor imaging MRI data (single acquisition during each test and retest session) to evaluate the across-session test-retest reproducibility of fractional anisotropy (FA), mean diffusivity (MD,  $10^{-3} \text{ mm}^2/\text{s}$ ), parallel ( $\lambda_{\parallel}$ ,  $10^{-3} \text{ mm}^2/\text{s}$ ) and axial ( $\lambda_{\perp}$ ,  $10^{-3} \text{ mm}^2/\text{s}$ ) diffusivities. The main hypothesis to test is: with the used acquisition and analysis protocol, are the reproducibility measures consistent with those reported in other similar studies?

## **4.3 Materials and methods**

### **4.3.1 Subjects**

Eight clinical sites participated in this study across Italy (Brescia, Verona, Genoa), Spain (Barcelona), France (Marseille, Lille, Toulouse) and Germany (Leipzig, Essen). The Brescia site was responsible for the coordination and analysis of the whole study and did not acquire MRI data. Each MRI site recruited 5 local volunteers within an age range of 50-80 years. The subject's age range corresponds to the same one of the clinical population that will be studied with the protocols tested in this reproducibility study. Each subject underwent two MRI sessions completed at least a week apart at the site, to minimize biological changes that could affect the reliability of the measures. Table 9 summarizes information about age, gender and test-retest interval times of the subjects recruited at each site. All participants were healthy volunteers with no history of major psychiatric, neurological or cognitive impairment, and provided written informed consent in accordance with the "classification" of the study as regards to the national regulations and laws in the different participating countries. In France, the study required an authorization from the national drug regulatory agency (Agence Nationale de Sécurité du Médicament et des produits de santé) and an approval from the Comité de Protection des Personnes Sud-Méditerranée 1 (Marseille), for the three French sites (Marseille, Lille, and Toulouse). In Germany, Spain and Italy the study required authorization from one Ethics Committee relevant to each institution: Essen (Ethik-Kommission des Universitätsklinikums Essen), Leipzig (Ethik-Kommission der Universität Leipzig), Barcelona (Comité de Ètica e Investigació Clínica Hospital Clínic de Barcelona), Brescia (Comitato Etico Istituzioni Ospedaliere Cattoliche, CEIOC) and Genoa (Comitato Etico IRCCS-Azienda Ospedaliera Universitaria San Martino-IST).



MRI site location	Site 1 Verona	Site 2 Barcelona	Site 3 Marseille	Site 4 Lille	Site 5 Toulouse	Site 6 Genoa	Site 7 Leipzig	Site 8 Essen
Subjects' age: mean±stdev, (range) years	67.8±9.9 (26)	74.6±2.7 (6)	66.0±8.3 (20)	64.2±5.3 (13)	59.2±4.5 (12)	58.2±2.2 (5)	62.8±2.6 (6)	52.4±1.5 (3)
Test-Retest Time interval (days)	28±23	10±3	23±22	15±11	14±10	24±17	13±3	11±5
Gender, (females/N)	2/5 (40%)	5/5 (100%)	4/5 (80%)	3/5 (60%)	3/5 (60%)	2/5 (40%)	3/5 (60%)	2/5 (40%)
3T MRI scanner	Siemens Allagra	Siemens TrioTim	Siemens Verio	Phillips Achieva	Phillips Achieva	GE HDxt	Siemens TrioTim	Siemens Skyra
MR system software version	VA25A	B17	B17	3.2.2	3.2.2	15 M4A	B17	D11
TX / RX coil	Birdcage	Body / 8-chan.	Body / 12-chan.	Body / 8-chan.	Body / 8-chan.	Body / 8-chan.	Body / 8-chan.	Body / 20-chan.
Parallel Imaging: method, acceleration	None	GRAPPA 2	GRAPPA 2	SENSE 1.5	SENSE 1.5	ASSET 2	GRAPPA 2	GRAPPA 2
<b>MPRAGE</b>								
TE (ms, shortest)	2.83	2.98	2.98	3.16	3.16	2.86	2.98	2.03
Acquisition time (min:sec)	9:50	5:12	5:12	6:50	6:50	4:43	5:12	5:12
<b>DTI</b>								
TR (ms)	9300	8000	9300	8000	8000	14974	8000	9100
TE (ms, shortest)	87	82	84	75	75	81	84	78
Acquisition time (min:sec)	5:53	5:14	6:04	5:27	5:27	8:59	5:12	5:23

**Table 9: Summary of demographic, MRI system and acquisition differences across MRI sites.**

#### 4.3.2 MRI acquisitions

The eight 3T MRI sites that participated in this study used different MRI system vendors and models (Siemens, GE, and Philips). Table 2 summarizes the main MRI system differences across sites. Each MRI scanning session consisted of several acquisitions, including: anatomical T2\*, anatomical FLAIR, resting state fMRI, B0 map, DTI and two anatomical T1 scans, with a total acquisition time of approximately 35 minutes. The two anatomical T1 scans were used for brain morphometry analysis (3D MPRAGE: sagittal acquisition, square FOV = 256 mm, 1x1x1 mm<sup>3</sup>, TR/TI = 2300/900 ms, flip angle= 9°, no fat suppression, full k-space, no averages). These parameters were largely based on the MPRAGE recommendations from ADNI 2 (<http://adni.loni.ucla.edu/research/protocols/mri-protocols/>) except for two factors: nominal spatial resolution (we used isotropic 1 mm<sup>3</sup> instead of 1x1x1.2 mm<sup>3</sup>) and image acceleration (when allowed by the RF coil we used an acceleration factor of two, instead of no acceleration). The main motivations for using acceleration were that most modern 3T scanners allow for it, and the reduction of scanning time is expected to reduce the sensitivity to head motion artifacts, even at an expense of some loss in signal.

The single DTI scan was used for brain diffusion analysis (b-value= 700 s/mm<sup>2</sup>, 5 b0 volumes, 30 gradient directions, 2x2x2mm<sup>3</sup>, acceleration factor 2 (GRAPPA, SENSE and ASSET in Siemens, Philips and GE systems, respectively), axial slice acquisition. The parallel acquisition methods were different across sites, the choices were made based on the optimal or possible options available at the different platforms (see Table 9). All images from multi-channel coils were reconstructed by the scanner as the sum of the squares across channels. When allowed by the MRI system, images were reconstructed and saved without additional filtering options.

### 4.3.3 Data preparation

Imaging data were initially anonymized at each site by replacing the subject name with a unique identifier using the free DicomBrowser tool (<http://hg.xnat.org/dicombrowser>). Anonymized dicom data were then compressed and uploaded on to a data sharing system accessible to all member sites, from where they were subsequently downloaded for analysis at central site (Brescia). Downloaded anonymized dicom data were converted to nifti format using the free dcm2nii software (<http://www.mccauslandcenter.sc.edu/mricro/mricron/dcm2nii.html>, output format FSL – 4D NIFTI nii) from which the original dicom converted to nifty files were utilized. All data were visually inspected for quality assurance prior to analyses to check that there were no mayor visible artifacts, including motion, wrap around, RF interference and signal intensity or contrast inhomogeneities. For diffusion images motion for the subjects during the acquisition was also performed. Each subject had a total of four anatomical scans (two from the test session and two from the retest session) and two diffusion scans (one from the test and one from the retest session). No within-session averaging was done.

### 4.3.4 Data post-processing

#### 4.3.4.1 Volumetric Measurement

Each MPRAGE anatomical volume was analyzed in FreeSurfer [204, 205] to automatically generate subject-specific cortical [192, 206] and subcortical [187] ROIs. For each subject we used two FreeSurfer analysis streams: the cross-sectional (CS) stream, which treats each segmentation independently and the longitudinal-stream (LG), which creates a within-subject template from the CS results as prior knowledge to drive the segmentation of multiple time points, allowing for improved within-session test-retest reproducibility of morphometric results relative to the CS analysis [194].

Our study is focused on a subset of the segmented regions which are of interest in neurodegenerative diseases. The volumetric ROIs included the hippocampal formation, amygdala, caudate nucleus (caudate), putamen, globus pallidus (pallidum), thalamus, lateral ventricles and total intracranial volume. The cortical ROIs included the parahippocampus gyrus, fusiform gyrus, superior temporal gyrus, precuneus, superiorparietal gyrus, supramarginal gyrus, lateral occipital gyrus, lingual gyrus and superior frontal gyrus [207]. For each of these structures (except the intracranial volume) the right and left hemisphere volumes are estimated separately on each anatomical scan. A total of 318 brain volumes were processed (8 MRI sites, 5 subjects per site, 4 volumes per subject and 2 processing streams). The segmentation results were visually inspected prior to the

volume and thickness analysis to confirm that no mayor errors were present. No manual edits were done. All analyses were done using FreeSurfer version 5.1, running on a Linux workstation (Ubuntu 10.04) equipped with Intel CPU 8 x 3.07 GHz processors and 7.9 GB of RAM.

#### 4.3.4.2 Diffusion data analysis: estimation of structural connectivity measures

Data analysis of each DTI volume included Eddy current and motion correction followed co-registration to an ICBM atlas and estimation of FA, MD ( $10^{-3}$  mm<sup>2</sup>/s),  $\lambda_{||}$  ( $10^{-3}$  mm<sup>2</sup>/s) and  $\lambda_{\perp}$  ( $10^{-3}$  mm<sup>2</sup>/s) from a full-brain voxel-based track-based spatial statistics (TBSS) analysis [4]. Each site's FA maps were projected into a common site-specific white matter (WM) skeleton using randomized 5000 permutations. Atlas-based WM regions of interest (ROIs) were defined for each subject and session by linear co-registration of the JHU-ICBM-1mm atlas to each subject's space. The ROI analysis was focused on the corpus callosum (body, genu and splenium), corticospinal tract (left/right), inferior and superior lateral fasciculi (left/right). Each site's reproducibility mean was the average across subjects.

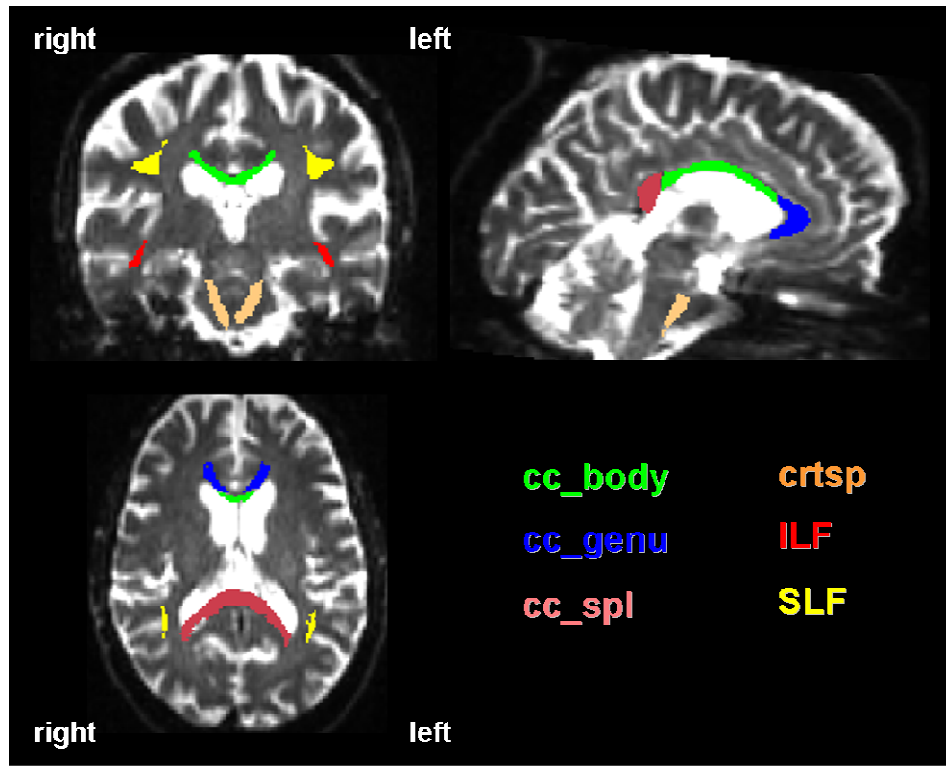


**Fig 23. Examples of  $b_0$  image of a healthy volunteer overlaid with the atlas-based masks used for the automatic diffusion quantification.**

Abbreviations: cc\_body= body of the corpus callosum, cc\_genu= genu of the corpus callosum, cc\_spl= splenium of the corpus callosum, crtsp= corticospinal tract, ILF= inferior lateral fasciculus, SLF= superior lateral fasciculus.

#### 4.3.5 Evaluation of reliability

To evaluate the reliability of the brain segmentation and diffusion results we analyzed their variability, or reproducibility error, across the test-retest sessions for each site. There are several sources of variability for a fixed scanner, which include variability from hydration status (expected to be small if scans are repeated within a short time interval), variability due to slightly different acquisitions in the two sessions (head position change in the scanner, motion artifacts, scanner instability, etc.), and finally variability due to the imaging processing methods themselves. In addition, in a multi-center study there is also the added variability from the different MRI systems (vendor, model, acquisition parameters). In this study the goals were to evaluate the across session reliability of FreeSurfer brain segmentations, within each site and across sites, both for the CS and LG processing streams and the across session reliability of diffusion parameters extracted using an atlas-based ROIs method.

Since every subject had segmentation results derived separately from each of the two test and the two retest MPRAGE volumes, we used these four possible test-retest comparisons across sessions to estimate a mean across-session variability error per subject. For diffusion reliability was simpler because we had one test and one retest. As variability error we used the dimensionless measure of absolute percent change of volume (or thickness or diffusion) of a structure with respect to its average. In other words, for each subject and for each structure the across-session variability error was estimated as follows:

$$\varepsilon_{ij} = 200 \times \frac{|V_{retest_i} - V_{test_j}|}{V_{retest_i} + V_{test_j}} \quad (6)$$

$$\text{Mean variability error} = \frac{\varepsilon_{11} + \varepsilon_{12} + \varepsilon_{21} + \varepsilon_{22}}{4} \quad (7)$$

where the indices  $i$  and  $j$  can take values 1 or 2 to refer to the first or second MPRAGE volume (or thickness or diffusion index) in each of the test ( $V_{test}$ ) and retest ( $V_{retest}$ ) sessions. The group variability error for every MRI site and brain structure was then averaged across subjects, within each analysis stream (or diffusion parameter) separately. Such estimation of variability can be interpreted as the mean measurement error. The measure was chosen because it is intuitive and because the estimation of the means is more robust than the estimation of the variance from the signed differences, in particular for low number of subjects.

Another way to study measure reproducibility is using the coefficient of variation (CV) or the intraclass correlation coefficient (ICC). The former describes the dispersion of the values while the latter expresses which part of variance can be explained by biological variation between subjects rather than by measurement error within subjects. CV and ICC for diffusion measures were estimated as follow:

$$CV = 100 \times \frac{\sigma}{\mu} \quad (8)$$

$$ICC = \frac{MS(B) - MS(W)}{MS(B) + (m-1) MS(W)} \quad (9)$$

where  $\sigma$  is the standard deviation and  $\mu$  the mean between test and retest,  $MS(B)$  is the between subjects mean square,  $MS(W)$  is the within subject mean square and  $m$  is the number of the observations per subject. For test-retest data on healthy elderly acquired at the same scanner using the same DTI sequence, the biological variation should be small and the CV and ICC should be high.

The distributions of volume (or thickness) differences plotted against volume (or thickness) means across sessions were examined with a Bland-Altman analysis [208]. These plots show the spread of data, the mean difference and the limits of agreement, and were used to confirm that the distributions were approximately symmetric around zero, that there were no outliers.

An additional evaluation of variability was done by computing the spatial reproducibility of the segmented subcortical and ventricular volumes or the of the white matter ROIs. Spatial reproducibility was examined computing the Dice coefficients for the volume overlap [209] on the co-registered test-retest volumes segmented with both the Freesurfer streams. Similar analysis was done for diffusion ROIs where Dice coefficient was performed on the co-registered test-retest ROIs. In particular, given two different labels (test and retest sessions) of a structure from the same subject, denoted by  $V_{test}$  and  $V_{retest}$  the Dice coefficient is given by [209]:

$$D_{ij} = \frac{1}{2} \frac{\text{Vol}(V_{retest_j} \cap V_{test_i})}{\text{Vol}(V_{retest_j}) + \text{Vol}(V_{test_i})} \quad (8)$$

$$\text{Mean } D = \frac{D_{11} + D_{12} + D_{21} + D_{22}}{4} \quad (9)$$

For identical spatial labels,  $D(V_{retest}, V_{test})$  achieves its maximum value of one, with decreasing values indicating less perfect overlap. For each subject the Dice coefficients were calculated as an average across the right and left hemispheres. The group results for each site were generated by averaging the Dice coefficients across subjects for each structure.

#### 4.3.6 Statistical analysis

The following statistical analyses tests were done, using matlab and SPSS (v.13.0):

- To test for MRI site effects on subject's age distributions, a one-way analysis of variance (ANOVA) was used, with MRI site as factor.
- To test for MRI site effects of mean volume, mean thickness, mean FA, mean MD, mean  $\lambda_{||}$ , mean  $\lambda_{\perp}$ , mean reproducibility error (of volumes, thickness and DTI parameters) and mean spatial overlap, a one-way Kruskal-Wallis test (non-parametric version of ANOVA) was used with MRI site as factor.
- To test for differences between the mean reproducibility error of the two Freesurfer streams (LG vs. CS) for each structure and site, the two-tailed Wilcoxon test was used (non-parametric version of the paired Student's t-test).

## 4.4 Results

In this study, we estimate the test-retest reliability of morphometry and diffusion measures derived from 3T MRI data on healthy elderly volunteers scanned in two separate sessions at least one week apart at different MRI sites (eight 3T MRI scanners from different vendors: GE, Siemens, Philips). This short period between the test and retest sessions was chosen to minimize biological changes that could affect the reliability of the measures and to mimic the variability expected from separate sessions, which are common in longitudinal studies. Moreover, for morphometry analysis, was evaluated how the reproducibility error is affected by Freesurfer processing stream (CS, LG). The 40 subjects enrolled (5 for each center, see Table 9 for summary demographic information) had similar age distribution except for site 2 (older group, mean age  $74.6 \pm 2.7$  years, significantly different from sites 5, 6, 7, 8, ANOVA,  $p < 0.05$ ) and site 8 (younger group, mean age  $52.4 \pm 1.5$  years, significantly different from sites 1, 2, 3, 4, ANOVA,  $p < 0.05$ ). There were no age distribution differences between the other MRI sites. The overall mean time interval between the test and retest sessions was 17 days.

### 4.4.1 Morphometry Results

One goal was to compute and evaluate the segmentations of a total of 320 brain volumes: 8 MRI sites, 5 subjects per site, 4 acquisitions per subject (two test, two retest), 2 Freesurfer segmentation analysis protocols. In practice we had 3 missing volumes: two subjects of site 5 had missing MPRAGE volume repetitions during the test session, and one MPRAGE from site 1 failed the segmentation for unknown reasons. Visual inspection of Freesurfer segmented images showed a high similarity of results quality across sites (Fig 24).

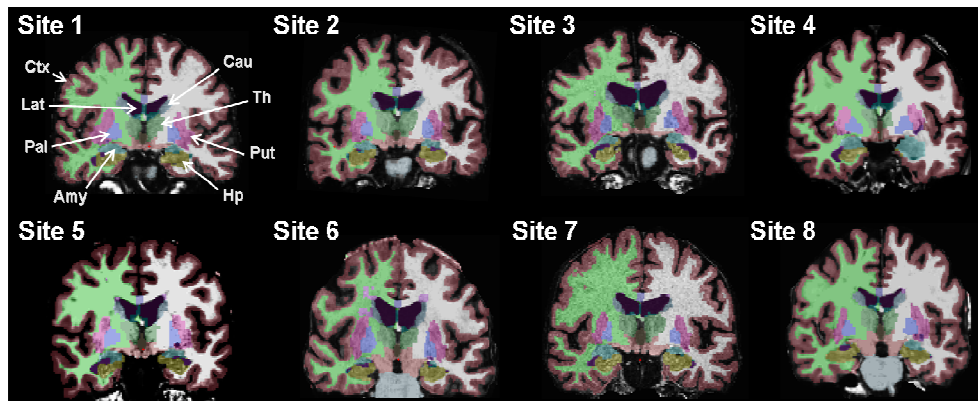


**Figure 24:** Sample MPRAGE images and Freesurfer segmentation results across different 3T MRI sites for qualitative comparison. Abbreviations: Hp= hippocampus, Amy= amygdala, Cau= caudate, Put= putamen, Pal= pallidum, Thal= thalamus, Lat= lateral ventricle, Ctx= cerebral cortex. See Table 2 for MRI sites characteristics.

#### 4.4.1.1 Estimation of brain morphometric volumes across MRI sites

Table 10 summarizes the group mean volumetric results (subcortical, ventricle and intracranial), averaged across hemispheres and across the test-retest sessions, for each MRI site as derived from the Freesurfer LG segmentation stream. A Kruskal-Wallis test for MRI site effect on the hemispheric volumes showed that there were significant site effects ( $p < 0.01$ ) for only 2 of the 15 structures evaluated: the left putamen and right pallidum. This variability of morphometric results across sites is consistent with the fact that the groups of subjects were different at the various sites, and might simply reflect anatomical variability.

Structure Volume	MRI Sites: Volumetric estimates (mm <sup>3</sup> )							
	Site 1	Site 2	Site 3	Site 4	Site 5	Site 6	Site 7	Site 8
<b>Hp</b>	3652 ± 394	3643 ± 399	3831 ± 382	4170 ± 251	4018 ± 241	4182 ± 209	3716 ± 396	3859 ± 589
<b>Amy</b>	1573 ± 239	1330 ± 229	1590 ± 180	1804 ± 320	1735 ± 263	1576 ± 179	1485 ± 211	1587 ± 248
<b>Cau</b>	3577 ± 293	2707 ± 305	3428 ± 265	3235 ± 295	3172 ± 207	4099 ± 434	3453 ± 295	3736 ± 992
<b>Put</b>	5152 ± 525	4458 ± 410	5051 ± 364	5441 ± 897	4950 ± 241	6713 ± 1008	4681 ± 260	5321 ± 622
<b>Pal</b>	1579 ± 167	1292 ± 118	1570 ± 248	1578 ± 248	1342 ± 342	2209 ± 409	1476 ± 189	1551 ± 324
<b>Thal</b>	6157 ± 525	5302 ± 458	6279 ± 745	6290 ± 813	6305 ± 646	7735 ± 731	5827 ± 424	6178 ± 827
<b>Lat</b>	14055 ± 7296	7579 ± 2485	11478 ± 5577	9150 ± 3252	6990 ± 2427	11509 ± 3965	13081 ± 6244	8018 ± 4397
<b>ICV</b>	1332302 ± 18476	1187475 ± 47690	1426896 ± 112925	1233636 ± 213199	1135640 ± 84246	1544876 ± 227217	1387241 ± 107959	1367857 ± 208535

**Table 10: Volume estimates across sites.** Within-site group means and standard deviation (across subjects, scanner sessions and hemispheres) of subcortical, ventricle and intracranial volumes derived from the Freesurfer longitudinal segmentation stream. Abbreviations: Hp= hippocampus, Amy= amygdala, Cau= caudate, Put= putamen, Pal= pallidum, Thal= thalamus, Lat= lateral ventricle, ICV= intracranial volume. See Table 2 for MRI sites characterization.

#### 4.4.1.2 Estimation of volume reproducibility: effects of MRI sites and segmentation analyses

Figure 25 shows an example of a Bland-Altman plot for a single site on two sample structures: the hippocampus (left) and the amygdale (right). The plot shows, for site 2, the distribution of across-session volume differences relative to the volume means for the two analysis streams, CS (top) and LG (bottom). For each brain hemisphere (left: red crosses, right: blue circles) the mean volume difference (solid horizontal line) and the limits of agreement ( $\pm 2$  standard deviations, interrupted horizontal lines) are shown. The 20 data points in each plot correspond to the 5 subjects and their respective 4 test-retest possible comparisons. As it can be seen, there are no outliers (all data points within 3 standard deviations) and the volume differences are symmetrically distributed around zero. Similar results were found for other sites and structures. In this example it is also possible to see how the spread of the data is reduced in the LG relative to the CS analysis.

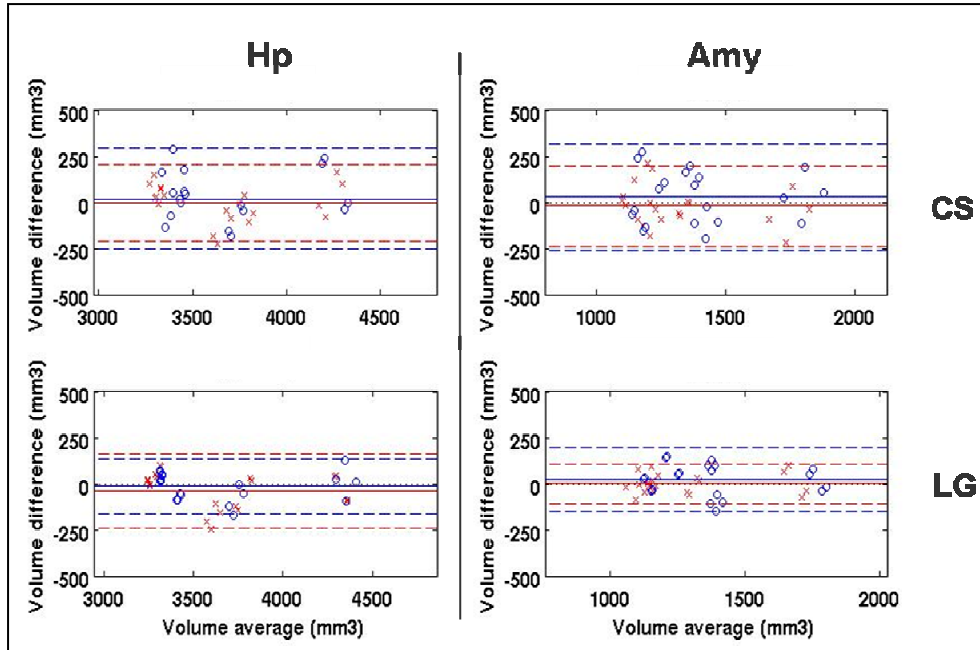


**Figure 25:** Sample distribution of cross-sectional (CS) and longitudinal (LS) volume reproducibility results (Site 2) in hippocampus (Hp) and amygdala (Amy): Bland-Altman plots showing volume difference versus volume mean (two single MPRAGE acquisitions per session, subjects,  $n=5$ ). For each brain hemisphere (left: red crosses, right: blue circles) the mean volume difference (solid horizontal line) and the limits of agreement ( $\pm 2$  standard deviations, interrupted horizontal lines) are shown. For reference, zero volume difference is shown as a black dotted line.

Table 11 summarizes the across-session test-retest reproducibility errors of the various segmented volumes for each site, for both analysis streams (CS and LG). In each site the mean reproducibility error is computed as a mean across subjects, across the four test-retest segmentations and across the two brain hemispheres where relevant (intracranial volume is the only exception). No significant MRI site effects were found on the reproducibility error, regardless of structure and analysis stream used for the brain segmentations (Kruskall-Wallis test,  $p<0.01$ ). Averaging the errors across sites allows to summarize the effects of analysis on the various structures (Table 3, last column). For all structures the LG stream showed a significantly lower reproducibility error relative to the CS stream (Wilcoxon test,  $p<0.01$ ), except for the lateral ventricle volumes, which gave no significant differences between analyses streams. When considering the separate hemispheric volumes within each site and test across all structures, we also found that in all sites the LG analysis gave significantly lower reproducibility errors relative to the CS analysis (Wilcoxon test,  $p<0.05$ ).



Structure and analyses		MRI Sites: Volumetric reproducibility errors (%)								Mean error across MRI sites (%)
		Site 1	Site 2	Site 3	Site 4	Site 5	Site 6	Site 7	Site 8	
Hp	CS	3.50 ± 2.84	2.58 ± 2.02	3.56 ± 3.52	1.99 ± 1.59	2.40 ± 1.71	4.93 ± 4.53	3.34 ± 2.38	3.79 ± 2.58	3.27 ± 1.82
	LG	1.95 ± 1.77	1.92 ± 1.57	1.96 ± 1.44	0.91 ± 0.71	1.80 ± 1.31	2.07 ± 1.99	1.94 ± 1.40	1.76 ± 1.27	1.86 ± 0.90
Amy	CS	7.38 ± 7.04	8.02 ± 5.80	4.84 ± 3.73	4.26 ± 4.54	6.76 ± 6.80	8.40 ± 9.10	7.13 ± 5.37	9.46 ± 8.95	7.07 ± 3.12
	LG	4.59 ± 3.64	4.57 ± 3.15	3.56 ± 2.29	2.49 ± 1.96	3.48 ± 3.27	3.68 ± 2.63	2.91 ± 3.05	5.17 ± 5.64	3.86 ± 1.68
Cau	CS	2.76 ± 1.65	2.78 ± 2.26	3.19 ± 4.07	2.27 ± 1.49	2.37 ± 1.73	2.76 ± 2.07	2.16 ± 1.88	2.28 ± 2.01	3.46 ± 2.67
	LG	1.35 ± 1.07	1.69 ± 1.27	2.45 ± 3.47	1.64 ± 1.38	2.03 ± 1.35	2.46 ± 1.91	1.56 ± 1.26	1.51 ± 0.88	1.80 ± 1.18
Put	CS	5.38 ± 3.91	5.47 ± 4.94	3.14 ± 3.00	3.70 ± 3.52	4.32 ± 4.54	5.51 ± 3.86	4.98 ± 7.45	4.34 ± 5.31	4.07 ± 2.88
	LG	3.24 ± 2.96	2.09 ± 1.63	1.88 ± 1.26	2.07 ± 1.75	1.70 ± 1.44	2.82 ± 2.21	1.66 ± 1.41	1.52 ± 0.99	2.12 ± 1.02
Pal	CS	7.47 ± 7.83	5.54 ± 5.17	5.71 ± 4.70	6.11 ± 7.40	8.82 ± 10.70	11.21 ± 7.82	6.28 ± 7.13	8.34 ± 8.14	6.91 ± 6.82
	LG	5.94 ± 7.08	3.15 ± 3.16	3.63 ± 2.37	2.23 ± 1.30	4.46 ± 4.29	4.99 ± 4.16	2.67 ± 1.91	2.99 ± 2.44	3.14 ± 2.28
Thal	CS	4.15 ± 3.37	3.65 ± 3.18	4.09 ± 3.07	3.69 ± 3.21	5.52 ± 7.30	7.29 ± 5.19	5.40 ± 7.02	5.94 ± 7.01	5.46 ± 3.17
	LG	2.27 ± 1.71	1.78 ± 1.60	1.51 ± 1.17	1.79 ± 1.21	1.88 ± 1.38	2.11 ± 1.87	1.52 ± 1.44	1.42 ± 1.45	2.14 ± 0.87
Lat	CS	3.43 ± 2.64	1.88 ± 1.43	2.50 ± 1.69	2.35 ± 1.66	2.73 ± 2.68	2.36 ± 2.62	1.67 ± 1.28	1.90 ± 2.07	2.36 ± 1.46
	LG	2.37 ± 2.30	2.49 ± 1.49	2.70 ± 1.39	2.00 ± 0.98	2.47 ± 1.27	1.54 ± 1.24	2.17 ± 1.56	2.73 ± 2.73	2.31 ± 1.24

**Table 11: Brain volumetric reproducibility errors for the various 3T MRI sites derived from the cross-sectional (CS) and longitudinal (LG) Freesurfer segmentations.** Within each site the mean reproducibility errors is computed across subjects, across the four test-retest acquisitions and across brain hemispheres. There are no significant MRI site effects, regardless of analysis (Kruskal-Wallis test,  $p < 0.01$ ). The last column shows the reproducibility errors for each site and analysis when averaged across sites. Except for the lateral ventricles, for all other structures the reproducibility errors of LG are significantly lower than those from CS analysis (Wilcoxon test,  $p < 0.01$ ). Abbreviations for the segmented volumes: Hp= hippocampus, Amy= amygdala, Cau= caudate, Put= putamen, Pal= pallidum, Thal= thalamus, Lat= lateral ventricle volume. See Table 2 for MRI sites characterization.

Figure 26 illustrates in a plot an example of the findings reported in Table 3, showing the distribution of volumetric reproducibility errors (%) across the eight MRI sites for just two structures, the hippocampus (left) and the amygdale (right). Each point represents an MRI site, with the longitudinal error on the vertical axis and the cross sectional error along the horizontal axis, with corresponding within-site standard deviations. The diagonal unity line corresponding to perfect agreement between the two measures is plotted as a thin reference line. The fact that the overall reproducibility error is smaller with the longitudinal line can be easily seen by having all dots under the unity line. The vertical and horizontal dotted lines mark the maximum range of the spread in absolute errors. It can be seen that the spread of errors for the longitudinal stream (range along vertical axis) is smaller than the spread of errors given by the cross-sectional stream (range

along horizontal axis). Overall this means that for the across-session test-retest errors in volumetric estimates the longitudinal stream gives lower reproducibility errors and also lower variability across MRI sites.

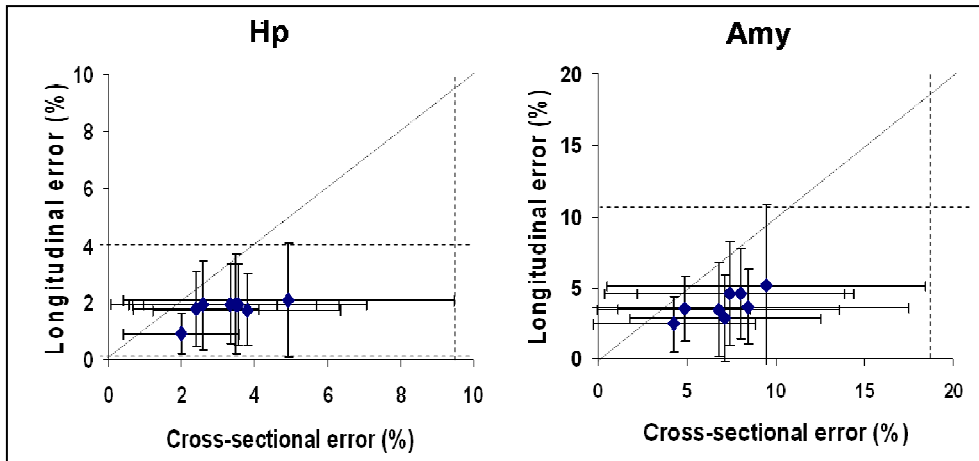


**Figure 26: Across-session test-retest reproducibility errors of hippocampus and amygdale volume estimates, effects of MRI site and processing stream.**

Reproducibility errors from the longitudinal and cross-sectional analysis for each one of the eight 3T MRI sites, with their respective within-site standard deviations.

Data derived from Table 11.

#### **4.4.1.3 Estimation of spatial reproducibility of volumetric segmentations: effects of MRI sites and segmentation analyses**

The across-session test-retest spatial overlaps for both analysis streams are reported in Table 12, which shows for each site, structure and analysis the mean Dice coefficient of spatial overlap averaged across subjects, across the 4 test-retest scans and across hemispheres. There were no significant MRI site effects of the Dice coefficients, regardless of analysis stream and structure (Kruskal-Wallis test,  $p < 0.01$ ). When averaged across MRI sites, the LG analysis showed significantly higher spatial reproducibility relative to the CS analysis, for all brain structures evaluated (Wilcoxon test,  $p < 0.01$ ). When grouping hemispheric structures within each site separately we also found that the spatial reproducibility of the LG analysis was significantly higher than that obtained with the CS analysis (Wilcoxon test,  $p < 0.02$ ).

Structure and analyses	MRI Sites: Dice coefficients for spatial overlap								Mean Dice across MRI sites	
	Site 1	Site 2	Site 3	Site 4	Site 5	Site 6	Site 7	Site 8		
Hp	CS	0.88 ± 0.02	0.89 ± 0.02	0.87 ± 0.03	0.89 ± 0.02	0.88 ± 0.02	0.88 ± 0.04	0.88 ± 0.06	0.84 ± 0.04	0.88 ± 0.02
	LG	0.92 ± 0.02	0.94 ± 0.02	0.91 ± 0.06	0.95 ± 0.03	0.93 ± 0.03	0.91 ± 0.07	0.95 ± 0.01	0.88 ± 0.06	0.93 ± 0.03
Amy	CS	0.83 ± 0.04	0.84 ± 0.03	0.85 ± 0.03	0.87 ± 0.03	0.85 ± 0.03	0.81 ± 0.02	0.91 ± 0.05	0.90 ± 0.03	0.84 ± 0.03
	LG	0.89 ± 0.03	0.91 ± 0.02	0.90 ± 0.05	0.94 ± 0.02	0.91 ± 0.04	0.89 ± 0.04	0.92 ± 0.01	0.87 ± 0.06	0.91 ± 0.03
Cau	CS	0.88 ± 0.02	0.87 ± 0.01	0.86 ± 0.03	0.87 ± 0.02	0.87 ± 0.02	0.84 ± 0.03	0.86 ± 0.12	0.87 ± 0.02	0.87 ± 0.02
	LG	0.93 ± 0.02	0.93 ± 0.02	0.91 ± 0.04	0.94 ± 0.01	0.93 ± 0.03	0.89 ± 0.04	0.94 ± 0.01	0.92 ± 0.04	0.92 ± 0.03
Put	CS	0.86 ± 0.03	0.88 ± 0.03	0.88 ± 0.02	0.89 ± 0.03	0.88 ± 0.03	0.86 ± 0.02	0.86 ± 0.11	0.87 ± 0.02	0.87 ± 0.02
	LG	0.91 ± 0.02	0.94 ± 0.01	0.92 ± 0.02	0.95 ± 0.01	0.94 ± 0.02	0.92 ± 0.03	0.94 ± 0.01	0.92 ± 0.03	0.93 ± 0.02
Pal	CS	0.80 ± 0.14	0.78 ± 0.15	0.81 ± 0.09	0.81 ± 0.16	0.75 ± 0.21	0.81 ± 0.04	0.77 ± 0.21	0.74 ± 0.19	0.79 ± 0.10
	LG	0.90 ± 0.05	0.90 ± 0.05	0.90 ± 0.05	0.94 ± 0.03	0.89 ± 0.07	0.89 ± 0.04	0.92 ± 0.02	0.89 ± 0.05	0.91 ± 0.04
Thal	CS	0.91 ± 0.01	0.92 ± 0.01	0.91 ± 0.02	0.92 ± 0.01	0.91 ± 0.03	0.89 ± 0.02	0.83 ± 0.07	0.82 ± 0.04	0.91 ± 0.01
	LG	0.95 ± 0.01	0.96 ± 0.01	0.95 ± 0.02	0.97 ± 0.01	0.96 ± 0.02	0.94 ± 0.02	0.96 ± 0.01	0.95 ± 0.02	0.96 ± 0.02
Lat	CS	0.92 ± 0.02	0.90 ± 0.03	0.91 ± 0.03	0.90 ± 0.03	0.88 ± 0.04	0.89 ± 0.02	0.92 ± 0.05	0.85 ± 0.06	0.90 ± 0.03
	LG	0.95 ± 0.01	0.95 ± 0.03	0.94 ± 0.03	0.95 ± 0.02	0.93 ± 0.05	0.92 ± 0.03	0.96 ± 0.01	0.89 ± 0.07	0.94 ± 0.03
All	CS	0.87 ± 0.04	0.87 ± 0.05	0.87 ± 0.04	0.88 ± 0.04	0.86 ± 0.05	0.85 ± 0.04	0.86 ± 0.05	0.84 ± 0.02	
	LG	0.92 ± 0.02	0.93 ± 0.02	0.92 ± 0.02	0.95 ± 0.01	0.93 ± 0.02	0.91 ± 0.02	0.94 ± 0.02	0.90 ± 0.03	

**Table 12: Spatial reproducibility of volumetric segmentations. Within-site group mean volume overlap (DICE coefficient) and standard deviation (across subjects, scanner sessions and hemispheres) derived from the Freesurfer cross-sectional (CS) and longitudinal (LG) segmentation streams.**

There are no significant MRI site effects, regardless of structure and analysis (Kruskal-Wallis test,  $p < 0.01$ ). The last column shows the spatial reproducibility for each site and analysis when averaged across sites. For all structures the spatial reproducibility was significantly higher with the LG analysis relative to the CS analysis (Wilcoxon test,  $p < 0.01$ ). Abbreviations: Hp= hippocampus, Amy= amygdala, Cau= caudate, Put= putamen, Pal= pallidum, Thal= thalamus, Lat= lateral ventricle volume. See Table 2 for MRI sites characterization.

#### 4.4.1.4 Estimation of cortical thicknesses across MRI sites

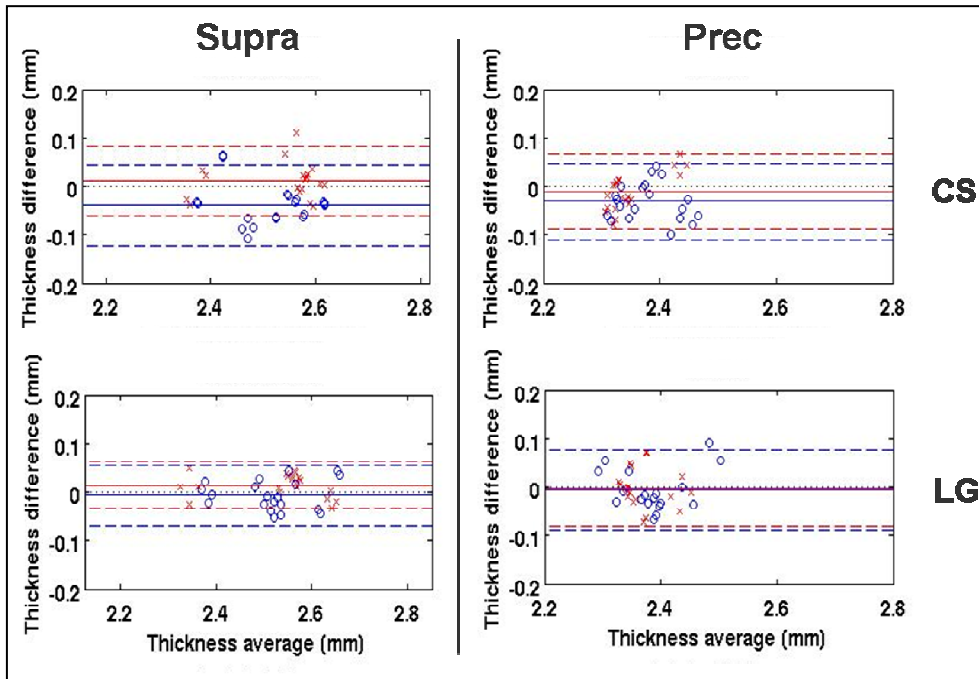
Table 13 summarizes the group mean cortical thickness results, averaged across hemispheres and across the test-retest sessions, for each MRI site as derived from the Freesurfer LG segmentation stream. The A Kruskal-Wallis test for MRI site effect on the hemispheric volumes showed that there were significant site effects ( $p < 0.01$ ) for only 3 of the 18 cortical structures evaluated: the right/left fusiform and the right superior frontal gyrus. This variability of morphometric results across sites is consistent with different degrees of anatomical variability from the different groups scanned at the different sites.

Structure thickness	MRI Sites: Cortical thickness estimates (mm)							
	Site 1	Site 2	Site 3	Site 4	Site 5	Site 6	Site 7	Site 8
<b>Fus</b>	2.55 ± 0.13	2.84 ± 0.15	2.74 ± 0.11	2.75 ± 0.08	2.82 ± 0.12	3.08 ± 0.11	2.75 ± 0.09	2.77 ± 0.08
<b>LatOc</b>	2.22 ± 0.15	2.31 ± 0.10	2.33 ± 0.12	2.14 ± 0.09	2.26 ± 0.18	2.44 ± 0.10	2.30 ± 0.09	2.30 ± 0.09
<b>Ling</b>	2.01 ± 0.07	1.97 ± 0.07	2.11 ± 0.11	1.96 ± 0.07	2.09 ± 0.15	2.15 ± 0.10	2.11 ± 0.08	2.01 ± 0.09
<b>Parahp</b>	2.79 ± 0.24	2.95 ± 0.25	2.88 ± 0.27	2.80 ± 0.26	3.04 ± 0.26	3.06 ± 0.24	2.89 ± 0.23	2.76 ± 0.32
<b>Prec</b>	2.26 ± 0.09	2.38 ± 0.05	2.38 ± 0.11	2.33 ± 0.09	2.40 ± 0.17	2.41 ± 0.19	2.34 ± 0.05	2.30 ± 0.07
<b>SupFr</b>	2.67 ± 0.11	2.71 ± 0.05	2.61 ± 0.13	2.83 ± 0.09	2.79 ± 0.10	2.64 ± 0.12	2.59 ± 0.08	2.59 ± 0.11
<b>SupPar</b>	2.14 ± 0.10	2.27 ± 0.05	2.27 ± 0.15	2.18 ± 0.07	2.22 ± 0.11	2.27 ± 0.09	2.26 ± 0.05	2.20 ± 0.07
<b>SupTem</b>	2.63 ± 0.10	2.70 ± 0.13	2.73 ± 0.12	2.80 ± 0.09	2.81 ± 0.10	2.86 ± 0.15	2.70 ± 0.16	2.77 ± 0.10
<b>Supra</b>	2.41 ± 0.09	2.51 ± 0.09	2.50 ± 0.13	2.46 ± 0.13	2.59 ± 0.13	2.61 ± 0.10	2.53 ± 0.12	2.53 ± 0.09

**Table 13: Cortical thickness estimates across sites. Within-site group means and standard deviation (across subjects, scanner sessions and hemispheres) of cortical thickness derived from the Freesurfer longitudinal segmentation stream. Abbreviations: Fus= Fusiform gyrus, LatOc= Lateraloccipital gyrus, Ling= Lingual gyrus, Parahp= Parahippocampal gyrus, Prec= Precuneus, SupFr= Superiorfrontal gyrus, SupPar= Superiorparietal gyrus, SupTem= Superiortemporal gyrus, Supra= Supramarginal gyrus. See Table 2 for MRI sites characterization.**

#### 4.4.1.5 Estimation of thickness reproducibility: effects of MRI sites and segmentation analysis

Figure 27 shows an example of a Bland-Altman plot for a single site on two sample cortical structures: the supramarginal gyrus (left) and the precuneus (right). The plot shows, for site 2, the distribution of across-session thickness differences relative to the thickness means for the two analysis streams, CS (top) and LG (bottom). For each brain hemisphere (left: red crosses, right: blue circles) the mean thickness difference (solid horizontal line) and the limits of agreement ( $\pm 2$  standard deviations, interrupted horizontal lines) are shown. The 20 data points in each plot correspond to the 5 subjects and their respective 4 test-retest possible comparisons. As it can be seen, there are no outliers (all data points within 3 standard deviations), the thickness differences are symmetrically distributed around zero. In this example it is also possible to see how the spread of thickness data is very similar in the LG and CS analyses.



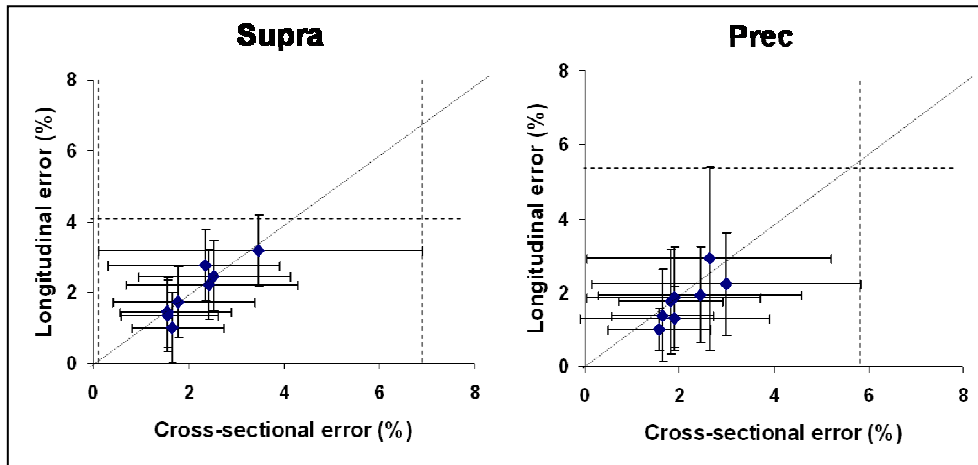
**Figure 27: Sample distribution of cross-sectional (CS) and longitudinal (LG) thickness reproducibility results (Site 2) in supramarginal gyrus (Supra) and precuneus (Prec):** Bland-Altman plots showing thickness difference versus thickness mean (two single MPRAGE acquisitions per session, subjects,  $n=5$ ). For each brain hemisphere (left: red crosses, right: blue circles) the mean volume difference (solid horizontal line) and the limits of agreement ( $\pm 2$  standard deviations, interrupted horizontal lines) are shown. For reference, zero volume difference is shown as a black dotted line.

Table 14 summarizes the mean across-session test-retest reproducibility errors in the cortical thickness estimates. For each site the mean error is averaged across subjects, across the four test-retest scans and across brain hemispheres. No significant MRI site effects were found on the reproducibility error, regardless of structure and analysis stream used for the brain segmentations (Kruskal-Wallis test,  $p < 0.01$ ). When averaged across MRI sites, the LG and CS analysis gave no significant differences in the thickness reproducibility (Wilcoxon test,  $p < 0.01$ ). When hemispheric structures were grouped and analyzed for each site separately we found that in four MRI sites the thickness reproducibility error was lower with the LG stream relative to the CS stream (Wilcoxon test,  $p < 0.02$ ), and not significantly different in the other four sites.

Structure and analyses		MRI Sites: Cortical thickness reproducibility errors (%)								Mean error across MRI sites (%)
		Site 1	Site 2	Site 3	Site 4	Site 5	Site 6	Site 7	Site 8	
Fus	CS	4.53 ± 3.24	2.03 ± 1.57	1.76 ± 1.35	1.73 ± 1.25	2.73 ± 2.07	1.92 ± 1.46	3.16 ± 2.47	2.62 ± 1.59	2.63 ± 1.45
	LG	4.31 ± 3.42	1.74 ± 1.49	1.66 ± 1.50	2.36 ± 1.56	3.07 ± 2.17	1.41 ± 1.12	1.55 ± 1.05	1.85 ± 1.21	2.34 ± 1.76
LatOc	CS	4.12 ± 3.93	2.01 ± 1.36	1.61 ± 1.27	1.25 ± 0.77	2.51 ± 2.10	2.47 ± 2.65	2.65 ± 2.06	2.00 ± 1.81	2.44 ± 1.75
	LG	2.18 ± 1.52	1.96 ± 0.99	1.69 ± 1.33	1.63 ± 1.56	2.34 ± 2.35	2.05 ± 1.59	2.21 ± 1.30	2.27 ± 1.41	2.11 ± 0.90
Ling	CS	5.14 ± 4.43	2.51 ± 1.27	2.35 ± 2.39	1.45 ± 1.19	2.25 ± 1.37	3.04 ± 2.19	2.55 ± 1.81	2.11 ± 1.92	2.63 ± 1.26
	LG	2.07 ± 1.45	1.88 ± 1.27	1.91 ± 1.62	1.92 ± 1.67	2.62 ± 2.28	2.05 ± 1.59	1.60 ± 1.50	2.37 ± 1.66	2.10 ± 1.02
Parahp	CS	5.51 ± 5.13	2.86 ± 1.97	2.60 ± 1.56	3.53 ± 2.19	3.15 ± 2.52	2.22 ± 1.97	2.47 ± 2.26	2.80 ± 2.23	3.22 ± 1.77
	LG	4.54 ± 3.59	1.76 ± 1.07	2.14 ± 2.02	2.25 ± 1.94	2.93 ± 2.48	1.52 ± 1.29	1.40 ± 1.24	2.49 ± 1.90	2.39 ± 1.37
Prec	CS	3.47 ± 3.45	1.57 ± 1.05	1.67 ± 1.06	1.55 ± 1.35	2.43 ± 1.86	2.36 ± 1.55	1.78 ± 1.60	2.53 ± 1.61	2.30 ± 1.66
	LG	3.18 ± 3.35	1.36 ± 0.98	1.02 ± 0.86	1.44 ± 0.99	2.23 ± 1.73	2.78 ± 2.03	1.72 ± 1.36	2.47 ± 1.56	2.13 ± 1.71
SupFr	CS	1.58 ± 0.93	1.93 ± 1.56	1.58 ± 1.48	4.46 ± 2.88	2.21 ± 1.96	2.83 ± 2.96	1.99 ± 1.87	3.37 ± 1.96	2.43 ± 1.69
	LG	1.57 ± 1.05	1.16 ± 0.81	1.57 ± 1.07	4.29 ± 2.98	1.78 ± 1.59	1.45 ± 1.02	1.53 ± 1.05	3.21 ± 3.21	2.06 ± 1.64
SupPar	CS	3.66 ± 4.07	1.68 ± 1.16	1.69 ± 1.37	1.50 ± 1.02	3.16 ± 2.28	3.19 ± 2.54	2.86 ± 2.59	3.01 ± 2.16	2.70 ± 2.04
	LG	2.27 ± 2.26	0.85 ± 0.59	1.34 ± 1.09	1.57 ± 1.65	2.20 ± 1.68	1.36 ± 0.93	1.55 ± 1.11	2.33 ± 1.54	1.73 ± 1.15
SupTem	CS	2.41 ± 2.10	1.38 ± 1.11	1.11 ± 0.73	1.55 ± 1.14	3.16 ± 2.28	2.76 ± 2.16	1.78 ± 1.57	1.53 ± 1.36	2.04 ± 1.16
	LG	2.58 ± 2.28	1.33 ± 0.78	1.03 ± 0.84	1.31 ± 0.89	1.35 ± 0.93	1.96 ± 1.79	1.17 ± 0.86	1.13 ± 1.22	1.63 ± 1.00
Supra	CS	2.63 ± 2.59	1.58 ± 1.09	1.64 ± 1.07	1.81 ± 1.10	1.88 ± 1.83	2.45 ± 2.14	1.91 ± 2.01	2.99 ± 2.83	2.16 ± 1.30
	LG	2.91 ± 2.47	1.00 ± 0.59	1.37 ± 1.24	1.75 ± 1.41	1.86 ± 1.35	1.92 ± 1.30	1.30 ± 0.86	2.23 ± 1.40	1.86 ± 1.11

**Table 14: Effects of MRI site and processing stream on thickness reproducibility.** Within-site group mean reproducibility error and standard deviation (across subjects, scanner sessions and hemispheres) derived from the Freesurfer cross-sectional (CS) and longitudinal (LG) segmentation streams. There are no significant MRI site effects, regardless of structure and analysis (Kruskal-Wallis test,  $p < 0.01$ ). The last column shows the spatial reproducibility for each site and analysis when averaged across sites. No significant differences were found between the thickness reproducibility errors from LG and CS analyses when grouped across sites (Wilcoxon test,  $p < 0.01$ ). Abbreviations: Fus= Fusiform gyrus, LatOc= Lateraloccipital gyrus, Ling= Lingual gyrus, Parahp= Parahippocampal gyrus, Prec= Precuneus, SupFr= Superiorfrontal gyrus, SupPar= Superiorparietal gyrus, SupTem= Superiortemporal gyrus, Supra= Supramarginal gyrus. See Table 2 for MRI sites characterization.

Figure 28 is similar to Figure 26, and it used to illustrate in a plot an example of the findings reported in Table 15. The figure shows the distribution of cortical thickness reproducibility errors (%) across the eight MRI sites for just two structures, the supramarginal gyrus (left) and the precuneous (right). Each point represents an MRI site, with the longitudinal error on the vertical axis and the cross sectional error along the horizontal axis, with corresponding within-site standard deviations. As it can be seen, the distribution of errors falls above and below the unity line, and the spread of errors of both analysis streams are comparable. In other words, the cross-sectional and longitudinal analysis streams do not give big differences in the across-session test-retest reproducibility errors of cortical thickness estimates.



**Figure 28: Across-session test-retest reproducibility errors of supramarginal gyrus and precuneus thickness estimates, effects of MRI site and processing stream.** Reproducibility errors from the longitudinal and cross-sectional analysis for each one of the eight 3T MRI sites, with their respective within-site standard deviations. Data derived from Table 14.

#### 4.4.2 Diffusion results

The main goals of this diffusion study were two: i) implement standardized procedures to acquire and analyze longitudinal multi-site diffusion 3T MRI data, and ii) evaluate the within and across-site across-session reproducibility of DTI-derived metrics typically used to characterize structural connectivity. The analysis was aimed at a total of 80 brains: 8 MRI sites, 5 subjects per site, 2 acquisitions per subjects (one test, one retest). The DTI-derived metrics included: fractional anisotropy (FA), mean diffusivity (MD,  $10^{-3} \text{ mm}^2/\text{s}$ ), parallel ( $\lambda_{\parallel}$ ,  $10^{-3} \text{ mm}^2/\text{s}$ ) and axial ( $\lambda_{\perp}$ ,  $10^{-3} \text{ mm}^2/\text{s}$ ) diffusivities. These metrics were evaluated and averaged for each subject and session in a number of gray and white matter ROIs taken from an atlas and considering relevance for MCI and AD studies. Four different analyses were used to characterize the across-session test-retest reliability on a single-subject basis: i) absolute differences relative to the mean in %, ii) intra class correlation (ICC), iii) coefficient of variation (CV), and iv) spatial reproducibility of the ROIs (Dice coefficients).

Preliminary quality assurance was done by inspecting each dataset for full brain coverage. We found that 6 DTI volumes had to be discarded from the analysis because of acquisition errors (partial brain coverage). Motion parameters estimated during the Eddy correction step were also inspected, indicating that, except for three sites, all maximum translations/rotations were below 1 mm/degrees (Table 15). Visual inspection of FA images showed a high qualitative similarity of results quality across sites (Fig 29).

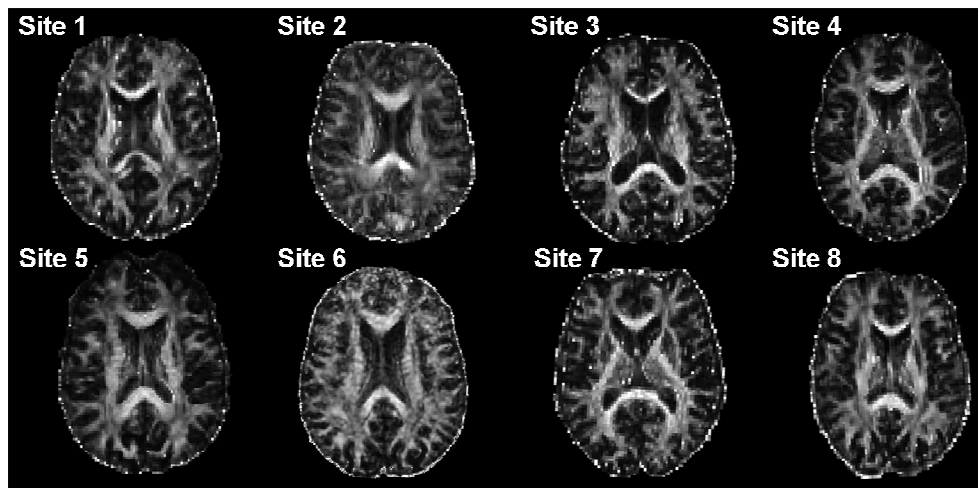


**Figure 29: Sample single-subject FA maps across different 3T MRI sites for qualitative comparison. See Table 2 for MRI sites characteristics.**

		DTI motion parameters							
		Site 1	Site 2	Site 3	Site 4	Site 5	Site 6	Site 7	Site 8
Max rotation (°)	test	0.78	0.94	0.82	0.83	0.93	0.62	0.78	0.76
	retest	0.90	0.73	1.02	0.91	0.69	0.60	2.13	1.31
Max translation (mm)	test	0.83	0.91	0.81	0.87	0.83	0.86	0.86	1.00
	retest	0.91	0.94	0.91	0.87	0.92	0.48	0.86	2.22

**Table 15. Head motion parameters across MRI sites. Maximum head rotations and translations across all subjects at each site.**

#### **4.4.2.1 Estimation of brain diffusion parameters across MRI sites**

Table 16 summarizes the group mean diffusion results averaged across test-retest session for each MRI sites. Values were consistent across sites and metrics and Kruskal-Wallis test for MRI site effect on the hemispheric diffusion indices did not show any significant effect.



a

		MRI Sites: diffusion estimates (FA and MD)							
Structures		Site 1	Site 2	Site 3	Site 4	Site 5	Site 6	Site 7	Site 8
cc_body	FA	0.577 ± 0.026	0.581 ± 0.018	0.580 ± 0.040	0.581 ± 0.036	0.574 ± 0.014	0.606 ± 0.027	0.514 ± 0.051	0.576 ± 0.028
	MD	0.937 ± 0.021	0.980 ± 0.070	0.886 ± 0.039	0.877 ± 0.065	0.893 ± 0.029	0.926 ± 0.029	0.955 ± 0.036	0.898 ± 0.031
cc_genu	FA	0.607 ± 0.025	0.585 ± 0.029	0.605 ± 0.046	0.595 ± 0.035	0.558 ± 0.017	0.635 ± 0.018	0.476 ± 0.020	0.583 ± 0.042
	MD	0.846 ± 0.050	0.814 ± 0.039	0.837 ± 0.041	0.886 ± 0.061	0.916 ± 0.024	0.917 ± 0.026	1.199 ± 0.039	0.860 ± 0.036
cc_spl	FA	0.639 ± 0.020	0.659 ± 0.034	0.652 ± 0.035	0.632 ± 0.024	0.662 ± 0.009	0.707 ± 0.014	0.656 ± 0.017	0.661 ± 0.033
	MD	0.962 ± 0.030	0.949 ± 0.063	0.899 ± 0.033	0.913 ± 0.064	0.892 ± 0.054	0.922 ± 0.032	0.971 ± 0.018	0.949 ± 0.047
crtsp_L	FA	0.483 ± 0.047	0.519 ± 0.033	0.490 ± 0.040	0.467 ± 0.057	0.520 ± 0.046	0.539 ± 0.055	0.525 ± 0.017	0.513 ± 0.030
	MD	0.905 ± 0.082	0.814 ± 0.057	0.839 ± 0.046	1.129 ± 0.229	0.828 ± 0.081	1.107 ± 0.570	0.897 ± 0.087	0.854 ± 0.070
crtsp_R	FA	0.500 ± 0.033	0.528 ± 0.039	0.469 ± 0.062	0.449 ± 0.045	0.504 ± 0.063	0.506 ± 0.082	0.557 ± 0.024	0.520 ± 0.030
	MD	0.864 ± 0.078	0.790 ± 0.048	0.871 ± 0.094	1.177 ± 0.154	0.820 ± 0.094	1.296 ± 0.706	0.830 ± 0.049	0.843 ± 0.039
ILF_L	FA	0.500 ± 0.023	0.493 ± 0.039	0.532 ± 0.034	0.545 ± 0.035	0.532 ± 0.026	0.549 ± 0.014	0.536 ± 0.032	0.493 ± 0.041
	MD	0.987 ± 0.072	0.875 ± 0.057	0.865 ± 0.065	0.859 ± 0.057	0.866 ± 0.053	0.944 ± 0.042	0.819 ± 0.027	0.932 ± 0.065
ILF_R	FA	0.519 ± 0.042	0.511 ± 0.031	0.524 ± 0.024	0.515 ± 0.017	0.514 ± 0.018	0.552 ± 0.028	0.477 ± 0.010	0.498 ± 0.065
	MD	0.912 ± 0.035	0.884 ± 0.041	0.900 ± 0.030	0.821 ± 0.039	0.835 ± 0.043	0.914 ± 0.018	0.862 ± 0.019	0.919 ± 0.086
SLF_L	FA	0.455 ± 0.023	0.427 ± 0.021	0.419 ± 0.026	0.429 ± 0.025	0.441 ± 0.014	0.478 ± 0.020	0.394 ± 0.013	0.425 ± 0.041
	MD	0.814 ± 0.030	0.853 ± 0.048	0.797 ± 0.069	0.771 ± 0.019	0.768 ± 0.022	0.808 ± 0.016	0.777 ± 0.039	0.792 ± 0.045
SLF_R	FA	0.459 ± 0.032	0.439 ± 0.021	0.434 ± 0.023	0.444 ± 0.029	0.455 ± 0.017	0.465 ± 0.024	0.418 ± 0.026	0.446 ± 0.049
	MD	0.815 ± 0.033	0.830 ± 0.039	0.805 ± 0.065	0.758 ± 0.021	0.762 ± 0.019	0.826 ± 0.017	0.808 ± 0.007	0.788 ± 0.062

b

Structures		MRI Sites: diffusion estimates ( $\lambda_{  }$ and $\lambda_{\perp}$ )							
		Site 1	Site 2	Site 3	Site 4	Site 5	Site 6	Site 7	Site 8
cc_body	$\lambda_{  }$	1.629 ± 0.033	1.705 ± 0.105	1.543 ± 0.037	1.532 ± 0.064	1.555 ± 0.040	1.664 ± 0.051	1.544 ± 0.038	1.565 ± 0.058
	$\lambda_{\perp}$	0.580 ± 0.033	0.617 ± 0.057	0.581 ± 0.057	0.549 ± 0.071	0.582 ± 0.029	0.557 ± 0.036	0.660 ± 0.064	0.585 ± 0.031
cc_genu	$\lambda_{  }$	1.500 ± 0.071	1.600 ± 0.038	1.478 ± 0.025	1.483 ± 0.052	1.569 ± 0.037	1.694 ± 0.061	1.778 ± 0.015	1.478 ± 0.037
	$\lambda_{\perp}$	0.519 ± 0.046	0.571 ± 0.047	0.520 ± 0.064	0.598 ± 0.068	0.590 ± 0.025	0.530 ± 0.021	0.911 ± 0.055	0.553 ± 0.050
cc_spl	$\lambda_{  }$	1.757 ± 0.031	1.757 ± 0.076	1.672 ± 0.044	1.650 ± 0.079	1.689 ± 0.087	1.821 ± 0.054	1.789 ± 0.041	1.767 ± 0.057
	$\lambda_{\perp}$	0.570 ± 0.034	0.554 ± 0.063	0.518 ± 0.050	0.544 ± 0.059	0.504 ± 0.040	0.492 ± 0.022	0.576 ± 0.026	0.542 ± 0.052
crtsp_L	$\lambda_{  }$	1.393 ± 0.064	1.300 ± 0.070	1.283 ± 0.047	1.583 ± 0.195	1.307 ± 0.075	1.639 ± 0.577	1.350 ± 0.109	1.371 ± 0.076
	$\lambda_{\perp}$	0.681 ± 0.097	0.572 ± 0.058	0.618 ± 0.054	0.902 ± 0.245	0.589 ± 0.088	0.853 ± 0.595	0.677 ± 0.080	0.597 ± 0.089
crtsp_R	$\lambda_{  }$	1.358 ± 0.118	1.276 ± 0.063	1.306 ± 0.072	1.612 ± 0.130	1.283 ± 0.100	1.851 ± 0.743	1.279 ± 0.087	1.357 ± 0.040
	$\lambda_{\perp}$	0.618 ± 0.063	0.548 ± 0.050	0.654 ± 0.110	0.961 ± 0.167	0.599 ± 0.107	1.038 ± 0.701	0.609 ± 0.042	0.586 ± 0.046
ILF_L	$\lambda_{  }$	1.527 ± 0.078	1.368 ± 0.072	1.401 ± 0.089	1.406 ± 0.064	1.400 ± 0.061	1.576 ± 0.075	1.339 ± 0.043	1.486 ± 0.076
	$\lambda_{\perp}$	0.716 ± 0.071	0.628 ± 0.058	0.597 ± 0.061	0.588 ± 0.057	0.601 ± 0.059	0.629 ± 0.028	0.559 ± 0.027	0.665 ± 0.069
ILF_R	$\lambda_{  }$	1.457 ± 0.063	1.401 ± 0.068	1.458 ± 0.049	1.314 ± 0.042	1.331 ± 0.054	1.535 ± 0.054	1.326 ± 0.018	1.453 ± 0.066
	$\lambda_{\perp}$	0.642 ± 0.044	0.625 ± 0.036	0.621 ± 0.032	0.575 ± 0.038	0.588 ± 0.042	0.604 ± 0.023	0.629 ± 0.019	0.652 ± 0.105
SLF_L	$\lambda_{  }$	1.234 ± 0.039	1.226 ± 0.044	1.154 ± 0.074	1.143 ± 0.046	1.145 ± 0.037	1.247 ± 0.034	1.170 ± 0.031	1.166 ± 0.041
	$\lambda_{\perp}$	0.604 ± 0.035	0.686 ± 0.051	0.619 ± 0.068	0.585 ± 0.020	0.577 ± 0.019	0.589 ± 0.019	0.627 ± 0.022	0.604 ± 0.055
SLF_R	$\lambda_{  }$	1.244 ± 0.038	1.211 ± 0.036	1.187 ± 0.070	1.140 ± 0.017	1.158 ± 0.034	1.262 ± 0.037	1.189 ± 0.026	1.187 ± 0.042
	$\lambda_{\perp}$	0.601 ± 0.044	0.638 ± 0.041	0.614 ± 0.063	0.567 ± 0.033	0.564 ± 0.019	0.608 ± 0.022	0.614 ± 0.034	0.586 ± 0.074

**Table 16: Diffusion parameters estimates across sites.** Within-site group means and standard deviation (across subjects and scanner sessions) of FA, MD ( $10^{-3} \text{ mm}^2/\text{s}$ ) (a),  $\lambda_{||}$  ( $10^{-3} \text{ mm}^2/\text{s}$ ) and  $\lambda_{\perp}$  ( $10^{-3} \text{ mm}^2/\text{s}$ ) (b). There are no significant MRI site effects (Kruskal-Wallis test,  $p < 0.01$ ). Abbreviations: cc\_body= body of the corpus callosum, cc\_genu= genu of the corpus callosum, cc\_spl= splenium of the corpus callosum, crtsp= corticospinal tract, ILF\_L= left inferior lateral fasciculus, ILF\_R= right inferior lateral fasciculus, SLF\_L= left superior lateral fasciculus, SLF\_R= right superior lateral fasciculus. See Table 2 for MRI sites characterization.

#### 4.4.2.1 Estimation of brain diffusion parameters reproducibility across MRI sites

The across-session test-retest reliability errors of the DTI indices are reported in Table 17, which shows for each structure and site, the mean absolute

reproducibility (%) across subjects. We found that the absolute reproducibility errors of FA, MD,  $\lambda_{||}$  and  $\lambda_{\perp}$  in white matter ROIs were highly consistent across structures, metrics and 3T MRI sites, and was mostly within the range 2-3%. A Kruskal-Wallis test for MRI site effect on the hemispheric regions showed a significant site effects ( $p < 0.01$ ) for 3 of the 9 regions considered: body (MD,  $p = 0.033$ ;  $\lambda_{\perp}$ ,  $p = 0.018$ ), splenium ( $\lambda_{||}$ ,  $p = 0.022$ ) and left superior lateral fasciculi (MD,  $p = 0.012$ ;  $\lambda_{\perp}$ ,  $p = 0.003$ ). Fig 30 summarized the reproducibility error of FA, MD,  $\lambda_{||}$  and  $\lambda_{\perp}$  for each site across the 9 white matter ROIs. No site effect was evident (Kruskal-Wallis test,  $p < 0.01$ ).

**a**

Structures		MRI Sites: diffusion reproducibility error (%) (FA and MD)							
		Site 1	Site 2	Site 3	Site 4	Site 5	Site 6	Site 7	Site 8
cc_body	FA	2.09 ± 1.10	2.84 ± 1.21	2.55 ± 1.89	1.17 ± 0.90	1.84 ± 1.63	2.43 ± 1.65	3.38 ± 1.89	0.72 ± 0.81
	MD	0.96 ± 0.76	5.89 ± 3.58	3.83 ± 0.99	3.99 ± 0.76	2.34 ± 1.07	1.99 ± 2.35	5.17 ± 0.27	2.54 ± 2.80
cc_genu	FA	0.89 ± 0.76	1.69 ± 0.74	2.72 ± 1.49	1.29 ± 1.01	1.25 ± 1.54	1.84 ± 1.44	3.63 ± 1.33	1.80 ± 0.82
	MD	1.59 ± 0.94	2.19 ± 1.66	3.55 ± 0.72	2.00 ± 2.40	1.51 ± 0.98	1.83 ± 0.99	3.49 ± 1.69	1.54 ± 1.58
cc_spl	FA	1.25 ± 0.85	4.40 ± 3.81	1.14 ± 1.13	2.09 ± 1.21	1.48 ± 1.00	1.07 ± 0.50	1.95 ± 1.45	1.34 ± 1.43
	MD	1.37 ± 1.14	7.23 ± 7.26	2.15 ± 1.15	1.65 ± 0.41	1.59 ± 0.80	1.71 ± 2.14	2.35 ± 3.19	0.59 ± 0.40
crtsp_L	FA	5.98 ± 4.16	4.07 ± 1.82	4.10 ± 4.87	6.26 ± 4.33	4.40 ± 2.43	8.87 ± 3.31	3.79 ± 0.18	3.86 ± 3.00
	MD	7.94 ± 10.25	4.81 ± 3.36	2.42 ± 2.68	14.85 ± 7.80	5.96 ± 5.28	11.55 ± 11.41	4.77 ± 2.30	3.33 ± 2.83
crtsp_R	FA	3.94 ± 2.94	7.99 ± 4.99	3.51 ± 2.40	5.86 ± 2.04	4.56 ± 4.61	3.73 ± 3.18	5.80 ± 1.83	4.93 ± 3.15
	MD	6.96 ± 4.42	6.72 ± 4.75	4.69 ± 4.02	6.37 ± 5.86	8.06 ± 6.13	8.36 ± 6.65	7.95 ± 8.53	3.78 ± 1.848
ILF_L	FA	1.32 ± 1.52	3.73 ± 2.88	2.74 ± 0.98	3.64 ± 1.88	5.06 ± 3.92	2.86 ± 0.74	3.47 ± 2.59	1.76 ± 1.885
	MD	3.41 ± 1.21	1.26 ± 1.04	5.03 ± 3.10	3.25 ± 3.79	1.71 ± 2.45	1.26 ± 1.59	5.06 ± 1.14	2.85 ± 1.37
ILF_R	FA	3.67 ± 2.83	3.60 ± 3.60	1.98 ± 1.92	2.12 ± 1.49	3.79 ± 2.82	2.43 ± 2.34	2.89 ± 2.18	4.19 ± 3.34
	MD	3.00 ± 2.81	4.68 ± 3.43	0.81 ± 0.84	1.15 ± 0.91	5.26 ± 7.93	1.17 ± 0.49	2.72 ± 3.47	2.08 ± 1.87
SLF_L	FA	1.16 ± 0.75	1.27 ± 0.77	4.83 ± 1.95	1.99 ± 1.16	1.21 ± 1.17	1.93 ± 1.34	1.58 ± 2.04	1.05 ± 0.52
	MD	0.57 ± 0.43	4.07 ± 2.21	3.60 ± 1.44	3.11 ± 1.01	1.41 ± 1.27	1.94 ± 0.78	2.27 ± 0.04	1.16 ± 1.25
SLF_R	FA	2.03 ± 1.13	4.39 ± 3.23	0.57 ± 0.88	2.81 ± 1.80	2.44 ± 2.08	2.73 ± 2.07	3.75 ± 3.67	1.42 ± 0.90
	MD	1.78 ± 0.50	5.01 ± 3.53	1.54 ± 1.02	0.78 ± 0.85	2.39 ± 3.92	1.80 ± 1.71	0.67 ± 0.57	1.49 ± 0.96

**b**

Structures		MRI Sites: diffusion reproducibility error (%) ( $\lambda$ II and $\lambda^{\perp}$ )							
		Site 1	Site 2	Site 3	Site 4	Site 5	Site 6	Site 7	Site 8
cc_body	All	1.31 ± 1.51	5.31 ± 3.14	2.62 ± 1.41	4.30 ± 1.50	2.73 ± 1.98	2.30 ± 2.41	3.64 ± 0.79	2.85 ± 2.42
	$\lambda^{\perp}$	1.76 ± 1.21	7.16 ± 4.82	5.46 ± 2.53	3.52 ± 1.00	1.81 ± 1.55	3.93 ± 1.24	6.91 ± 0.11	2.18 ± 3.01
cc_genu	All	1.77 ± 0.25	2.60 ± 1.28	1.91 ± 1.49	2.38 ± 2.14	2.02 ± 1.14	0.84 ± 0.67	1.29 ± 0.18	1.75 ± 2.03
	$\lambda^{\perp}$	2.39 ± 0.69	2.63 ± 1.90	5.36 ± 1.20	2.02 ± 2.56	1.12 ± 1.26	3.64 ± 2.34	5.57 ± 3.03	1.76 ± 0.76
cc_spl	All	1.86 ± 1.40	5.23 ± 4.02	1.23 ± 1.13	2.29 ± 1.55	1.81 ± 0.97	1.57 ± 1.80	1.90 ± 1.65	0.81 ± 0.55
	$\lambda^{\perp}$	1.33 ± 0.93	8.43 ± 11.34	3.26 ± 2.01	1.83 ± 1.44	1.99 ± 1.58	1.37 ± 0.83	4.27 ± 3.56	1.73 ± 1.28
crtsp_L	All	5.90 ± 6.45	3.17 ± 2.23	3.76 ± 2.48	9.93 ± 6.32	3.89 ± 3.90	10.37 ± 10.12	4.00 ± 4.21	2.17 ± 2.12
	$\lambda^{\perp}$	11.89 ± 13.80	7.26 ± 3.94	3.25 ± 3.34	19.18 ± 9.24	8.50 ± 6.78	14.69 ± 12.32	5.49 ± 0.09	4.88 ± 4.24
crtsp_R	All	6.64 ± 4.17	3.66 ± 2.23	3.41 ± 3.02	4.30 ± 3.72	5.95 ± 3.23	5.97 ± 5.39	7.18 ± 5.13	4.30 ± 2.33
	$\lambda^{\perp}$	8.08 ± 6.81	10.85 ± 8.20	5.85 ± 5.44	8.90 ± 7.67	10.31 ± 9.82	12.54 ± 8.03	8.68 ± 11.82	4.80 ± 1.90
ILF_L	All	2.86 ± 0.92	2.01 ± 2.57	4.33 ± 3.22	3.86 ± 2.96	2.20 ± 1.58	2.06 ± 1.83	5.42 ± 1.35	2.37 ± 1.17
	$\lambda^{\perp}$	4.02 ± 1.82	1.11 ± 0.69	5.68 ± 3.37	4.25 ± 4.09	4.26 ± 3.00	2.45 ± 0.84	4.74 ± 1.12	3.41 ± 3.06
ILF_R	All	2.95 ± 2.67	3.64 ± 4.11	0.82 ± 0.69	1.53 ± 1.01	4.96 ± 4.60	1.27 ± 0.81	1.85 ± 2.02	3.51 ± 2.51
	$\lambda^{\perp}$	3.91 ± 3.47	5.87 ± 3.73	1.26 ± 1.39	2.04 ± 1.44	6.34 ± 11.41	2.64 ± 2.29	3.63 ± 5.00	2.76 ± 1.49
SLF_L	All	0.97 ± 0.40	3.52 ± 2.00	1.73 ± 0.79	3.87 ± 1.10	1.72 ± 1.40	1.89 ± 1.63	1.00 ± 1.04	1.53 ± 1.03
	$\lambda^{\perp}$	0.62 ± 0.30	4.63 ± 2.41	5.36 ± 2.70	2.36 ± 1.17	1.46 ± 1.05	1.96 ± 1.16	3.38 ± 0.83	1.07 ± 1.33
SLF_R	All	2.46 ± 1.02	3.66 ± 2.48	1.60 ± 1.15	1.13 ± 0.82	2.75 ± 2.80	1.92 ± 2.07	1.83 ± 2.39	1.48 ± 1.31
	$\lambda^{\perp}$	1.08 ± 1.18	6.30 ± 4.61	1.48 ± 1.07	2.06 ± 0.73	3.05 ± 4.54	2.33 ± 2.16	0.75 ± 0.50	1.75 ± 1.36

**Table 17: Effects of MRI site on diffusion reproducibility.** Within-site group mean reproducibility error and standard deviation (across subjects and scanner sessions). The abbreviations are the same of Table 16. See Table 2 for MRI sites characterization.

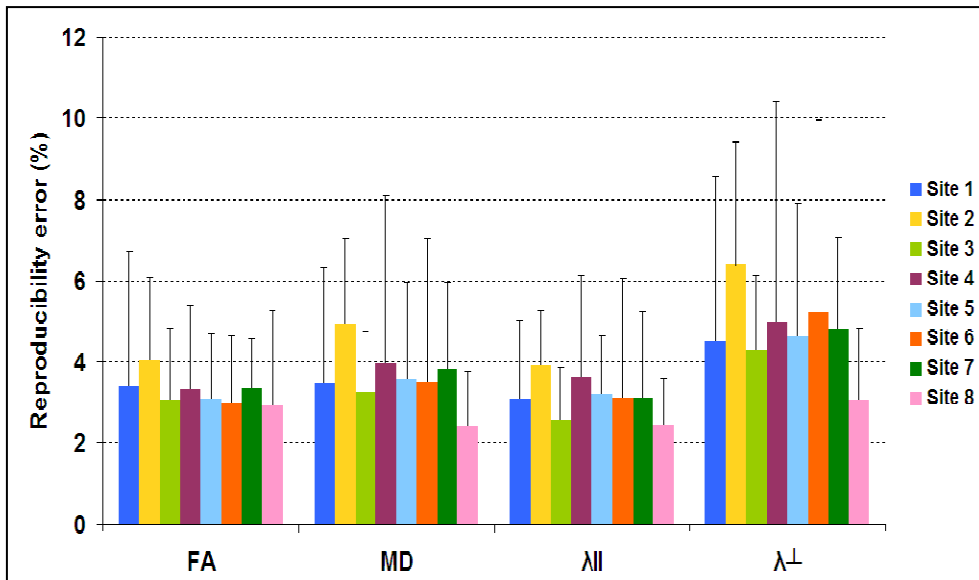


**Figure 30: Summary of MRI site effects on diffusion reproducibility.** Within-site group mean reproducibility error (across-session test-retest) and standard deviation (across subjects, structures and sessions). There are no significant MRI site effects (Kruskal-Wallis test,  $p < 0.01$ ). See Table 2 for MRI sites characterization.

#### 4.4.2.2 Estimation of CV and ICC: effects of MRI sites

In addition to the absolute reproducibility error, the ICC and CV were used to characterize the reliability of the DTI estimates. Table 18 shows the mean ICC and the mean CV across sites and structures. Values were consistent across sites and metrics. There were no significant MRI site effects (Kruskal-Wallis test,  $p < 0.01$ ) for ICC while for CV a site effect was evident for MD (Kruskal-Wallis test,  $p = 0.006$ ),  $\lambda_{II}$  ( $p = 0.023$ ) and  $\lambda_{\perp}$  ( $p = 0.016$ ).

DTI Index	ICC and CV across MRI sites								
		Site 1	Site 2	Site 3	Site 4	Site 5	Site 6	Site 7	Site 8
FA	ICC	0.98 ± 0.02	0.98 ± 0.01	0.99 ± 0.01	0.97 ± 0.04	0.98 ± 0.0	0.97 ± 0.03	0.97 ± 0.02	0.99 ± 0.01
	CV	1.76 ± 1.79	2.67 ± 2.28	1.90 ± 1.68	2.14 ± 1.78	2.05 ± 1.96	2.02 ± 1.71	2.37 ± 1.37	1.66 ± 1.68
MD	ICC	0.99 ± 0.01	0.98 ± 0.02	0.98 ± 0.01	0.99 ± 0.01	0.99 ± 0.0	0.99 ± 0.00	0.98 ± 0.03	0.99 ± 0.01
	CV	2.17 ± 3.07	3.29 ± 2.78	2.17 ± 1.65	2.92 ± 3.71	2.37 ± 3.12	2.48 ± 3.89	2.71 ± 2.29	1.52 ± 1.32
All	ICC	0.98 ± 0.02	0.81 ± 0.25	0.90 ± 0.19	0.93 ± 0.10	0.89 ± 0.0	0.90 ± 0.11	0.95 ± 0.06	0.94 ± 0.04
	CV	2.10 ± 2.28	2.58 ± 1.94	1.88 ± 1.48	2.84 ± 2.52	2.20 ± 2.00	2.22 ± 3.35	2.21 ± 1.96	1.63 ± 1.39
$\lambda^{\perp}$	ICC	0.96 ± 0.04	0.90 ± 0.11	0.92 ± 0.07	0.91 ± 0.14	0.90 ± 0.0	0.92 ± 0.08	0.95 ± 0.06	0.97 ± 0.02
	CV	2.76 ± 4.23	4.26 ± 4.09	2.92 ± 2.22	3.63 ± 4.74	3.05 ± 4.38	3.58 ± 4.67	3.41 ± 2.82	1.90 ± 1.73

**Table 18: ICC and CV of WM ROIs.** Within-site group mean ICC and CV and standard deviation of FA, MD,  $\lambda^{\perp}$  (across subjects, structures and scanner sessions). See Table 2 for MRI sites characterization.

#### 4.4.2.3 Estimation of spatial reproducibility of atlas-based ROIs: effects of MRI sites

The across-session test-retest spatial overlaps are reported in Table 19, which shows for each site and ROI the mean Dice coefficient of spatial overlap averaged across subjects. A Kruskal-Wallis test for MRI site effect on the hemispheric volumes showed a significant site effects ( $p < 0.01$ ) for 3 of the 9 regions considered: splenium, right corticospinal tract and left inferior lateral fasciculi.

ROI	MRI Sites: Dice coefficients for spatial overlap							
	Site 1	Site 2	Site 3	Site 4	Site 5	Site 6	Site 7	Site 8
cc_body	0.92 ± 0.02	0.88 ± 0.05	0.89 ± 0.03	0.92 ± 0.01	0.92 ± 0.01	0.91 ± 0.01	0.93 ± 0.05	0.92 ± 0.02
cc_genu	0.90 ± 0.02	0.90 ± 0.03	0.89 ± 0.02	0.91 ± 0.02	0.91 ± 0.02	0.91 ± 0.02	0.78 ± 0.09	0.91 ± 0.01
cc_spl	0.92 ± 0.01	0.91 ± 0.03	0.90 ± 0.04	0.94 ± 0.01	0.94 ± 0.01	0.94 ± 0.02	0.97 ± 0.06	0.94 ± 0.01
crtsp_L	0.79 ± 0.02	0.82 ± 0.05	0.83 ± 0.11	0.71 ± 0.06	0.77 ± 0.09	0.74 ± 0.13	0.74 ± 0.06	0.80 ± 0.07
crtsp_R	0.80 ± 0.05	0.82 ± 0.03	0.80 ± 0.04	0.69 ± 0.12	0.79 ± 0.12	0.71 ± 0.06	0.70 ± 0.07	0.81 ± 0.03
ILF_L	0.81 ± 0.07	0.84 ± 0.01	0.82 ± 0.05	0.88 ± 0.02	0.87 ± 0.05	0.87 ± 0.03	0.77 ± 0.08	0.88 ± 0.02
ILF_R	0.86 ± 0.03	0.85 ± 0.05	0.85 ± 0.04	0.86 ± 0.03	0.86 ± 0.04	0.85 ± 0.03	0.79 ± 0.03	0.87 ± 0.04
SLF_L	0.87 ± 0.05	0.83 ± 0.05	0.85 ± 0.06	0.88 ± 0.03	0.88 ± 0.04	0.89 ± 0.03	0.74 ± 0.08	0.90 ± 0.03
SLF_R	0.89 ± 0.03	0.84 ± 0.05	0.87 ± 0.05	0.89 ± 0.02	0.89 ± 0.03	0.89 ± 0.01	0.79 ± 0.09	0.88 ± 0.03
All	0.86 ± 0.05	0.85 ± 0.03	0.86 ± 0.03	0.85 ± 0.09	0.87 ± 0.05	0.86 ± 0.07	0.80 ± 0.09	0.88 ± 0.05

**Table 19: Spatial reproducibility of WM ROI.** Within-site group mean volume overlap (DICE coefficient) and standard deviation (across subjects and scanner sessions). The last row shows the spatial reproducibility for each site. The abbreviations are the same of Table 16. See Table 2 for MRI sites characterization.

## **4.5 Discussion**

### **4.5.1 Brain morphometry**

We show for the first time in a group of eight different 3T MRI scanners (Siemens, Philips, GE) that human subcortical volume and cortical thickness estimates derived from brain structural MRI data are remarkably reproducible when using the publicly available FreeSurfer automated segmentation tool. Specifically, using a group of healthy older (mean age  $63.2 \pm 8.1$  years,  $n=40$  where 5 sub/scanner) we examined how the subcortical, ventricular and intracranial volumes as well as cortical thickness test-retest reproducibility are affected by scan session, segmentation analyses and vendor. We demonstrate that longitudinal FreeSurfer processing stream improve reliability relative to the cross-sectional segmentation stream, both within and across MRI sites.

The segmentation errors reported in this work represent the best estimate we can give for the error of the method under the reported measurement conditions. The main factors that introduce errors in the final segmentation results are image quality factors (signal-to-noise ratio and contrast-to-noise ratio) and brain anatomical variability relative to the probabilistic atlas. These factors are intermingled. Realistic brain anatomical simulations with pre-defined characteristics for subcortical structures and their spatial arrangements could be attempted to separate the contribution of segmentation errors from image quality and segmentation atlas factors. These issues are important but are beyond the scope of this manuscript. The closest to a ground-truth that can be currently used to assess the accuracy of the FreeSurfer segmentation method is the comparison with manual segmentations by a neuroanatomist, as validated in Fischl et al. 2002 [187].

The segmentation results of volumes (table 3) and thicknesses (table 6) are comparable with previously reported results (The Internet Brain Volume Database, <http://www.cma.mgh.harvard.edu/ibvd/>). For most structures, there's a fairly wide range of estimates of normal volume, and ours are within the typical range. Overall, there was consistent reliability of volumes for all regions considered across sites and vendors (table 4). For the hippocampus, thalamus, caudate, putamen, lateral ventricles and intracranial volumes, cross-sectional reproducibility error was less than 6%. As expected, higher variability has been revealed for smaller structures such as amygdale and pallidum (under 11.2%). Longitudinal pipeline, reducing the biological variabilities using the subject as his own control, significantly decreased reproducibility error in all regions. For bigger structure was less than 3% while for smaller regions was less than 6%. Our across session test-retest reproducibility are comparable with previously within session reproducibility results performed using a Siemens TIM Trio scanner [194]. The spatial reproducibility results showed constant and high spatial consistency of the segmentation volumes already using the cross-sectional stream (mean Dice coefficient range across sites from 0.84 to 0.88) (Table 5), improved with the longitudinal pipeline (mean Dice coefficient range across sites from 0.90 to 0.95). Spatial overlap results are also in good agreement with a previous within session study [194].

The thickness reproducibility results were consistent for all regions across sites and vendors and were less than 5.51% (table 7). Unexpectedly, no significant

difference between the thickness reproducibility errors from the two analyses was found. This is in contrast to previous reported findings [194, 207] where a reduction of the thickness measurements variability was demonstrated. Several study differences may explain this discrepancy. Han et al used a lower field strength and considered the overall mean thickness measurement error while we analyzed single gyrus. Although Reuter et al used a 3T scanner, factors that could account on results differences are related to data collection (sample size and MPAGE sequence) and to data analysis (they measured within session reproducibility). Indeed, their test-retest data derived from a set consisting of 115 controls scanned in the same site versus our 40, about which 5 subjects for each site. Moreover, within session acquisition is less affected by source of variance such as subject repositioning and magnetic field instability or drift.

As recently shown, in vivo local structural 3D shapes characterization assessed differences between patients with AD and normal elderly individual [210, 211]. Hence, combining both volume and shape metrics might improve the power of detecting cross-sectional differences across populations or longitudinal changes. An important extension of the reproducibility study here presented would be to examine the reproducibility of shape metrics.

#### 4.5.2 Brain diffusion

In this study we investigated how the test-retest quantitative estimation and reproducibility errors of FA, MD,  $\lambda_{II}$  and  $\lambda_{\perp}$  derived from DTI data in a group of healthy older (mean age  $63.2 \pm 8.1$  years,  $n=40$  where 5 sub/scanner) are affected by 3T MRI scanners (Siemens, Philips, GE). As mentioned in the introduction, most multi-site DTI reproducibility studies have been performed at 1.5T [212-215], except for a few studies that used either limited number of MRI sites [200] or dedicated acquisitions with several averaged acquisitions [203]. Our reproducibility analysis was focused in different ROIs relevant to the study of neurodegenerative diseases like MCI and AD [216]: body, genu, splenium of the corpus callosum, corticospinal tract (left/right), inferior lateral fasciculus (left/right), superior lateral fasciculus (left/right). The goal was to evaluate and standardized an automatic procedure for the quantification of DTI indices which gave reproducibility results similarly to manually drawn ROIs studies. Fully automated procedures which avoid manual drawing of ROIs have the advantage of not requiring the presence of high inter- and intra-rater coefficient of variation to guarantee DTI parameters reliability. On the other hand, automated methods may be susceptible to partial volume effects at the edge of the anatomical structures.

All DTI-derived metrics obtained from our acquisitions and analysis protocol (FA, MD,  $\lambda_{\perp}$  and  $\lambda_{II}$ ) were found consistent across MRI sites (Table 15a-b) and were comparable with previously reported DTI studies on healthy subjects of the same age [217, 218]. Overall, we found considerable consistency and good test-retest across session reproducibility of FA, MD,  $\lambda_{II}$  and  $\lambda_{\perp}$  metrics across structures and 3T scanners (table 16a-b and Fig 30). The absolute reproducibility errors of FA and MD in white matter ROIs were mostly within the range 2-3%, except for corticospinal tracts where the reproducibility error reached 7.99% for FA and 14.95% for MD. Other 3T reproducibility studies on corpus callosum reported FA errors in the same range [200, 201]. Also CV in the corpus callosum was in good agreement with previous 3T [200, 201] and lower relative to 1.5T studies [212, 213]. Besides corpus callosum, the CV of the other structures, excluding MD,  $\lambda_{II}$



and  $\lambda^{\perp}$  of corticospinal tracts, were below 10% which is desirable for biological variables related to imaging [219]. The ICC for most of the metrics was above 0.89 with lower values for  $\lambda^{\perp}$ . ICC is more restrictive as reproducibility test and should be above 0.80 [219]. As in the multi-site 3T study (two identical GE scanners) of Vollmar et al, we detected lower reproducibility in smaller ROIs (i.e., corticospinal tracts) than in bigger ones (i.e., corpus callosum). Finally, comparisons among the four diffusion indices showed an higher reproducibility across different brain areas for FA and MD rather than axial or radial diffusivity (Table 16b and Fig 30). These parameters may be sensitive to scanner instability or to other systematic source of error such as body hydration or temperature of the subjects [219]. The spatial reproducibility was consistent across MRI sites. Again, the lower spatial overlap was detected in smaller tracts (i.e., corticospinal tracts), more sensitive to noise, and where fibers of different and crossing orientations were present (i.e., superior lateral fasciculi). This is due to an intrinsic limitation of the DTI technique where imaging of multiple fiber orientation in a single voxel is not possible. Diffusion Spectrum Imaging (DSI), a recent development of MRI, may overcome this problem.

Extension of this work include understand possible sources of variability as well as further evaluation of reproducibility measures in gray matter, such as in the hippocampus.

#### **4.5.3 Limits of the study**

The major limit of this morphometric and diffusion study is the number of subject per site, an high number of subjects allow to minimize biases in the results. Besides, the volunteers are not the same for all sites including in our study biological variables due to obvious individual differences of the subjects. The optimal condition to make a test-retest reproducibility study should be organize a single group of healthy volunteers able to travel to the participating sites across the different countries.

#### **4.6 Conclusions and future prospects**

Reliability of subcortical, ventricular and intracranial volumes as well as cortical thickness was high and unaffected by scanner of different vendors. Using the longitudinal stream of Freesurfer we improve the volume reproducibility for intra- and inter-site scanning achieving an averaged reproducibility errors for each site less than 4%.

A multi-site 3T MRI protocol for brain DTI analysis was implemented in eight sites covering four countries. Our protocol considered single DTI acquisitions (no averages, approximately 5 min acquisitions each) and 8 different sites covering the most common clinical MRI vendors in Europe (Siemens, Philips, GE), both using old and very modern equipment. We found that the across-session test-retest reproducibility was comparable to that reported by other studies which used either low number of MRI sites or longer acquisitions.

All these metrics will be assessed in the MCI longitudinal study already started in order to identify imaging markers to predict the conversion of MCI to AD and to map the disease progression from its earlier stages.

Besides, being our morphometry and diffusion study an extension to the literature, suggests that the multi-site acquisition and analysis protocol used allows for reducing the number of subject that a single-site would need to detect a specific effect size by roughly the number of sites.

## 5 ACKNOWLEDGEMENTS

The research leading to this thesis has received funding from the European Community's Seventh Framework Programme (FP7/2007-2013) for the Innovative Medicine Initiative under Grant Agreement n°115009.

Thanks to PharmaCOG fundings for allowing me to work on these interesting topics.

I wish to express my sincere thanks to Giovanni Frisoni and Gianluigi Forloni, for providing me with all the necessary facilities.

I am grateful to Claudia Balducci and Jorge Jovicich for their irreplaceable guidance and unceasing encouragements.

I also thank Alessandra Paladini, Edoardo Micotti, Marco Lorenzi and Daniele Tolomeo for their help and support.

I am also grateful to my tutors Luisa Ottobrini and Mario Clerici for their precious time.

I finally thanks all my colleagues and friends for their support and (mainly) patience and who, directly or indirectly, help me to arrive at the end of this adventure.

## 6 LIST OF TABLES AND FIGURES

### **Figure 1. Hypothetical model of dynamic biomarkers in human AD (a) [13] and pathological AD progression in the most frequently used mice (b).**

Models of amyloidosis are created by deploying one, or a combination of, genes that have been found mutated in Familiar AD subjects (such as APP and PS1). These mice show structural, functional and biochemical alterations similarly to the human pre-clinical stage of AD pathology. Moreover, as for human, mouse deficits increase with age. All APP and/or PS1 Tg mouse models do not reproduce tangles. Tau pathology can be replicated in mice using modifications in the sequence of tau protein discovered in the familiar form of Frontotemporal Dementia with parkinsonism linked to chromosome 17 and Tau Tg mice are characterized by tangles in absence of A $\beta$ . The triple transgenic mouse model, carrying mutation in APP, PS1 and Tau (3xTg) better reproduces the signature lesions of AD as it develops both A $\beta$  and tangles.

**Figure 2. Structural markers in humans and mice.** In humans, grey matter loss in regions such as hippocampus (hp), cortices (ctx) and whole brain (WB) is useful for defining the AD pathology and tracking its progression. The brain morphological alteration of Tg mice are linked with neurodevelopmental rather than neurodegenerative factors. Indeed, each Tg has a specific structural alteration signature and are described one by one. Volume decrease and increase are represented in red and blue colours respectively while no differences between Tg and controls are illustrated in green. Continuous line represents whole brain (WB), dotted line only posterior brain. The only mouse model exhibiting hippocampal volume decrease and deficits in cortical volume detected using MRI is the Inducible APP<sup>swe</sup>/Ind, where pathology develops when the brain has reached fully maturity.

**Figure 3. Functional and metabolic markers of preclinical AD in humans and homologous markers in Tg mice.** Neuronal functionality is compromised many years before the appearance of clinical symptoms. Human studies found progressive functional impairment in the hippocampus (hp), posterior cingulate cortex (PCC), entorhinal cortex (ent) and temporo-parietal cortex (TP) of AD patients. The same areas were investigated in transgenic mice.

Top: Functional markers of preclinical AD in humans. Middle: Mice strains where functional markers homologous to humans have been identified (e.g. metabolic deficits in the hippocampus of J20 and 3xTg mice). Bottom: Mice strains where the same markers have been evaluated giving opposite results in comparison with humans. Markers decrease and increase are represented with red and blue colours respectively.

**Fig 4.** Some examples of sagittal (first row and bottom left) and coronal (second row middle and right) images of a young WT are shown with overlay of the masks used for the manual volume segmentation. Abbreviations: Cau-Put= caudate-putamen, Hp= hippocampus, OB= olfactory bulb, ctx= cortex (except the frontal), Vent= lateral, third and fourth ventricles, WB= whole brain, ICV= intracranial volume.

**Fig 5.** Examples of coronal color-coded images of a young WT are shown with overlay overlaid of the masks used for the manual diffusion quantification (black background) and 3D masks visualization (grey background). Abbreviations: cc= corpus callosum, ac= anterior commissure, cc= corpus callosum, cp= cerebral peduncle, ec= external capsule, fi= fimbria, int= internal capsule, Cau-Put=

caudate-putamen, hp= hippocampus, OB= olfactory bulb, Frontal ctx= frontal cortex, Thal= thalamus, PIR= piriform cortex.

**Fig 6. Entorhinal cortex (ERC) thickness definition shown on a coronal image of a WT mouse.** Abbreviation: rf = rhinal fissure.

**Fig 7. Comparison between TASTPM and WT normalized volumes across structures.** Within-site group means and standard deviation (across mice and hemispheres) of volumes derived from the manual segmentation. Axis y reported square root values. Two-way ANOVA, \* $p < .05$ ; \*\* $p < .01$ ; \*\*\* $p < .001$  after Hochberg's correction. Interaction p-values were also shown. The abbreviations were the same of Table 3.

**Fig 8. Representative T2-weighted images, FA maps and colour-coded FA from one coronal slice of young TASTPM and age-matched control.**

**Fig 9. Automated FA and  $\lambda^\perp$  maps comparisons between older TASTPM and age-matched controls.** Coronal brain images overlaid with the skeleton (green) and with the TBSS results. Data showed significantly ( $p < .05$ ) lower (red-yellow) FA and higher (light-blue)  $\lambda^\perp$  values in external capsule, corpus callosum, fimbria and cerebral peduncle of TASTPM.

**Fig 10. DTI indices in the anterior commissure (ac) and corpus callosum (cc) of TASTPM and age-matched WT.** Two-way ANOVA, \* $p < .05$ ; \*\* $p < .01$ ; \*\*\* $p < .001$  after Hochberg's correction. Interaction p-values are also shown.

**Fig 11. A representative comparison of amyloid load among older WT and different ages of TASTPM.** Sagittal slices were immunostained with the 6E10 antibody. TASTPM Tg mice display A $\beta$  deposits which became visible at 9 months and increased with age. Even if the majority of the amyloid burdens was in the grey matter, deposits in white matter were clearly evident (magnification 4x; scale bar, 250  $\mu$ m). Abbreviations: Cau-Put= caudate-putamen, Hp= hippocampus, ctx= cortex, cc= corpus callosum, Thal= thalamus.

**Fig 12. A representative comparison of neuroinflammation among older WT and different ages of TASTPM.** Sagittal slices were immunostained with Cd11b (a) and GFAP (b) antibodies. Microglial (arrow) and astrocytes (arrowhead) activation were observed when amyloid was present (magnification 4x; scale bar, 250  $\mu$ m). The abbreviations are the same of Fig 11.

**Fig 13. A representative comparison of myelinated axons among older WT and different ages of TASTPM.** Sagittal slices were stained with Gold chloride. A progressive white matter disorganization starting at 13 months is observable in TASTPM Tg mice (magnification 4x; scale bar, 250  $\mu$ m). The abbreviations are the same of Fig 11.

**Fig 14. Comparison between TauPS2APP and WT normalized volume estimations across structures.** Within-site group means and standard deviation (across mice and hemispheres) volumes derived from the manual segmentation. Two-way ANOVA, \* $p < .05$ ; \*\* $p < .01$ ; \*\*\* $p < .001$  after Hochberg's correction. Interaction p-values were also shown. The abbreviations were the same of Table 3.

**Fig 15. A representative comparison of amyloid load among older mice.** Sagittal slices were immunostained with the 6E10 antibody. A $\beta$  deposits can be seen in corpus callosum, hippocampus, cortex, caudate-putamen and, to a lesser extent, in the thalamus (magnification 4x; scale bar, 250  $\mu$ m). The abbreviations are the same of Fig 11.

**Fig 16. A representative comparison of neuroinflammation among older mice.** Sagittal slices were immunostained with Cd11b (a) and GFAP (b) antibodies. Only

older TauPS2APP exhibited glial (arrow) and astrocytes (arrowhead) activation (magnification 4x; scale bar, 250  $\mu$ m). The abbreviations are the same of Fig 11.

**Fig 17. A representative comparison of myelinated axons among older mice.** Sagittal slices were stained with Gold chloride. Any qualitative difference between TauPS2APP and WT can be appreciated (magnification 4x; scale bar, 250  $\mu$ m). The abbreviations are the same of Fig 11.

**Fig 18. Comparison between PDAPP and WT normalized volume estimations across structures.** Within-site group means and standard deviation (across mice and hemispheres) of volumes derived from the manual segmentation. Two-way ANOVA, \* $p < .05$ ; \*\* $p < .01$ ; \*\*\* $p < .001$  after Hochberg's correction. Interaction p-values were also shown. The abbreviations were the same of Table 3.

**Fig 19. DTI indices in the corpus callosum (cc) and external capsule (ec) of PDAPP and age-matched WT.** Two-way ANOVA, \* $p < .05$ ; \*\* $p < .01$ ; \*\*\* $p < .001$  after Hochberg's correction. Interaction p-values were also shown.

**Fig 20. A representative comparison of amyloid load among older WT and different ages of PDAPP.** Sagittal slices were immunostained with the 6E10 antibody. Few A $\beta$  deposits can be seen only in the hippocampus of older PDAPP (magnification 4x; scale bar, 250  $\mu$ m). The abbreviations are the same of Fig 11.

**Fig 21. A representative comparison of neuroinflammation among older WT and different ages of PDAPP.** Sagittal slices were immunostained with Cd11b (a) and GFAP (b) antibodies. No qualitative difference between TauPS2APP and WT can be appreciated (magnification 4x; scale bar, 250  $\mu$ m). The abbreviations are the same of Fig 11.

**Fig 22. A representative comparison of myelinated axons among older WT and different ages of PDAPP.** Sagittal slices were stained with Gold chloride. No qualitative difference between PDAPP and WT can be appreciated (magnification 4x; scale bar, 250  $\mu$ m). The abbreviations are the same of Fig 11.

**Fig 23. Examples of b0 image of a healthy volunteer overlaid with the atlas-based masks used for the automatic diffusion quantification.** Abbreviations: cc\_body= body of the corpus callosum, cc\_genu= genu of the corpus callosum, cc\_spl= splenium of the corpus callosum, crtsp= corticospinal tract, ILF= inferior lateral fasciculus, SLF= superior lateral fasciculus.

**Figure 24: Sample MPAGE images and Freesurfer segmentation results across different 3T MRI sites for qualitative comparison.** Abbreviations: Hp= hippocampus, Amy= amygdala, Cau= caudate, Put= putamen, Pal= pallidum, Thal= thalamus, Lat= lateral ventricle, Ctx= cerebral cortex. See Table 2 for MRI sites characteristics.

**Figure 25: Sample distribution of cross-sectional (CS) and longitudinal (LS) volume reproducibility results (Site 2) in hippocampus (Hp) and amygdala (Amy):** Bland-Altman plots showing volume difference versus volume mean (two single MPAGE acquisitions per session, subjects,  $n=5$ ). For each brain hemisphere (left: red crosses, right: blue circles) the mean volume difference (solid horizontal line) and the limits of agreement ( $\pm 2$  standard deviations, interrupted horizontal lines) are shown. For reference, zero volume difference is shown as a black dotted line.

**Figure 26: Across-session test-retest reproducibility errors of hippocampus and amygdala volume estimates, effects of MRI site and processing stream.** Reproducibility errors from the longitudinal and cross-sectional analysis for each

one of the eight 3T MRI sites, with their respective within-site standard deviations. Data derived from Table 11.

**Figure 27: Sample distribution of cross-sectional (CS) and longitudinal (LG) thickness reproducibility results (Site 2) in supramarginal gyrus (Supra) and precuneus (Prec):** Bland-Altman plots showing thickness difference versus thickness mean (two single MPRAGE acquisitions per session, subjects, n=5). For each brain hemisphere (left: red crosses, right: blue circles) the mean volume difference (solid horizontal line) and the limits of agreement ( $\pm 2$  standard deviations, interrupted horizontal lines) are shown. For reference, zero volume difference is shown as a black dotted line.

**Figure 28: Across-session test-retest reproducibility errors of supramarginal gyrus and precuneus thickness estimates, effects of MRI site and processing stream.** Reproducibility errors from the longitudinal and cross-sectional analysis for each one of the eight 3T MRI sites, with their respective within-site standard deviations. Data derived from Table 14.

**Figure 29: Sample single-subject FA maps across different 3T MRI sites for qualitative comparison. See Table 2 for MRI sites characteristics.**

**Figure 30: Summary of MRI site effects on diffusion reproducibility.** Within-site group mean reproducibility error (across-session test-retest) and standard deviation (across subjects, structures and sessions). There are no significant MRI site effects (Kruskal-Wallis test,  $p < 0.01$ ). See Table 2 for MRI sites characterization.

**Table 1. Most frequently used mice models of amyloidosis.** PDGF $\beta$  (platelet-derived growth factor  $\beta$ -chain) and PrP (prion protein) result in a transgene expression inside and outside of the central nervous system. Thy-1 (thymocyte differentiation antigen 1), HMG-CoA reductase (3 hydroxy-3-methylglutaryl-coenzyme A reductase) and NSE (neuron-specific enolase) are neuronal specific.

**Table 2.** List of the transgenic mice and their respective controls included in this study, specified by animals per age, gender and study design. Abbreviations: CS= cross-sectional; LG= longitudinal.

**Table 3. Comparison between TASTPM and WT volume and thickness estimations.** Within-site group means and standard deviation (across mice and hemispheres) of volumes and thickness obtained from the manual segmentation. The ERC statistics refer to two-way ANOVA, \*\* $p < .01$ ; \*\*\* $p < .001$  after Hochberg's correction. Abbreviations: Cau-Put= caudate-putamen, Hp= hippocampus, OB= olfactory bulb, Fron ctx= frontal cortex, ctx= rest of the cortex, Vent= lateral, third and fourth ventricles, WB= whole brain, ICV= intracranial volume, ERC= entorhinal cortex.

**Table 4. DTI indices of the white (a, b) and grey (c) regions of interest.** MD,  $\lambda_{||}$  and  $\lambda_{\perp}$  are expressed as  $10^{-3} \text{ mm}^2/\text{s}$ . Two-way ANOVA, \* $p < .05$ ; \*\* $p < .01$ ; \*\*\* $p < .001$  after Hochberg's correction. Interaction p-values are shown in the transgene x age column. Abbreviations: FA= fractional anisotropy, MD= mean diffusivity,  $\lambda_{||}$ = axial diffusivity,  $\lambda_{\perp}$ = radial diffusivity, cc= corpus callosum, ac= anterior commissure, cp= cerebral peduncle, cing= cingulum, int= internal capsule, ec= external capsule, fi= fimbria, Cau-Put= caudate-putamen, Hp= hippocampus, OB= olfactory bulb, Thal= thalamus, ns= non-significant.

**Table 5. Comparison between TauPS2APP and WT volume estimations across structures.** Within-site group means and standard deviation (across mice and hemispheres) of volumes and thickness derived from the manual segmentation. The ERC statistics referred to two-way ANOVA, \*\* $p < .01$ ; \*\*\* $p < .001$  after Hochberg's correction. The abbreviations were the same of Table 3.

**Table 6. DTI indices of the grey regions of interest.** MD is expressed as  $10^{-3} \text{ mm}^2/\text{s}$ . Two-way ANOVA, \* $p < .05$ ; \*\* $p < .01$ ; \*\*\* $p < .001$  after Hochberg's correction. Interaction  $p$ -values are shown in the transgene x age column. Abbreviations: Cau= caudate-putamen, Hp= hippocampus, Thal= thalamus, ns= non-significant.

**Table 7. Comparison between PDAPP and WT volume estimations across structures.** Within-site group means and standard deviation (across mice and hemispheres) of volumes and thickness derived from the manual segmentation. The ERC statistics refer to two-way ANOVA, \*\*\* $p < .001$  after Hochberg's correction. The abbreviations were the same of Table 3.

**Table 8: Summary of studies that evaluated within-scanner across session test-retest reproducibility of 3T MRI morphometry (a) and diffusion (b) results on healthy subjects.** Abbreviations: CS, cross-sectional analysis; LG, longitudinal analysis, WB= whole brain, cc\_body= body of the corpus callosum, cc\_genu= genu of the corpus callosum, cc\_spl= splenium of the corpus callosum, crts= corticospinal tract, ILF= inferior lateral fasciculus, SLF= superior lateral fasciculus.

**Table 9: Summary of demographic, MRI system and acquisition differences across MRI sites.**

**Table 10: Volume estimates across sites.** Within-site group means and standard deviation (across subjects, scanner sessions and hemispheres) of subcortical, ventricle and intracranial volumes derived from the Freesurfer longitudinal segmentation stream. Abbreviations: Hp= hippocampus, Amy= amygdala, Cau= caudate, Put= putamen, Pal= pallidum, Thal= thalamus, Lat= lateral ventricle, ICV= intracranial volume. See Table 2 for MRI sites characterization.

**Table 11: Brain volumetric reproducibility errors for the various 3T MRI sites derived from the cross-sectional (CS) and longitudinal (LG) Freesurfer segmentations.** Within each site the mean reproducibility errors is computed across subjects, across the four test-retest acquisitions and across brain hemispheres. There are no significant MRI site effects, regardless of analysis (Kruskal-Wallis test,  $p < 0.01$ ). The last column shows the reproducibility errors for each site and analysis when averaged across sites. Except for the lateral ventricles, for all other structures the reproducibility errors of LG are significantly lower than those from CS analysis (Wilcoxon test,  $p < 0.01$ ). Abbreviations for the segmented volumes: Hp= hippocampus, Amy= amygdala, Cau= caudate, Put= putamen, Pal= pallidum, Thal= thalamus, Lat= lateral ventricle volume. See Table 2 for MRI sites characterization.

**Table 12: Spatial reproducibility of volumetric segmentations.** Within-site group mean volume overlap (DICE coefficient) and standard deviation (across subjects, scanner sessions and hemispheres) derived from the Freesurfer cross-sectional (CS) and longitudinal (LG) segmentation streams. There are no significant MRI site effects, regardless of structure and analysis (Kruskal-Wallis test,  $p < 0.01$ ). The last column shows the spatial reproducibility for each site and analysis when averaged across sites. For all structures the spatial reproducibility was significantly higher with the LG analysis relative to the CS analysis (Wilcoxon test,  $p < 0.01$ ). Abbreviations: Hp= hippocampus, Amy= amygdala, Cau= caudate,



Put= putamen, Pal= pallidum, Thal= thalamus, Lat= lateral ventricle volume. See Table 2 for MRI sites characterization.

**Table 13: Cortical thickness estimates across sites.** Within-site group means and standard deviation (across subjects, scanner sessions and hemispheres) of cortical thickness derived from the Freesurfer longitudinal segmentation stream. Abbreviations: Fus= Fusiform gyrus, LatOc= Lateraloccipital gyrus, Ling= Lingual gyrus, Parahp= Parahippocampal gyrus, Prec= Precuneus, SupFr= Superiorfrontal gyrus, SupPar= Superiorparietal gyrus, SupTem= Superiortemporal gyrus, Supra= Supramarginal gyrus. See Table 2 for MRI sites characterization.

**Table 14: Effects of MRI site and processing stream on thickness reproducibility.** Within-site group mean reproducibility error and standard deviation (across subjects, scanner sessions and hemispheres) derived from the Freesurfer cross-sectional (CS) and longitudinal (LG) segmentation streams. There are no significant MRI site effects, regardless of structure and analysis (Kruskall-Wallis test,  $p < 0.01$ ). The last column shows the spatial reproducibility for each site and analysis when averaged across sites. No significant differences were found between the thickness reproducibility errors from LG and CS analyses when grouped across sites (Wilcoxon test,  $p < 0.01$ ). Abbreviations: Fus= Fusiform gyrus, LatOc= Lateraloccipital gyrus, Ling= Lingual gyrus, Parahp= Parahippocampal gyrus, Prec= Precuneus, SupFr= Superiorfrontal gyrus, SupPar= Superiorparietal gyrus, SupTem= Superiortemporal gyrus, Supra= Supramarginal gyrus. See Table 2 for MRI sites characterization.

**Table 15. Head motion parameters across MRI sites.** Maximum head rotations and translations across all subjects at each site.

**Table 16: Diffusion parameters estimates across sites.** Within-site group means and standard deviation (across subjects and scanner sessions) of FA, MD ( $10^{-3} \text{ mm}^2/\text{s}$ ) (a),  $\lambda_{II}$  ( $10^{-3} \text{ mm}^2/\text{s}$ ) and  $\lambda_{\perp}$  ( $10^{-3} \text{ mm}^2/\text{s}$ ) (b). There are no significant MRI site effects (Kruskall-Wallis test,  $p < 0.01$ ). Abbreviations: cc\_body= body of the corpus callosum, cc\_genu= genu of the corpus callosum, cc\_spl= splenium of the corpus callosum, crtsp= corticospinal tract, ILF\_L= left inferior lateral fasciculus, ILF\_R= right inferior lateral fasciculus, SLF\_L= left superior lateral fasciculus, SLF\_R= right superior lateral fasciculus. See Table 2 for MRI sites characterization.

**Table 17: Effects of MRI site on diffusion reproducibility.** Within-site group mean reproducibility error and standard deviation (across subjects and scanner sessions). The abbreviations are the same of Table 16. See Table 2 for MRI sites characterization.

**Table 18: ICC and CV of WM ROIs.** Within-site group mean ICC and CV and standard deviation of FA, MD,  $\lambda_{II}$ ,  $\lambda_{\perp}$  (across subjects, structures and scanner sessions). See Table 2 for MRI sites characterization.

**Table 19: Spatial reproducibility of WM ROI.** Within-site group mean volume overlap (DICE coefficient) and standard deviation (across subjects and scanner sessions). The last row shows the spatial reproducibility for each site. The abbreviations are the same of Table 16. See Table 2 for MRI sites characterization.

## 7 BIBLIOGRAPHY

- 1 Mucke L. Neuroscience: Alzheimer's disease. *Nature* 2009, 461: 895-897
- 2 Ferri CP, Prince M, Brayne C, Brodaty H, Fratiglioni L, Ganguli M, Hall K, *et al.* Global prevalence of dementia: a Delphi consensus study. *Lancet* 2005, 366: 2112-2117
- 3 Zanetti O, Solerte SB, Cantoni F. Life expectancy in Alzheimer's disease (AD). *Arch Gerontol Geriatr* 2009, 49 Suppl 1: 237-243
- 4 Hardy J, Allsop D. Amyloid deposition as the central event in the aetiology of Alzheimer's disease. *Trends Pharmacol Sci* 1991, 12: 383-388
- 5 Grundke-Iqbal I, Iqbal K, Quinlan M, Tung Y, Zaidi M, Wisniewski H. Microtubule-associated protein tau. A component of Alzheimer paired helical filaments. *J Biol Chem* 1986, 261: 6084-6089
- 6 Grundke-Iqbal I, Iqbal K, Tung Y, Quinlan M, Wisniewski H, Binder L. Abnormal phosphorylation of the microtubule-associated protein tau (tau) in Alzheimer cytoskeletal pathology. *Proc Natl Acad Sci U S A* 1986, 83: 4913-4917
- 7 Jack CR, Knopman DS, Jagust WJ, Shaw LM, Aisen PS, Weiner MW, Petersen RC, *et al.* Hypothetical model of dynamic biomarkers of the Alzheimer's pathological cascade. *Lancet Neurol* 2010, 9: 119-128
- 8 Glenner GG, Wong CW. Alzheimer's disease: initial report of the purification and characterization of a novel cerebrovascular amyloid protein. *Biochem Biophys Res Commun* 1984, 120: 885-890
- 9 Masters CL, Simms G, Weinman NA, Multhaup G, McDonald BL, Beyreuther K. Amyloid plaque core protein in Alzheimer disease and Down syndrome. *Proc Natl Acad Sci U S A* 1985, 82: 4245-4249
- 10 Learning from failure. *Nat Rev Drug Discov* 2010, 9: 499
- 11 Schneider LS, Sano M. Current Alzheimer's disease clinical trials: methods and placebo outcomes. *Alzheimers Dement* 2009, 5: 388-397
- 12 Fox NC, Cousens S, Scahill R, Harvey RJ, Rossor MN. Using serial registered brain magnetic resonance imaging to measure disease progression in Alzheimer disease: power calculations and estimates of sample size to detect treatment effects. *Arch Neurol* 2000, 57: 339-344
- 13 Sperling RA, Aisen PS, Beckett LA, Bennett DA, Craft S, Fagan AM, Iwatsubo T, *et al.* Toward defining the preclinical stages of Alzheimer's disease: recommendations from the National Institute on Aging-Alzheimer's Association workgroups on diagnostic guidelines for Alzheimer's disease. *Alzheimers Dement* 2011, 7: 280-292
- 14 Thompson P, Hayashi K, de Zubizaray G, Janke A, Rose S, Semple J, Herman D, *et al.* Dynamics of gray matter loss in Alzheimer's disease. *J Neurosci* 2003, 23: 994-1005
- 15 Bronge L, Bogdanovic N, Wahlund L. Postmortem MRI and histopathology of white matter changes in Alzheimer brains. A quantitative, comparative study. *Dement Geriatr Cogn Disord* 2002, 13: 205-212
- 16 van Duinen S, Castaño E, Prelli F, Bots G, Luyendijk W, Frangione B. Hereditary cerebral hemorrhage with amyloidosis in patients of Dutch origin is related to Alzheimer disease. *Proc Natl Acad Sci U S A* 1987, 84: 5991-5994
- 17 Chartier-Harlin M, Crawford F, Houlden H, Warren A, Hughes D, Fidani L, Goate A, *et al.* Early-onset Alzheimer's disease caused by mutations at codon 717 of the beta-amyloid precursor protein gene. *Nature* 1991, 353: 844-846

- 18 Sherrington R, Rogaev E, Liang Y, Rogaeva E, Levesque G, Ikeda M, Chi H, *et al.* Cloning of a gene bearing missense mutations in early-onset familial Alzheimer's disease. *Nature* 1995, 375: 754-760
- 19 Levy-Lahad E, Wasco W, Poorkaj P, Romano D, Oshima J, Pettingell W, Yu C, *et al.* Candidate gene for the chromosome 1 familial Alzheimer's disease locus. *Science* 1995, 269: 973-977
- 20 Spillantini MG, Murrell JR, Goedert M, Farlow MR, Klug A, Ghetti B. Mutation in the tau gene in familial multiple system tauopathy with presenile dementia. *Proc Natl Acad Sci U S A* 1998, 95: 7737-7741
- 21 Games D, Adams D, Alessandrini R, Barbour R, Berthelette P, Blackwell C, Carr T, *et al.* Alzheimer-type neuropathology in transgenic mice overexpressing V717F beta-amyloid precursor protein. *Nature* 1995, 373: 523-527
- 22 Hsiao K, Chapman P, Nilsen S, Eckman C, Harigaya Y, Younkin S, Yang F, *et al.* Correlative memory deficits, Abeta elevation, and amyloid plaques in transgenic mice. *Science* 1996, 274: 99-102
- 23 Casas C, Sergeant N, Itier JM, Blanchard V, Wirths O, van der Kolk N, Vingthedeux V, *et al.* Massive CA1/2 neuronal loss with intraneuronal and N-terminal truncated Abeta42 accumulation in a novel Alzheimer transgenic model. *Am J Pathol* 2004, 165: 1289-1300
- 24 Irizarry MC, McNamara M, Fedorchak K, Hsiao K, Hyman BT. APPSw transgenic mice develop age-related A beta deposits and neuropil abnormalities, but no neuronal loss in CA1. *J Neuropathol Exp Neurol* 1997, 56: 965-973
- 25 Delatour B, Guegan M, Volk A, Dhenain M. In vivo MRI and histological evaluation of brain atrophy in APP/PS1 transgenic mice. *Neurobiol Aging* 2006, 27: 835-847
- 26 Richards JG, Higgins GA, Ouagazzal AM, Ozmen L, Kew JN, Bohrmann B, Malherbe P, *et al.* PS2APP transgenic mice, coexpressing hPS2mut and hAPPswe, show age-related cognitive deficits associated with discrete brain amyloid deposition and inflammation. *J Neurosci* 2003, 23: 8989-9003
- 27 Oddo S, Caccamo A, Shepherd JD, Murphy MP, Golde TE, Kaye R, Metherate R, *et al.* Triple-transgenic model of Alzheimer's disease with plaques and tangles: intracellular Abeta and synaptic dysfunction. *Neuron* 2003, 39: 409-421
- 28 Grueninger F, Bohrmann B, Czech C, Ballard TM, Frey JR, Weidensteiner C, von Kienlin M, *et al.* Phosphorylation of Tau at S422 is enhanced by Abeta in TauPS2APP triple transgenic mice. *Neurobiol Dis* 2010, 37: 294-306
- 29 Sinha S, Anderson J, Barbour R, Basi G, Caccavello R, Davis D, Doan M, *et al.* Purification and cloning of amyloid precursor protein beta-secretase from human brain. *Nature* 1999, 402: 537-540
- 30 Vassar R, Bennett B, Babu-Khan S, Kahn S, Mendiaz E, Denis P, Teplow D, *et al.* Beta-secretase cleavage of Alzheimer's amyloid precursor protein by the transmembrane aspartic protease BACE. *Science* 1999, 286: 735-741
- 31 Sabo S, Ikin A, Buxbaum J, Greengard P. The Alzheimer amyloid precursor protein (APP) and FE65, an APP-binding protein, regulate cell movement. *J Cell Biol* 2001, 153: 1403-1414
- 32 Chen Y. APP induces neuronal apoptosis through APP-BP1-mediated downregulation of beta-catenin. *Apoptosis* 2004, 9: 415-422

- 33 Kwak Y, Dantuma E, Merchant S, Bushnev S, Sugaya K. Amyloid- $\beta$  precursor protein induces glial differentiation of neural progenitor cells by activation of the IL-6/gp130 signaling pathway. *Neurotox Res* 2010, 18: 328-338
- 34 Kamenetz F, Tomita T, Hsieh H, Seabrook G, Borchelt D, Iwatsubo T, Sisodia S, *et al.* APP processing and synaptic function. *Neuron* 2003, 37: 925-937
- 35 Li H, Wang B, Wang Z, Guo Q, Tabuchi K, Hammer R, Südhof T, *et al.* Soluble amyloid precursor protein (APP) regulates transthyretin and Klotho gene expression without rescuing the essential function of APP. *Proc Natl Acad Sci U S A* 2010, 107: 17362-17367
- 36 Selkoe DJ. Alzheimer's disease: genes, proteins, and therapy. *Physiol Rev* 2001, 81: 741-766
- 37 Nilsberth C, Westlind-Danielsson A, Eckman CB, Condron MM, Axelman K, Forsell C, Stenh C, *et al.* The 'Arctic' APP mutation (E693G) causes Alzheimer's disease by enhanced Abeta protofibril formation. *Nat Neurosci* 2001, 4: 887-893
- 38 Francis R, McGrath G, Zhang J, Ruddy D, Sym M, Apfeld J, Nicoll M, *et al.* aph-1 and pen-2 are required for Notch pathway signaling, gamma-secretase cleavage of betaAPP, and presenilin protein accumulation. *Dev Cell* 2002, 3: 85-97
- 39 Yu G, Nishimura M, Arawaka S, Levitan D, Zhang L, Tandon A, Song Y, *et al.* Nicastrin modulates presenilin-mediated notch/glp-1 signal transduction and betaAPP processing. *Nature* 2000, 407: 48-54
- 40 Zhang C, Wu B, Beglopoulos V, Wines-Samuelson M, Zhang D, Dragatsis I, Südhof TC, *et al.* Presenilins are essential for regulating neurotransmitter release. *Nature* 2009, 460: 632-636
- 41 Takashima A, Murayama M, Murayama O, Kohno T, Honda T, Yasutake K, Nihonmatsu N, *et al.* Presenilin 1 associates with glycogen synthase kinase-3beta and its substrate tau. *Proc Natl Acad Sci U S A* 1998, 95: 9637-9641
- 42 Takashima A. GSK-3 is essential in the pathogenesis of Alzheimer's disease. *J Alzheimers Dis* 2006, 9: 309-317
- 43 Zhang H, Sun S, Herreman A, De Strooper B, Bezprozvanny I. Role of presenilins in neuronal calcium homeostasis. *J Neurosci* 2010, 30: 8566-8580
- 44 Naruse S, Thinakaran G, Luo J, Kusiak J, Tomita T, Iwatsubo T, Qian X, *et al.* Effects of PS1 deficiency on membrane protein trafficking in neurons. *Neuron* 1998, 21: 1213-1221
- 45 Kim S, Leem J, Lah J, Slunt H, Levey A, Thinakaran G, Sisodia S. Multiple effects of aspartate mutant presenilin 1 on the processing and trafficking of amyloid precursor protein. *J Biol Chem* 2001, 276: 43343-43350
- 46 Edbauer D, Winkler E, Haass C, Steiner H. Presenilin and nicastrin regulate each other and determine amyloid beta-peptide production via complex formation. *Proc Natl Acad Sci U S A* 2002, 99: 8666-8671
- 47 Ghidoni R, Benussi L, Paterlini A, Missale C, Usardi A, Rossi R, Barbiero L, *et al.* Presenilin 2 mutations alter cystatin C trafficking in mouse primary neurons. *Neurobiol Aging* 2007, 28: 371-376
- 48 Begley J, Duan W, Chan S, Duff K, Mattson M. Altered calcium homeostasis and mitochondrial dysfunction in cortical synaptic compartments of presenilin-1 mutant mice. *J Neurochem* 1999, 72: 1030-1039
- 49 Chakroborty S, Goussakov I, Miller M, Stutzmann G. Deviant ryanodine receptor-mediated calcium release resets synaptic homeostasis in presymptomatic 3xTg-AD mice. *J Neurosci* 2009, 29: 9458-9470

- 50 Sturchler-Pierrat C, Abramowski D, Duke M, Wiederhold KH, Mistl C, Rothacher S, Ledermann B, *et al.* Two amyloid precursor protein transgenic mouse models with Alzheimer disease-like pathology. *Proc Natl Acad Sci U S A* 1997, 94: 13287-13292
- 51 Duff K, Eckman C, Zehr C, Yu X, Prada CM, Perez-tur J, Hutton M, *et al.* Increased amyloid-beta<sub>42</sub>(43) in brains of mice expressing mutant presenilin 1. *Nature* 1996, 383: 710-713
- 52 Borchelt DR, Ratovitski T, van Lare J, Lee MK, Gonzales V, Jenkins NA, Copeland NG, *et al.* Accelerated amyloid deposition in the brains of transgenic mice coexpressing mutant presenilin 1 and amyloid precursor proteins. *Neuron* 1997, 19: 939-945
- 53 Howlett DR, Richardson JC, Austin A, Parsons AA, Bate ST, Davies DC, Gonzalez MI. Cognitive correlates of Abeta deposition in male and female mice bearing amyloid precursor protein and presenilin-1 mutant transgenes. *Brain Res* 2004, 1017: 130-136
- 54 Wirths O, Multhaup G, Bayer T. A modified beta-amyloid hypothesis: intraneuronal accumulation of the beta-amyloid peptide--the first step of a fatal cascade. *J Neurochem* 2004, 91: 513-520
- 55 Bayer T, Wirths O. Intracellular accumulation of amyloid-Beta - a predictor for synaptic dysfunction and neuron loss in Alzheimer's disease. *Front Aging Neurosci* 2010, 2: 8
- 56 Zheng H, Jiang M, Trumbauer M, Sirinathsinghji D, Hopkins R, Smith D, Heavens R, *et al.* beta-Amyloid precursor protein-deficient mice show reactive gliosis and decreased locomotor activity. *Cell* 1995, 81: 525-531
- 57 Handler M, Yang X, Shen J. Presenilin-1 regulates neuronal differentiation during neurogenesis. *Development* 2000, 127: 2593-2606
- 58 Shen J, Bronson R, Chen D, Xia W, Selkoe D, Tonegawa S. Skeletal and CNS defects in Presenilin-1-deficient mice. *Cell* 1997, 89: 629-639
- 59 Steiner H, Duff K, Capell A, Romig H, Grim M, Lincoln S, Hardy J, *et al.* A loss of function mutation of presenilin-2 interferes with amyloid beta-peptide production and notch signaling. *J Biol Chem* 1999, 274: 28669-28673
- 60 Donoviel D, Hadjantonakis A, Ikeda M, Zheng H, Hyslop P, Bernstein A. Mice lacking both presenilin genes exhibit early embryonic patterning defects. *Genes Dev* 1999, 13: 2801-2810
- 61 Beglopoulos V, Sun X, Saura C, Lemere C, Kim R, Shen J. Reduced beta-amyloid production and increased inflammatory responses in presenilin conditional knock-out mice. *J Biol Chem* 2004, 279: 46907-46914
- 62 Feng R, Wang H, Wang J, Shrom D, Zeng X, Tsien J. Forebrain degeneration and ventricle enlargement caused by double knockout of Alzheimer's presenilin-1 and presenilin-2. *Proc Natl Acad Sci U S A* 2004, 101: 8162-8167
- 63 Luo Y, Bolon B, Kahn S, Bennett B, Babu-Khan S, Denis P, Fan W, *et al.* Mice deficient in BACE1, the Alzheimer's beta-secretase, have normal phenotype and abolished beta-amyloid generation. *Nat Neurosci* 2001, 4: 231-232
- 64 Goedert M, Jakes R. Mutations causing neurodegenerative tauopathies. *Biochim Biophys Acta* 2005, 1739: 240-250
- 65 Binder L, Frankfurter A, Rebhun L. The distribution of tau in the mammalian central nervous system. *J Cell Biol* 1985, 101: 1371-1378
- 66 Dixit R, Ross JL, Goldman YE, Holzbaur EL. Differential regulation of dynein and kinesin motor proteins by tau. *Science* 2008, 319: 1086-1089

- 67 Dawson H, Ferreira A, Eyster M, Ghoshal N, Binder L, Vitek M. Inhibition of neuronal maturation in primary hippocampal neurons from tau deficient mice. *J Cell Sci* 2001, 114: 1179-1187
- 68 Perez M, Santa-Maria I, Gomez de Barreda E, Zhu X, Cuadros R, Cabrero JR, Sanchez-Madrid F, *et al.* Tau--an inhibitor of deacetylase HDAC6 function. *J Neurochem* 2009, 109: 1756-1766
- 69 Khlistunova I, Biernat J, Wang Y, Pickhardt M, von Bergen M, Gazova Z, Mandelkow E, *et al.* Inducible expression of Tau repeat domain in cell models of tauopathy: aggregation is toxic to cells but can be reversed by inhibitor drugs. *J Biol Chem* 2006, 281: 1205-1214
- 70 Michel G, Mercken M, Murayama M, Noguchi K, Ishiguro K, Imahori K, Takashima A. Characterization of tau phosphorylation in glycogen synthase kinase-3beta and cyclin dependent kinase-5 activator (p23) transfected cells. *Biochim Biophys Acta* 1998, 1380: 177-182
- 71 Alvarez A, Toro R, Cáceres A, Maccioni R. Inhibition of tau phosphorylating protein kinase cdk5 prevents beta-amyloid-induced neuronal death. *FEBS Lett* 1999, 459: 421-426
- 72 Goedert M, Jakes R, Crowther R, Six J, Lübke U, Vandermeeren M, Cras P, *et al.* The abnormal phosphorylation of tau protein at Ser-202 in Alzheimer disease recapitulates phosphorylation during development. *Proc Natl Acad Sci U S A* 1993, 90: 5066-5070
- 73 Denk F, Wade-Martins R. Knock-out and transgenic mouse models of tauopathies. *Neurobiol Aging* 2009, 30: 1-13
- 74 Cruz JC, Tseng HC, Goldman JA, Shih H, Tsai LH. Aberrant Cdk5 activation by p25 triggers pathological events leading to neurodegeneration and neurofibrillary tangles. *Neuron* 2003, 40: 471-483
- 75 Lucas JJ, Hernández F, Gómez-Ramos P, Morán MA, Hen R, Avila J. Decreased nuclear beta-catenin, tau hyperphosphorylation and neurodegeneration in GSK-3beta conditional transgenic mice. *EMBO J* 2001, 20: 27-39
- 76 Gotz J, Schild A, Hoernkli F, Pennanen L. Amyloid-induced neurofibrillary tangle formation in Alzheimer's disease: insight from transgenic mouse and tissue-culture models. *Int J Dev Neurosci* 2004, 22: 453-465
- 77 Irizarry MC, Soriano F, McNamara M, Page KJ, Schenk D, Games D, Hyman BT. Abeta deposition is associated with neuropil changes, but not with overt neuronal loss in the human amyloid precursor protein V717F (PDAPP) transgenic mouse. *J Neurosci* 1997, 17: 7053-7059
- 78 Wirths O, Weis J, Kaye R, Saido TC, Bayer TA. Age-dependent axonal degeneration in an Alzheimer mouse model. *Neurobiol Aging* 2007, 28: 1689-1699
- 79 Bassar P, Pierpaoli C. Microstructural and physiological features of tissues elucidated by quantitative-diffusion-tensor MRI. *J Magn Reson B* 1996, 111: 209-219
- 80 Zhang B, Higuchi M, Yoshiyama Y, Ishihara T, Forman MS, Martinez D, Joyce S, *et al.* Retarded axonal transport of R406W mutant tau in transgenic mice with a neurodegenerative tauopathy. *J Neurosci* 2004, 24: 4657-4667
- 81 Ittner LM, Fath T, Ke YD, Bi M, van Eersel J, Li KM, Gunning P, *et al.* Parkinsonism and impaired axonal transport in a mouse model of frontotemporal dementia. *Proc Natl Acad Sci U S A* 2008, 105: 15997-16002

- 82 Yuan A, Kumar A, Peterhoff C, Duff K, Nixon RA. Axonal transport rates in vivo are unaffected by tau deletion or overexpression in mice. *J Neurosci* 2008, 28: 1682-1687
- 83 Dawson H, Cantillana V, Jansen M, Wang H, Vitek M, Wilcock D, Lynch J, *et al.* Loss of tau elicits axonal degeneration in a mouse model of Alzheimer's disease. *Neuroscience* 2010, 169: 516-531
- 84 Smith K, Peethumnongsin E, Lin H, Zheng H, Pautler R. Increased Human Wildtype Tau Attenuates Axonal Transport Deficits Caused by Loss of APP in Mouse Models. *Magn Reson Insights* 2010, 4: 11-18
- 85 Vossel KA, Zhang K, Brodbeck J, Daub AC, Sharma P, Finkbeiner S, Cui B, *et al.* Tau reduction prevents Abeta-induced defects in axonal transport. *Science* 2010, 330: 198
- 86 Zempel H, Thies E, Mandelkow E, Mandelkow E. Abeta oligomers cause localized Ca(2+) elevation, missorting of endogenous Tau into dendrites, Tau phosphorylation, and destruction of microtubules and spines. *J Neurosci* 2010, 30: 11938-11950
- 87 Zheng W, Bastianetto S, Mennicken F, Ma W, Kar S. Amyloid beta peptide induces tau phosphorylation and loss of cholinergic neurons in rat primary septal cultures. *Neuroscience* 2002, 115: 201-211
- 88 Peethumnongsin E, Yang L, Kallhoff-Muñoz V, Hu L, Takashima A, Pautler RG, Zheng H. Convergence of presenilin- and tau-mediated pathways on axonal trafficking and neuronal function. *J Neurosci* 2010, 30: 13409-13418
- 89 Lazarov O, Morfini G, Pigino G, Gadadhar A, Chen X, Robinson J, Ho H, *et al.* Impairments in fast axonal transport and motor neuron deficits in transgenic mice expressing familial Alzheimer's disease-linked mutant presenilin 1. *J Neurosci* 2007, 27: 7011-7020
- 90 Maloney MT, Bamberg JR. Cofilin-mediated neurodegeneration in Alzheimer's disease and other amyloidopathies. *Mol Neurobiol* 2007, 35: 21-44
- 91 Whiteman IT, Gervasio OL, Cullen KM, Guillemin GJ, Jeong EV, Witting PK, Antao ST, *et al.* Activated actin-depolymerizing factor/cofilin sequesters phosphorylated microtubule-associated protein during the assembly of alzheimer-like neuritic cytoskeletal striations. *J Neurosci* 2009, 29: 12994-13005
- 92 Kamal A, Almenar-Queralt A, LeBlanc JF, Roberts EA, Goldstein LS. Kinesin-mediated axonal transport of a membrane compartment containing beta-secretase and presenilin-1 requires APP. *Nature* 2001, 414: 643-648
- 93 Stokin GB, Lillo C, Falzone TL, Brusch RG, Rockenstein E, Mount SL, Raman R, *et al.* Axonopathy and transport deficits early in the pathogenesis of Alzheimer's disease. *Science* 2005, 307: 1282-1288
- 94 DeKosky ST, Scheff SW. Synapse loss in frontal cortex biopsies in Alzheimer's disease: correlation with cognitive severity. *Ann Neurol* 1990, 27: 457-464
- 95 Coleman PD, Yao PJ. Synaptic slaughter in Alzheimer's disease. *Neurobiol Aging* 2003, 24: 1023-1027
- 96 Laakso MP. Structural imaging in cognitive impairment and the dementias: an update. *Curr Opin Neurol* 2002, 15: 415-421
- 97 Gengler S, Hamilton A, Holscher C. Synaptic plasticity in the hippocampus of a APP/PS1 mouse model of Alzheimer's disease is impaired in old but not young mice. *PLoS One* 2010, 5: e9764

- 98 Radde R, Bolmont T, Kaeser SA, Coomaraswamy J, Lindau D, Stoltze L, Calhoun ME, *et al.* Abeta42-driven cerebral amyloidosis in transgenic mice reveals early and robust pathology. *EMBO Rep* 2006, 7: 940-946
- 99 Chapman PF, White GL, Jones MW, Cooper-Blacketer D, Marshall VJ, Irizarry M, YOUNKIN L, *et al.* Impaired synaptic plasticity and learning in aged amyloid precursor protein transgenic mice. *Nat Neurosci* 1999, 2: 271-276
- 100 Breyhan H, Wirths O, Duan K, Marcello A, Rettig J, Bayer TA. APP/PS1KI bigenic mice develop early synaptic deficits and hippocampus atrophy. *Acta Neuropathol* 2009, 117: 677-685
- 101 Fitzjohn SM, Morton RA, Kuenzi F, Rosahl TW, Shearman M, Lewis H, Smith D, *et al.* Age-related impairment of synaptic transmission but normal long-term potentiation in transgenic mice that overexpress the human APP695SWE mutant form of amyloid precursor protein. *J Neurosci* 2001, 21: 4691-4698
- 102 Christensen DZ, Kraus SL, Flohr A, Cotel MC, Wirths O, Bayer TA. Transient intraneuronal A beta rather than extracellular plaque pathology correlates with neuron loss in the frontal cortex of APP/PS1KI mice. *Acta Neuropathol* 2008, 116: 647-655
- 103 Rutten B, Van der Kolk N, Schafer S, van Zandvoort M, Bayer T, Steinbusch H, Schmitz C. Age-related loss of synaptophysin immunoreactive presynaptic boutons within the hippocampus of APP751SL, PS1M146L, and APP751SL/PS1M146L transgenic mice. *Am J Pathol* 2005, 167: 161-173
- 104 Fitzjohn SM, Kuenzi F, Morton RA, Rosahl TW, Lewis H, Smith D, Seabrook GR, *et al.* A study of long-term potentiation in transgenic mice over-expressing mutant forms of both amyloid precursor protein and presenilin-1. *Mol Brain* 2010, 3: 21
- 105 Tomiyama T, Matsuyama S, Iso H, Umeda T, Takuma H, Ohnishi K, Ishibashi K, *et al.* A mouse model of amyloid beta oligomers: their contribution to synaptic alteration, abnormal tau phosphorylation, glial activation, and neuronal loss in vivo. *J Neurosci* 2010, 30: 4845-4856
- 106 Townsend M, Qu Y, Gray A, Wu Z, Seto T, Hutton M, Shearman MS, *et al.* Oral treatment with a gamma-secretase inhibitor improves long-term potentiation in a mouse model of Alzheimer's disease. *J Pharmacol Exp Ther* 2010, 333: 110-119
- 107 Polydoro M, Acker CM, Duff K, Castillo PE, Davies P. Age-dependent impairment of cognitive and synaptic function in the htau mouse model of tau pathology. *J Neurosci* 2009, 29: 10741-10749
- 108 Yoshiyama Y, Higuchi M, Zhang B, Huang SM, Iwata N, Saido TC, Maeda J, *et al.* Synapse loss and microglial activation precede tangles in a P301S tauopathy mouse model. *Neuron* 2007, 53: 337-351
- 109 Eckermann K, Mocanu MM, Khlistunova I, Biernat J, Nissen A, Hofmann A, Schöning K, *et al.* The beta-propensity of Tau determines aggregation and synaptic loss in inducible mouse models of tauopathy. *J Biol Chem* 2007, 282: 31755-31765
- 110 Yao P, Bushlin I, Furukawa K. Preserved synaptic vesicle recycling in hippocampal neurons in a mouse Alzheimer's disease model. *Biochem Biophys Res Commun* 2005, 330: 34-38
- 111 Bertoni-Freddari C, Sensi SL, Giorgetti B, Balialetti M, Di Stefano G, Canzoniero LM, Casoli T, *et al.* Decreased presence of perforated synapses in a triple-transgenic mouse model of Alzheimer's disease. *Rejuvenation Res* 2008, 11: 309-313



- 112 Oddo S, Vasilevko V, Caccamo A, Kitazawa M, Cribbs DH, LaFerla FM. Reduction of soluble Abeta and tau, but not soluble Abeta alone, ameliorates cognitive decline in transgenic mice with plaques and tangles. *J Biol Chem* 2006, 281: 39413-39423
- 113 Lesné S, Kotilinek L, Ashe KH. Plaque-bearing mice with reduced levels of oligomeric amyloid-beta assemblies have intact memory function. *Neuroscience* 2008, 151: 745-749
- 114 Walsh DM, Klyubin I, Fadeeva JV, Cullen WK, Anwyl R, Wolfe MS, Rowan MJ, *et al.* Naturally secreted oligomers of amyloid beta protein potently inhibit hippocampal long-term potentiation in vivo. *Nature* 2002, 416: 535-539
- 115 Shankar GM, Bloodgood BL, Townsend M, Walsh DM, Selkoe DJ, Sabatini BL. Natural oligomers of the Alzheimer amyloid-beta protein induce reversible synapse loss by modulating an NMDA-type glutamate receptor-dependent signaling pathway. *J Neurosci* 2007, 27: 2866-2875
- 116 Kelly JF, Furukawa K, Barger SW, Rengen MR, Mark RJ, Blanc EM, Roth GS, *et al.* Amyloid beta-peptide disrupts carbachol-induced muscarinic cholinergic signal transduction in cortical neurons. *Proc Natl Acad Sci U S A* 1996, 93: 6753-6758
- 117 Hoshi M, Takashima A, Murayama M, Yasutake K, Yoshida N, Ishiguro K, Hoshino T, *et al.* Nontoxic amyloid beta peptide 1-42 suppresses acetylcholine synthesis. Possible role in cholinergic dysfunction in Alzheimer's disease. *J Biol Chem* 1997, 272: 2038-2041
- 118 Ye L, Qi JS, Qiao JT. Long-term potentiation in hippocampus of rats is enhanced by endogenous acetylcholine in a way that is independent of N-methyl-D-aspartate receptors. *Neurosci Lett* 2001, 300: 145-148
- 119 Dzieczapolski G, Glogowski CM, Masliah E, Heinemann SF. Deletion of the alpha 7 nicotinic acetylcholine receptor gene improves cognitive deficits and synaptic pathology in a mouse model of Alzheimer's disease. *J Neurosci* 2009, 29: 8805-8815
- 120 Kim JH, Anwyl R, Suh YH, Djamgoz MB, Rowan MJ. Use-dependent effects of amyloidogenic fragments of (beta)-amyloid precursor protein on synaptic plasticity in rat hippocampus in vivo. *J Neurosci* 2001, 21: 1327-1333
- 121 Chen QS, Wei WZ, Shimahara T, Xie CW. Alzheimer amyloid beta-peptide inhibits the late phase of long-term potentiation through calcineurin-dependent mechanisms in the hippocampal dentate gyrus. *Neurobiol Learn Mem* 2002, 77: 354-371
- 122 Renner M, Lacor PN, Velasco PT, Xu J, Contractor A, Klein WL, Triller A. Deleterious effects of amyloid beta oligomers acting as an extracellular scaffold for mGluR5. *Neuron* 2010, 66: 739-754
- 123 Hsieh H, Boehm J, Sato C, Iwatsubo T, Tomita T, Sisodia S, Malinow R. AMPAR removal underlies Abeta-induced synaptic depression and dendritic spine loss. *Neuron* 2006, 52: 831-843
- 124 Braak H, Braak E. Neuropathological staging of Alzheimer-related changes. *Acta Neuropathol* 1991, 82: 239-259
- 125 Arriagada PV, Growdon JH, Hedley-Whyte ET, Hyman BT. Neurofibrillary tangles but not senile plaques parallel duration and severity of Alzheimer's disease. *Neurology* 1992, 42: 631-639
- 126 Frisoni GB, Fox NC, Jack CR, Scheltens P, Thompson PM. The clinical use of structural MRI in Alzheimer disease. *Nat Rev Neurol* 2010, 6: 67-77

- 127 Driscoll I, Davatzikos C, An Y, Wu X, Shen D, Kraut M, Resnick SM. Longitudinal pattern of regional brain volume change differentiates normal aging from MCI. *Neurology* 2009, 72: 1906-1913
- 128 Redwine JM, Kosofsky B, Jacobs RE, Games D, Reilly JF, Morrison JH, Young WG, *et al.* Dentate gyrus volume is reduced before onset of plaque formation in PDAPP mice: a magnetic resonance microscopy and stereologic analysis. *Proc Natl Acad Sci U S A* 2003, 100: 1381-1386
- 129 Van Broeck B, Vanhoutte G, Pirici D, Van Dam D, Wils H, Cuijt I, Vennekens K, *et al.* Intraneuronal amyloid beta and reduced brain volume in a novel APP T714I mouse model for Alzheimer's disease. *Neurobiol Aging* 2008, 29: 241-252
- 130 von Kienlin M, Kunnecke B, Metzger F, Steiner G, Richards JG, Ozmen L, Jacobsen H, *et al.* Altered metabolic profile in the frontal cortex of PS2APP transgenic mice, monitored throughout their life span. *Neurobiol Dis* 2005, 18: 32-39
- 131 Lau JC, Lerch JP, Sled JG, Henkelman RM, Evans AC, Bedell BJ. Longitudinal neuroanatomical changes determined by deformation-based morphometry in a mouse model of Alzheimer's disease. *Neuroimage* 2008, 42: 19-27
- 132 Maheswaran S, Barjat H, Rueckert D, Bate S, Howlett D, Tilling L, Smart S, *et al.* Longitudinal regional brain volume changes quantified in normal aging and Alzheimer's APP x PS1 mice using MRI. *Brain Res* 2009, 1270: 19-32
- 133 Badea A, Johnson GA, Jankowsky JL. Remote sites of structural atrophy predict later amyloid formation in a mouse model of Alzheimer's disease. *Neuroimage* 2010, 50: 416-427
- 134 Stahl R, Dietrich O, Teipel SJ, Hampel H, Reiser MF, Schoenberg SO. White matter damage in Alzheimer disease and mild cognitive impairment: assessment with diffusion-tensor MR imaging and parallel imaging techniques. *Radiology* 2007, 243: 483-492
- 135 Liu Y, Spulber G, Lehtimäki KK, Könönen M, Hallikainen I, Gröhn H, Kivipelto M, *et al.* Diffusion tensor imaging and Tract-Based Spatial Statistics in Alzheimer's disease and mild cognitive impairment. *Neurobiol Aging* 2009,
- 136 Kiuchi K, Morikawa M, Taoka T, Nagashima T, Yamauchi T, Makinodan M, Norimoto K, *et al.* Abnormalities of the uncinate fasciculus and posterior cingulate fasciculus in mild cognitive impairment and early Alzheimer's disease: a diffusion tensor tractography study. *Brain Res* 2009, 1287: 184-191
- 137 Fellgiebel A, Wille P, Müller MJ, Winterer G, Scheurich A, Vucurevic G, Schmidt LG, *et al.* Ultrastructural hippocampal and white matter alterations in mild cognitive impairment: a diffusion tensor imaging study. *Dement Geriatr Cogn Disord* 2004, 18: 101-108
- 138 Song SK, Kim JH, Lin SJ, Brendza RP, Holtzman DM. Diffusion tensor imaging detects age-dependent white matter changes in a transgenic mouse model with amyloid deposition. *Neurobiol Dis* 2004, 15: 640-647
- 139 Sun SW, Song SK, Harms MP, Lin SJ, Holtzman DM, Merchant KM, Kotyk JJ. Detection of age-dependent brain injury in a mouse model of brain amyloidosis associated with Alzheimer's disease using magnetic resonance diffusion tensor imaging. *Exp Neurol* 2005, 191: 77-85
- 140 Thiessen JD, Glazner KA, Nafez S, Schellenberg AE, Buist R, Martin M, Albeni BC. Histochemical visualization and diffusion MRI at 7 Tesla in the

- TgCRND8 transgenic model of Alzheimer's disease. *Brain Struct Funct* 2010, 215: 29-36
- 141 de la Torre JC. Is Alzheimer's disease a neurodegenerative or a vascular disorder? Data, dogma, and dialectics. *Lancet Neurol* 2004, 3: 184-190
- 142 Bruehl C, Witte OW. Cellular activity underlying altered brain metabolism during focal epileptic activity. *Ann Neurol* 1995, 38: 414-420
- 143 Mosconi L, Mistur R, Switalski R, Tsui WH, Glodzik L, Li Y, Pirraglia E, *et al.* FDG-PET changes in brain glucose metabolism from normal cognition to pathologically verified Alzheimer's disease. *Eur J Nucl Med Mol Imaging* 2009, 36: 811-822
- 144 Jagust W. Positron emission tomography and magnetic resonance imaging in the diagnosis and prediction of dementia. *Alzheimers Dement* 2006, 2: 36-42
- 145 Poisnel G, Hérard AS, El Tannir El Tayara N, Bourrin E, Volk A, Kober F, Delatour B, *et al.* Increased regional cerebral glucose uptake in an APP/PS1 model of Alzheimer's disease. *Neurobiol Aging* 2011,
- 146 Kuntner C, Kesner AL, Bauer M, Kremslehner R, Wanek T, Mandler M, Karch R, *et al.* Limitations of small animal PET imaging with [18F]FDDNP and FDG for quantitative studies in a transgenic mouse model of Alzheimer's disease. *Mol Imaging Biol* 2009, 11: 236-240
- 147 Luo F, Rustay NR, Ebert U, Hradil VP, Cole TB, Llano DA, Mudd SR, *et al.* Characterization of 7- and 19-month-old Tg2576 mice using multimodal in vivo imaging: limitations as a translatable model of Alzheimer's disease. *Neurobiol Aging* 2010,
- 148 Reiman EM, Uecker A, Gonzalez-Lima F, Minear D, Chen K, Callaway NL, Berndt JD, *et al.* Tracking Alzheimer's disease in transgenic mice using fluorodeoxyglucose autoradiography. *Neuroreport* 2000, 11: 987-991
- 149 Valla J, Gonzalez-Lima F, Reiman EM. FDG autoradiography reveals developmental and pathological effects of mutant amyloid in PDAPP transgenic mice. *Int J Dev Neurosci* 2008, 26: 253-258
- 150 Valla J, Schneider L, Reiman EM. Age- and transgene-related changes in regional cerebral metabolism in PSAPP mice. *Brain Res* 2006, 1116: 194-200
- 151 Nicholson RM, Kusne Y, Nowak LA, Laferla FM, Reiman EM, Valla J. Regional cerebral glucose uptake in the 3xTG model of Alzheimer's disease highlights common regional vulnerability across AD mouse models. *Brain Res* 2010,
- 152 González RG, Fischman AJ, Guimaraes AR, Carr CA, Stern CE, Halpern EF, Growdon JH, *et al.* Functional MR in the evaluation of dementia: correlation of abnormal dynamic cerebral blood volume measurements with changes in cerebral metabolism on positron emission tomography with fludeoxyglucose F 18. *AJNR Am J Neuroradiol* 1995, 16: 1763-1770
- 153 Bradley KM, O'Sullivan VT, Soper ND, Nagy Z, King EM, Smith AD, Shepstone BJ. Cerebral perfusion SPET correlated with Braak pathological stage in Alzheimer's disease. *Brain* 2002, 125: 1772-1781
- 154 Habert MO, de Souza LC, Lamari F, Daragon N, Desarnaud S, Jardel C, Dubois B, *et al.* Brain perfusion SPECT correlates with CSF biomarkers in Alzheimer's disease. *Eur J Nucl Med Mol Imaging* 2010, 37: 589-593
- 155 Moreno H, Wu WE, Lee T, Brickman A, Mayeux R, Brown TR, Small SA. Imaging the Abeta-related neurotoxicity of Alzheimer disease. *Arch Neurol* 2007, 64: 1467-1477

- 156 Faure A, Verret L, Bozon B, El Tannir El Tayara N, Ly M, Kober F, Dhenain M, *et al.* Impaired neurogenesis, neuronal loss, and brain functional deficits in the APPxPS1-Ki mouse model of Alzheimer's disease. *Neurobiol Aging* 2009,
- 157 Massaad CA, Amin SK, Hu L, Mei Y, Klann E, Pautler RG. Mitochondrial superoxide contributes to blood flow and axonal transport deficits in the Tg2576 mouse model of Alzheimer's disease. *PLoS One* 2010, 5: e10561
- 158 Weidensteiner C, Metzger F, Bruns A, Bohrmann B, Kuennecke B, von Kienlin M. Cortical hypoperfusion in the B6.PS2APP mouse model for Alzheimer's disease: comprehensive phenotyping of vascular and tissular parameters by MRI. *Magn Reson Med* 2009, 62: 35-45
- 159 Bourasset F, Mélissa O, Tremblay C, Julien C, Do TM, Oddo S, LaFerla F, *et al.* Reduction of the cerebrovascular volume in a transgenic mouse model of Alzheimer's disease. *Neuropharmacology* 2009, 56: 808-813
- 160 Kantarci K, Weigand SD, Petersen RC, Boeve BF, Knopman DS, Gunter J, Reyes D, *et al.* Longitudinal 1H MRS changes in mild cognitive impairment and Alzheimer's disease. *Neurobiol Aging* 2007, 28: 1330-1339
- 161 Ackl N, Ising M, Schreiber YA, Atiya M, Sonntag A, Auer DP. Hippocampal metabolic abnormalities in mild cognitive impairment and Alzheimer's disease. *Neurosci Lett* 2005, 384: 23-28
- 162 Oberg J, Spenger C, Wang FH, Andersson A, Westman E, Skoglund P, Sunnemark D, *et al.* Age related changes in brain metabolites observed by 1H MRS in APP/PS1 mice. *Neurobiol Aging* 2008, 29: 1423-1433
- 163 Marjanska M, Curran GL, Wengenack TM, Henry PG, Bliss RL, Poduslo JF, Jack CR, Jr., *et al.* Monitoring disease progression in transgenic mouse models of Alzheimer's disease with proton magnetic resonance spectroscopy. *Proc Natl Acad Sci U S A* 2005, 102: 11906-11910
- 164 Dedeoglu A, Choi JK, Cormier K, Kowall NW, Jenkins BG. Magnetic resonance spectroscopic analysis of Alzheimer's disease mouse brain that express mutant human APP shows altered neurochemical profile. *Brain Res* 2004, 1012: 60-65
- 165 Franklin KB. The Mouse Brain in Stereotaxic Coordinates. In: Paxinos G ed.ed.: Academic Press, San Diego 1997
- 166 Yang D, Xie Z, Stephenson D, Morton D, Hicks CD, Brown TM, Sriram R, *et al.* Volumetric MRI and MRS provide sensitive measures of Alzheimer's disease neuropathology in inducible Tau transgenic mice (rTg4510). *Neuroimage* 2011, 54: 2652-2658
- 167 Jack CR, Dickson DW, Parisi JE, Xu YC, Cha RH, O'Brien PC, Edland SD, *et al.* Antemortem MRI findings correlate with hippocampal neuropathology in typical aging and dementia. *Neurology* 2002, 58: 750-757
- 168 DeKosky ST, Scheff SW. Synapse loss in frontal cortex biopsies in Alzheimer's disease: correlation with cognitive severity. *Ann Neurol* 1990, 27: 457-464
- 169 Salat DH, Kaye JA, Janowsky JS. Selective preservation and degeneration within the prefrontal cortex in aging and Alzheimer disease. *Arch Neurol* 2001, 58: 1403-1408
- 170 Thompson MD, Knee K, Golden CJ. Olfaction in persons with Alzheimer's disease. *Neuropsychol Rev* 1998, 8: 11-23

- 171 Killiany RJ, Hyman BT, Gomez-Isla T, Moss MB, Kikinis R, Jolesz F, Tanzi R, *et al.* MRI measures of entorhinal cortex vs hippocampus in preclinical AD. *Neurology* 2002, 58: 1188-1196
- 172 Sun SW, Liang HF, Cross AH, Song SK. Evolving Wallerian degeneration after transient retinal ischemia in mice characterized by diffusion tensor imaging. *Neuroimage* 2008, 40: 1-10
- 173 Song SK, Yoshino J, Le TQ, Lin SJ, Sun SW, Cross AH, Armstrong RC. Demyelination increases radial diffusivity in corpus callosum of mouse brain. *Neuroimage* 2005, 26: 132-140
- 174 Chen H, Epelbaum S, Delatour B. Fiber Tracts Anomalies in APPxPS1 Transgenic Mice Modeling Alzheimer's Disease. *J Aging Res* 2011, 2011: 281274
- 175 Teipel SJ, Bayer W, Alexander GE, Zebuhr Y, Teichberg D, Kulic L, Schapiro MB, *et al.* Progression of corpus callosum atrophy in Alzheimer disease. *Arch Neurol* 2002, 59: 243-248
- 176 Moon WJ, Kim HJ, Roh HG, Han SH. Atrophy measurement of the anterior commissure and substantia innominata with 3T high-resolution MR imaging: does the measurement differ for patients with frontotemporal lobar degeneration and Alzheimer disease and for healthy subjects? *AJNR Am J Neuroradiol* 2008, 29: 1308-1313
- 177 Kantarci K, Petersen RC, Boeve BF, Knopman DS, Weigand SD, O'Brien PC, Shiung MM, *et al.* DWI predicts future progression to Alzheimer disease in amnesic mild cognitive impairment. *Neurology* 2005, 64: 902-904
- 178 Dickerson BC, Wolk DA, Initiative AsDN. MRI cortical thickness biomarker predicts AD-like CSF and cognitive decline in normal adults. *Neurology* 2012, 78: 84-90
- 179 Jones DK, Cercignani M. Twenty-five pitfalls in the analysis of diffusion MRI data. *NMR Biomed* 2010, 23: 803-820
- 180 Pfefferbaum A, Rohlfing T, Rosenbloom MJ, Sullivan EV. Combining atlas-based parcellation of regional brain data acquired across scanners at 1.5 T and 3.0 T field strengths. *Neuroimage* 2012, 60: 940-951
- 181 Polders DL, Leemans A, Hendrikse J, Donahue MJ, Luijten PR, Hoogduin JM. Signal to noise ratio and uncertainty in diffusion tensor imaging at 1.5, 3.0, and 7.0 Tesla. *J Magn Reson Imaging* 2011, 33: 1456-1463
- 182 Whitwell JL, Sampson EL, Watt HC, Harvey RJ, Rossor MN, Fox NC. A volumetric magnetic resonance imaging study of the amygdala in frontotemporal lobar degeneration and Alzheimer's disease. *Dement Geriatr Cogn Disord* 2005, 20: 238-244
- 183 Rojas DC, Smith JA, Benkers TL, Camou SL, Reite ML, Rogers SJ. Hippocampus and amygdala volumes in parents of children with autistic disorder. *Am J Psychiatry* 2004, 161: 2038-2044
- 184 Alemán-Gómez Y, Melie-García L, Valdés-Hernandez P. IBASPM: Toolbox for automatic parcellation of brain structures. ed. Human Brain Mapping, 12th Annual Meeting; Florence, Italy. 2007
- 185 Ashburner J, Friston KJ. Voxel-based morphometry--the methods. *Neuroimage* 2000, 11: 805-821
- 186 Camara O, Scahill RI, Schnabel JA, Crum WR, Ridgway GR, Hill DL, Fox NC. Accuracy assessment of global and local atrophy measurement techniques with realistic simulated longitudinal data. *Med Image Comput Comput Assist Interv* 2007, 10: 785-792

- 187 Fischl B, Salat DH, Busa E, Albert M, Dieterich M, Haselgrove C, van der Kouwe A, *et al.* Whole brain segmentation: automated labeling of neuroanatomical structures in the human brain. *Neuron* 2002, 33: 341-355
- 188 Leow A, Yu CL, Lee SJ, Huang SC, Protas H, Nicolson R, Hayashi KM, *et al.* Brain structural mapping using a novel hybrid implicit/explicit framework based on the level-set method. *Neuroimage* 2005, 24: 910-927
- 189 Magnotta VA, Harris G, Andreasen NC, O'Leary DS, Yuh WT, Heckel D. Structural MR image processing using the BRAINS2 toolbox. *Comput Med Imaging Graph* 2002, 26: 251-264
- 190 Smith SM, Zhang Y, Jenkinson M, Chen J, Matthews PM, Federico A, De Stefano N. Accurate, robust, and automated longitudinal and cross-sectional brain change analysis. *Neuroimage* 2002, 17: 479-489
- 191 Studholme C, Cardenas V, Schuff N, Rosen H, Miller B, Weiner M. Detecting spatially consistent structural differences in Alzheimer's and frontotemporal dementia using deformation morphometry. ed. *MICCAI*:41–48. 2001
- 192 Desikan RS, Ségonne F, Fischl B, Quinn BT, Dickerson BC, Blacker D, Buckner RL, *et al.* An automated labeling system for subdividing the human cerebral cortex on MRI scans into gyral based regions of interest. *Neuroimage* 2006, 31: 968-980
- 193 Desikan RS, Cabral HJ, Hess CP, Dillon WP, Glastonbury CM, Weiner MW, Schmansky NJ, *et al.* Automated MRI measures identify individuals with mild cognitive impairment and Alzheimer's disease. *Brain* 2009, 132: 2048-2057
- 194 Reuter M, Schmansky NJ, Rosas HD, Fischl B. Within-subject template estimation for unbiased longitudinal image analysis. *Neuroimage* 2012, 61: 1402-1418
- 195 Wonderlick JS, Ziegler DA, Hosseini-Varnamkhasti P, Locascio JJ, Bakkour A, van der Kouwe A, Triantafyllou C, *et al.* Reliability of MRI-derived cortical and subcortical morphometric measures: effects of pulse sequence, voxel geometry, and parallel imaging. *Neuroimage* 2009, 44: 1324-1333
- 196 Kruggel F, Turner J, Muftuler LT, Initiative AsDN. Impact of scanner hardware and imaging protocol on image quality and compartment volume precision in the ADNI cohort. *Neuroimage* 2010, 49: 2123-2133
- 197 Morey RA, Selgrade ES, Wagner HR, Huettel SA, Wang L, McCarthy G. Scan-rescan reliability of subcortical brain volumes derived from automated segmentation. *Hum Brain Mapp* 2010, 31: 1751-1762
- 198 van der Kouwe AJ, Benner T, Salat DH, Fischl B. Brain morphometry with multiecho MPRAGE. *Neuroimage* 2008, 40: 559-569
- 199 Huang L, Wang X, Baliki MN, Wang L, Apkarian AV, Parrish TB. Reproducibility of Structural, Resting-State BOLD and DTI Data between Identical Scanners. *PLoS One* 2012, 7: e47684
- 200 Vollmar C, O'Muircheartaigh J, Barker GJ, Symms MR, Thompson P, Kumari V, Duncan JS, *et al.* Identical, but not the same: intra-site and inter-site reproducibility of fractional anisotropy measures on two 3.0T scanners. *Neuroimage* 2010, 51: 1384-1394
- 201 Bisdas S, Bohning DE, Besenski N, Nicholas JS, Rumboldt Z. Reproducibility, interrater agreement, and age-related changes of fractional anisotropy measures at 3T in healthy subjects: effect of the applied b-value. *AJNR Am J Neuroradiol* 2008, 29: 1128-1133

- 202 Jansen JF, Kooi ME, Kessels AG, Nicolay K, Backes WH. Reproducibility of quantitative cerebral T2 relaxometry, diffusion tensor imaging, and <sup>1</sup>H magnetic resonance spectroscopy at 3.0 Tesla. *Invest Radiol* 2007, 42: 327-337
- 203 Fox RJ, Sakaie K, Lee JC, Debbins JP, Liu Y, Arnold DL, Melhem ER, *et al.* A validation study of multicenter diffusion tensor imaging: reliability of fractional anisotropy and diffusivity values. *AJNR Am J Neuroradiol* 2012, 33: 695-700
- 204 Dale AM, Fischl B, Sereno MI. Cortical surface-based analysis. I. Segmentation and surface reconstruction. *Neuroimage* 1999, 9: 179-194
- 205 Fischl B, Sereno MI, Dale AM. Cortical surface-based analysis. II: Inflation, flattening, and a surface-based coordinate system. *Neuroimage* 1999, 9: 195-207
- 206 Fischl B, van der Kouwe A, Destrieux C, Halgren E, Ségonne F, Salat DH, Busa E, *et al.* Automatically parcellating the human cerebral cortex. *Cereb Cortex* 2004, 14: 11-22
- 207 Han X, Jovicich J, Salat D, van der Kouwe A, Quinn B, Czanner S, Busa E, *et al.* Reliability of MRI-derived measurements of human cerebral cortical thickness: the effects of field strength, scanner upgrade and manufacturer. *Neuroimage* 2006, 32: 180-194
- 208 Bland JM, Altman DG. Statistical methods for assessing agreement between two methods of clinical measurement. *Lancet* 1986, 1: 307-310
- 209 van Rijsbergen C. Information Retrieval. 2nd ed. London, U.K: Butterworths. ed. 1979
- 210 Cavedo E, Boccardi M, Ganzola R, Canu E, Beltramello A, Caltagirone C, Thompson PM, *et al.* Local amygdala structural differences with 3T MRI in patients with Alzheimer disease. *Neurology* 2011, 76: 727-733
- 211 Frisoni GB, Ganzola R, Canu E, Rüb U, Pizzini FB, Alessandrini F, Zoccatelli G, *et al.* Mapping local hippocampal changes in Alzheimer's disease and normal ageing with MRI at 3 Tesla. *Brain* 2008, 131: 3266-3276
- 212 Bonekamp D, Nagae LM, Degaonkar M, Matson M, Abdalla WM, Barker PB, Mori S, *et al.* Diffusion tensor imaging in children and adolescents: reproducibility, hemispheric, and age-related differences. *Neuroimage* 2007, 34: 733-742
- 213 Ciccarelli O, Parker GJ, Toosy AT, Wheeler-Kingshott CA, Barker GJ, Boulby PA, Miller DH, *et al.* From diffusion tractography to quantitative white matter tract measures: a reproducibility study. *Neuroimage* 2003, 18: 348-359
- 214 Pfefferbaum A, Adalsteinsson E, Sullivan EV. Replicability of diffusion tensor imaging measurements of fractional anisotropy and trace in brain. *J Magn Reson Imaging* 2003, 18: 427-433
- 215 Heiervang E, Behrens TE, Mackay CE, Robson MD, Johansen-Berg H. Between session reproducibility and between subject variability of diffusion MR and tractography measures. *Neuroimage* 2006, 33: 867-877
- 216 Drago V, Babiloni C, Bartrés-Faz D, Caroli A, Bosch B, Hensch T, Didic M, *et al.* Disease tracking markers for Alzheimer's disease at the prodromal (MCI) stage. *J Alzheimers Dis* 2011, 26 Suppl 3: 159-199
- 217 Cho H, Yang DW, Shon YM, Kim BS, Kim YI, Choi YB, Lee KS, *et al.* Abnormal integrity of corticocortical tracts in mild cognitive impairment: a diffusion tensor imaging study. *J Korean Med Sci* 2008, 23: 477-483
- 218 Mielke MM, Kozauer NA, Chan KC, George M, Toroney J, Zerrate M, Bandeen-Roche K, *et al.* Regionally-specific diffusion tensor imaging in mild cognitive impairment and Alzheimer's disease. *Neuroimage* 2009, 46: 47-55

219 Marengo S, Rawlings R, Rohde GK, Barnett AS, Honea RA, Pierpaoli C, Weinberger DR. Regional distribution of measurement error in diffusion tensor imaging. *Psychiatry Res* 2006, 147: 69-78



## 8 SCIENTIFIC PRODUCTS

### Papers

**Moira Marizzoni**, Gianluigi Forloni, Giovanni B. Frisoni. New paradigm for testing AD drugs – Surrogate outcomes homologous in animals and humans. Submitted to "Drug Discovery Today: Therapeutic Strategies" on April 26th.

Jorge Jovicich\*, **Moira Marizzoni**\*, Roser Sala-Llloch, Núria Bargalló, David Bartrés-Faz, Jennifer Arnold, Jens Benninghoff, Jens Wiltfang, Luca Roccatagliata, Flavio M. Nobili, Christian Zeeh, Thomas Günther, Peter Schönknecht, Melanie Leroy, Regis Bordet, Valérie Chanoine, Jean-Philippe Ranjeva, Mira Didic, Oliver Blin, Hélène Gros-Dagnac, Pierre Payoux, Giada Zoccatelli, Franco Alessandrini, Alberto Beltramello, Giovanni B. Frisoni, on behalf of PharmaCog Consortium. Brain morphometry reproducibility in multi-center 3T MRI studies: An evaluation of cross-sectional and longitudinal segmentations. Manuscript under internal review for submission to Neuroimage.

**Moira Marizzoni**, Edoardo Micotti, Marco Lorenzi, Alessandra Paladini, Anna Caroli, Claudia Balducci, Sophie Dix, Michael O'Neill, Christian Czech, Laurence Ozmen, Jill C. Richardson, Gianluigi Forloni, Giovanni Frisoni. *In vivo* diffusion tensor imaging and tract-based spatial statistics in three mouse models of Alzheimer's disease. *In preparation*.

**Moira Marizzoni**\*, Jorge Jovicich\*, Roser Sala-Llloch, Nuria Bargalló, David Bartrés-Faz, Jennifer Arnold, Jens Benninghoff, Jens Wiltfang, Luca Roccatagliata, Flavio Nobili, Christian Zeeh, Peter Schonknecht, Giada Zoccatelli, Franco Alessandrini, Alberto Beltramello, Hélène GROS-DAGNAC, Pierre Payoux, Valérie, Chanoine, Jean-Philippe Ranjeva, Mira Didic, Melanie Leroy, Regis Bordet, Giovanni Frisoni. Across-session reproducibility of DTI derived metrics measured at 3T: Pharmacog consortium. *In preparation*.

\* Co-first authors

### Congress presentations (published only)

#### AD/PD 2013 (Florence, March 5-10)

**Moira Marizzoni**. In vivo Diffusion Tensor Imaging in Three Mouse Models of Alzheimer's Disease. Oral presentation.

#### AAIC 2012 (Vancouver, July 15-19)

**Moira Marizzoni**, Edoardo Micotti, Marco Lorenzi, Alessandra Paladini, Anna Caroli, Claudia Balducci, Sophie Dix, Michael O'Neill, Christian Czech, Laurence Ozmen, Jill C. Richardson, Gianluigi Forloni, Giovanni Frisoni. *In vivo* diffusion tensor imaging and tract-based spatial statistics in three mouse models of Alzheimer's disease. *Alzheimer's & Dementia: The Journal of the Alzheimer's Association*, Vol. 8, Issue 4, Supplement, Pages P154-P155, July 2012. Presented as a poster.

Edoardo Micotti, Alessandra Paladini, **Maira Marizzoni**, Anna Caroli, Claudia Balducci, Sophie Dix, Michael O'Neill, Christian Czech, Laurence Ozmen, Jill C. Richardson, Giovanni Frisoni, Gianluigi Forloni. Cerebral structural changes in different transgenic models of Alzheimer's disease: An MRI study Alzheimer's & Dementia: The Journal of the Alzheimer's Association, Vol. 8, Issue 4, Supplement, Page P152, July 2012. Presented as a poster.

Jorge Jovicich, Genoveffa Borsci, **Maira Marizzoni**, Roser Sala-Llonch, Núria Bargalló, David Bartréz-Faz, Jens Benninghoff, Jens Wiltfang, Luca Roccatagliata, Flavio M. Nobili, Karl-Titus Hoffmann, Thomas Günther, Peter Schönknecht, Aurélien Monnet, Regis Bordet, Valérie Chanoine, Alexandra Auffret, Jean-Philippe Ranjeva, Oliver Blin, Hélène Gros-Dagnac, Pierre Payoux, Giada Zoccatelli, Franco Alessandrini, Alberto Beltramello, Hans-Goran Hardemark, Giovanni B. Frisoni. Pharmacog: Multi-site MRI calibration to study progression of Alzheimer's disease. Alzheimer's & Dementia: The Journal of the Alzheimer's Association, Vol. 8, Issue 4, Supplement, Page P342, July 2012. Presented as a poster.